UNIVERSITY OF CALIFORNIA
RIVERSIDE

Large-Area Quality Control of Atomically-Thin Layered Materials

A Dissertation submitted in partial satisfaction
of the requirements for the degree of

Doctor of Philosophy

in

Electrical Engineering

by

Craig Merten Nolen

March 2012

Dissertation Committee:
Dr. Alexander A. Balandin, Chairperson
Dr. Roger Lake
Dr. Alexander Khitun

The Dissertation of Craig Merten Nolen is approved by:

_____

_____

_____

University of California, Riverside

ACKNOWLEDGEMENT

First and foremost, I would like to thank my research adviser Professor Alexander A. Balandin for giving me the unique opportunity to pursue my own research interests. I am endowed to him for providing me a world class education through his guidance using the self-guided approach. He provided me the perfect balance between allowing me to define my own dissertation work and thrusting my motivations in the right direction when it was of critical importance. It was through this advising that I gained the key understanding of what it took to become a successful research scientist.

I would like to thank all my colleagues at the Nano-Device Laboratory for their helpful comments and always providing a positive atmosphere at the workplace. My sincere gratitude of thanks goes out to Desalegne, Javed, Vivek, Jie, Guanxiong, Pradyumna, Zhong, Richard, Samia, Irene, Ben, and Zahid. I would like to thank Bir Bhanu and Giovanni Denina of the Visualization and Intelligent Systems Laboratory for their collaboration with all work in my dissertation involving MATLAB image processing toolbox throughout chapter 3 where much of this section was reprinted from Nolen et al., ACS Nano 5, 914 (2012) with permission. Also much thanks to Anirutha Sumant for wafers with CVD graphene grown on Ni wafers in chapter 3.5. Much appreciation to Sandia National Labs for allowing me use part of the work I completed as chapter 4. The following details specifically address individual acknowledgements as requested by Sandia National Laboratories for chapter 4. I would like to thank my colleagues at Sandia National Laboratories in Albuquerque, NM for spending their time and patience in helping me build and execute my graphene transfer objectives during my

6 month graduate student internship. These results are reflected in Chapter 4 of this dissertation. Section 4.1 and 4.2 of Chapter 4 in this dissertation was a direct and partial rendition correspondingly of the work that I completed in section 4.2 of the SAND2011-6961 Enabling Graphene Nanoelectronics – Sandia 2011 Report. The experience that I gained at Sandia was truly invaluable one and without a doubt has helped shape me to become a more profound researcher with a wider skill set along with better analytical skills making me much more competitive in the job market than I would have been without this experience. Included are the details of the assistance that each Sandian individual contributed to my work. I am deeply indebted to Dr. Stephen Howell for his advising through guidance and mentorship that he provided me on the electrostatic graphene transfer project where he supplied me with the original apparatus setup, custom developed LabVIEW software for electrical measurements, and directing me on the theoretical aspects of my work as well. I am especially appreciative that Steve took out the time to seriously listen to each of my unique research ideas for possible future research project ventures and provided realistic feedback while trying to see them through no matter how off-the-wall they might have been. I want to thank Anthony Ross III (TJ) for designing / fabricating graphite pillared structures, SiC pillared structures, and preparation for the Si_3N_4 target substrates with Ti/Au backside contact. I especially want to give TJ thanks for teaching me these methods with hands on experience by bringing me in Sandia's MESA Fab clean room. I want to thank Taisuke Ohta for providing epitaxial grown graphene samples on SiC Si-face (0001) of both single layer and hydrogen intercalated Bernal stacked bi-layer graphene for future studies. I want to thank

Thomas Beechem and Anthony E. McDonald for providing Raman spectroscopic mapping scans of the graphene samples on the various insulating substrates. I want to thank Laura Biedermann who initially trained me on the electrostatic transfer process, brought me up to speed with prior electrostatic graphene transfer work, got me acquainted with the Sandian work place, and developed the graphene constructive optical interference naked eye visualization model for viewing graphene layers on top of Si_3N_4 under an optical microscope. I would like to thank Thomas Friedmann for the fabrication of Si_3N_4 using the LPCVD tool. I would like to thank Scott Habermehl for extremely useful discussions of electrical testing on theory and experiment utilizing his breadth of knowledge on Si_3N_4 from his years of experience and publications on the subject matter including the poole-frenkle emission effects through calculation and experiment. Lastly, I would like to thank David Henry for useful discussions on insight involving SEM work and guiding me in the right direction on a number of different aspects on Sandian related projects. Contact for Sandian based work can be sent to Dr. Stephen W. Howell at swhowell@sandia.gov who is the principal investigator (PI) on the Graphene Nanoelectronics initiative in the Rad-Hard CMOS Technology Department.

I want to end with acknowledging my family Andrea, RJ, Ben, Lynn and Larry for providing their love, support, and understanding through all my educational endeavors. As for my parents, thank you for the complete financial support that you have given me throughout my entire education. I am forever thankful for this aid and as requested, I promise to pass this gift on to my children allowing them to focus on their studies without financial pressures.

To my family

Andrea, RJ, Ben, Lynn, and Larry

ABSTRACT OF THE DISSERTATION

Large-Area Quality Control of Atomically-Thin Layered Materials

by

Craig Merten Nolen

Doctor of Philosophy, Graduate Program in Electrical Engineering
University of California, Riverside, March 2012
Dr. Alexander A. Balandin, Chairperson

Fast progress in chemical vapor deposition of graphene and other quasi-two-dimensional layered materials such as topological insulators call for development of a reliable high-throughput method of layered materials identification and quality control. The number of atomic planes in graphene or other ultra-thin films has to be determined very fast and over large wafer-scale areas. The previously existed methods of accurate counting of the number of atomic planes in few-layer graphene were primarily based on micro-Raman spectroscopy. These methods were local, slow, and could not be scaled up to characterize the whole wafers. In this dissertation research I proposed and developed an automatic approach for graphene inspection over the wafer-size areas. The proposed method can be scaled up for industrial use. It is based on the image processing analysis of the pseudo-color contrasts uniquely assigned to each few-layer graphene region characterized by a specific number of atomic planes. The initial calibration of the technique is performed

with the help of micro-Raman spectroscopy. The image processing is also used to account for the lighting non-uniformity of the samples. Implementation of the technique developed in this dissertation research reduces the cost and time required for graphene identification and quality assessment, and can become the next major impetus for practical applications of graphene, few-layer graphene and other atomically-thin films. The technique was tested on mechanically exfoliated graphene and then extended to the chemical-vapor-deposited graphene, and to bismuth telluride topological insulator thin films. The second part of the dissertation research deals with development of the electrostatic transfer process. The investigated approach allows one to transfer the patterned few-layer graphene films controllably to Si_3N_4 substrates compatible with other materials. The large-area quality control and graphene transfer techniques developed in this dissertation research are important for the proposed practical applications of graphene in electronics and optoelectronics.

Contents

List of Figures

Chapter 1

Introduction

Recent studies in materials research have drawn increased interest towards low dimensional materials for integration into or replacement of current silicon complementary metal-oxide semiconductor (Si-CMOS) integrated circuit (IC) technology. Reports of extraordinary intrinsic properties of atomically-thin materials have revamped focus onto this topic of research as a possible gateway to fuel the next generation of semiconductor technologies. Novel nanomaterials have since emerged from these guided research efforts unleashing a plethora of previously unforeseen possibilities. Many of these nanoscale technologies reveal enhanced properties that enable new semiconductor device physics in the 'quantum physics regime' and some even in the 'relativistic regime' to be utilized. This in turn spawned a countless number of potential real world device applications that very well may change the course of semiconductor electronics history.

1.1 HISTORICAL PERSPECTIVE: END OF MOORE'S LAW AND NEW SEMICONDUCTOR TECHNOLOGIES

Since the invention of the integrated circuit made from the silicon transistor in 1958, there has been a steady trend of a two-fold increase in transistors every 18 months and a drastic size reduction coined by Moore's Law [1]. This was predicted by Gordon E. Moore which consequently became a relatively accurate prediction. This trend has

continued without much deviation until recently when the limitations of silicon-based devices have begun to reach their limitations on speed, size, thermodynamic stability, and electrical current leakage among other things [2]. With this setback, the need for new innovative semiconductor technologies became of the utmost importance for continuing the progression of Moore's Law into the future. Since silicon is the basis for the semiconductor industry, it is critical that new materials be compatible for integration with current Si-CMOS technology [3, 4]. Just as well, unconventional innovations that replace silicon-based technology need to compete equally or better on various levels than their Si-based predecessors. The success of these new technologies will rely heavily on their ability to provide real-world applicability in terms of parallel fabrication for industrial manufacturing in a timely manner with relatively low production costs [3]. Carbon-based electronics has become a paramount focus of advancing technology beyond their previous limits through numerous approaches [4].

1.2 MOTIVATIONS: FROM GRAPHENE'S PROPERTIES TO PRODUCTION LIMITATIONS

In 2004, a new carbon-based material named graphene, a single atomic layer of sp^2 bonded carbon atoms arranged in a hexagonal crystal lattice, was discovered experimentally through mechanical exfoliation for the first time [5, 6]. More than a decade before, graphene previously gained much attention in the theoretical physics community for its extraordinary intrinsic properties following a new physical regime 'relativistic physics' instead of traditional 'quantum or classical physics' [7]. Until

recently, strictly quasi-two-dimensional (2D) crystals were said to not exist at room temperature due to thermodynamic instability debated by Landau and Peierls ~70+ years ago [8, 9]. On the contrary, graphene has proven to be stable and exist at room temperature due to the occupation of hanging bonds causing graphene to either wrinkle when suspended or bind-coupled to a substrate [10]. In turn, this single 2-Dimensional (2D) atomic sheet of graphene atoms consequently makes up the basic building block for 0-Dimensional (0D) buckyballs, 1-Dimensional (1D) carbon nanotubes, and 3-Dimensional (3D) bulk graphite [7]. For the past 6 years, graphene research has incurred a massive influx in published work shown by a 2010 report by Dresselhaus et. al. [11] including studies on experimental, theoretical, and practical application findings for this material. Prior to the discovery of graphene, carbon nanotubes were the major focus of carbon-based research which yielded few applications due to the major limiting factor of the inability to develop parallel fabrication processes that were cheap, simple, and compatible with integration into current silicon manufacturing processes [12]. Unlike with the case of carbon nanotubes, graphene's quasi-two-dimensional layered interface (in the x-y plane) allow this material to be fabricated for a large-area using standard parallel fabrication processes such as chemical vapor deposition (CVD) leading to greater possibly for real-world applications [13].

What sets graphene apart from other materials are its exotic intrinsic electronic [14], thermal [15] shown in Table 1.1, optical [16-18], and mechanical properties [19]. These intrinsic properties remain strongly dependent on the number of atomic planes. Furthermore, the physical characteristics of few-layer graphene (FLG) are different from

those of single layer graphene (SLG). SLG reveals electron mobility in the range from ~40,000 to 400,000 $cm^2V^{-1}s^{-1}$ [14] and intrinsic thermal conductivity above ~3000 W/mK for large suspended flakes [15, 19-22] while bi-layer graphene (BLG) exhibits electron mobility in the range from ~3000 to 8000 $cm^2V^{-1}s^{-1}$ [5] and intrinsic thermal conductivity near ~2500 W/mK [23, 24]. The electronic, thermal and optical properties of FLG approach those of bulk graphite as the number of atomic layers exceeds approximately ten layers [25, 26]. The optical transparency of FLG also shows a strong function of the number of layers [16-18]. The one-atom thickness of graphene and its optical

Important Materials	**Room Temp Thermal Conductivity**
Silicon (Si)	145 W/mK
SiO_2	1 - 13 W/mK
Copper	400 W/mK
Carbon Materials	
Diamond	1000 - 2200 W/mK
Graphite	200 - 2000 W/mK (Orientation Dependent)
Diamond-like Carbon (DLC)	0.1 - 10 W/mK
Carbon Nano-tubes (CNTs)	3000 - 3500 W/mK
Single Layer Graphene	**~2000~5300 W/mK [15] (Size Dependent)**
Bi-Layer / Few Layer Graphene	**~2800 W/mK [23] / ~1300W/mK [23]**

Table 1.1: Room temperature thermal conductivity values of common materials used in semiconductors and thermal conductivity values of carbon materials.

transparency (only ~2.3% absorption per layer [16]) make graphene identification and counting the number of atomic planes in FLG extremely challenging.

Recent progress in the chemical vapor deposition (CVD) growth of graphene led to fabrication of large-area graphene layers that are transferable onto various insulating substrates [27, 28]. CVD grown graphene layers of up to 30 inches in size on cheap flexible substrates have been demonstrated [27]. Various methods of graphene synthesis were reported [29-31]. It is reasonable to expect, in near future, the emergence of graphene growth techniques on insulating substrates, which would allow one to avoid the graphene transfer steps. A number of recent demonstrations show the possibility of growing graphene directly onto Cu metal growth substrate where Cu was evaporated away at high temperatures leaving behind the grown graphene layers on top of the dielectric medium without using any transfer steps [32]. Growth directly on near-lattice matched insulating substrates has been demonstrated by growing graphene directly on hexagonal boron nitride (h-BN) using CVD [33], on silicon carbide (SiC) using molecular-beam epitaxial growth (MBE) [34] or on SiC via CVD growth [35]. The fusion of the large-area graphene on cheap, transparent, flexible substrates with graphene-based OLED technology is expected to lead to major practical applications [36]. However, as larger area graphene becomes available, quality control remains as an important factor limiting further progress in graphene research and applications. For all these reasons, it is important to develop a fast scalable method for determining the number of atomic planes in synthesized graphene or mechanically exfoliated graphene from highly ordered pyrolytic graphite (HOPG) bulk ingot. The crucial feature of this method, which would

allow for industry applications, should be its suitability for large-area substrates (i.e. lateral dimensions in millimeters or inches). The electronic industry requires high quality large-area wafers that can be used for reliable high-throughput device fabrication.

Many methods currently exist for identifying layers of graphene, which are used individually or in combination for counting the number of atomic layers in graphene samples and for extrapolating the quality of graphene (e.g. presence of lattice defects or impurities [37, 38]). Some of these methods include micro-Raman spectroscopy [39, 40], optical microscopy [16-18], low-energy electron microscopy (LEEM) [41, 42], low-energy electron diffraction (LEED) [29, 41], atomic force microscopy (AFM) [7], scanning electron microscopy (SEM) [7], transmission electron microscopy (TEM) [7], scanning tunneling microscopy (STM) [43], photoelectron microscopy (PES) [41], angle resolved photoelectron spectroscopy (ARPES) [41], photoemission electron microscope (PEEM) [41], Image J data analysis software [44], and reflection high-energy electron diffraction (RHEED) [45] are the most commonly used methods for graphene characterization to observe material bonds, defect impurities, or layer stack counting. Yet, these processes are severely limited by their slow, expensive, and non-automated measurement procedures. Also, most of these techniques provide only a rough estimate at best for determining the number of atomic planes. Of these identification tools, micro-Raman spectroscopy remains as the only non-destructive reliable and accurate technique with optical microscopy for graphene layer quantification and is the most widely used technique.

REFERENCES

1. G. E. Moore, *Proceedings of the IEEE* **86**, 82 (1998).
2. C.G Hwang, *IEDM IEEE-EDS International* 1 (2007).
3. R.R. Schaller, *IEEE Spectrum* **34**, 52 (1997).
4. P. Avouris, Z. Chen, and V. Perebeinos, *Nature Nanotechnology* **2**, 605 (2007).
5. K. S. Novoselov, A. K. Geim, S. V. Morozov, D. Jiang, Y. Zhang, S. V. Dubonos, I. V. Grigorieva, and A. A. Firsov, *Science* **306**, 666 (2004).
6. K. S. Novoselov, D. Jiang, F. Schedin, T. J. Booth, V. V. Khotkevich, S. V. Morozov, and A. K. Geim, *Proc. Natl. Acad. Sci.* **102**, 10451 (2005).
7. A. K. Geim and K. S. Novoselov, *Nature Materials* **6**, 183 (2007)
8. R. E. Peierls, *Ann. I. H. Poincare* **5**, 177 (1935).
9. L. D. Landau, *Phys. Z. Sowjetunion* **11**, 26 (1937).
10. J. C. Meyer, A. K. Geim, M. I. Katsnelson, K. S. Novoselov, T. J. Booth, and S. Roth, *Nature* **446**, 60 (2007).
11. M. S. Dresselhaus and P. T. Araujo, *ACS Nano* **4**, 6297 (2010).
12. M. Paradise and T. Goswami, *Mat. Des.* **28**, 1477 (2007).
13. A. K. Geim, *Science* **324**, 1530 (2009).
14. S. Morozov, K. S. Novoselov, M. I. Katsnelson, F. Schedin, D. C. Elias, J. A. Jaszczak, and A. K. Geim, *Phys. Rev Lett.* **100**, 016602 (2008).
15. A. A. Balandin, S. Ghosh, W. Bao, I. Calizo, D. Teweldebrhan, F. Miao, and C. N. Lau, *Nano Lett.* **8**, 902 (2008).

16. P. Blake, E. W. Hill, A. H. Castro Neto, K. S. Novoselov, D. Jiang, R. Yang, T. J. Booth, and A. K. Geim, *Appl. Phys. Lett.* **91**, 063124 (2007).
17. R. R. Nair, P. Blake, A. N. Grigorenko, K. S. Novoselov, T. J. Booth, T. Stauber, N. M . R. Peres, and A. K. Geim, *Science* **320**, 1308 (2008).
18. C. Casiraghi, A. Hartschuh, E. Lidorikis, H. Qian, H. Harutyunyan, T. Gokus, K. S. Novoselov, and A. C. Ferrari, *Nano Lett.* **7**, 2711 (2007).
19. S. Ghosh, I. Calizo, D. Teweldebrhan, E. P. Pokatilov, D. L. Nika, A. A. Balandin, W. Bao, F. Miao, and C. N. Lau, *App. Phys. Lett.* **92**, 151911 (2008).
20. D. L. Nika, E. P. Pokatilov, A. S. Askerov, and A. A. Balandin, *Phys. Rev. B* **79**, 155413 (2009).
21. D. L. Nika, S. Ghosh, E. P. Pokatilov, and A. A. Balandin, *App. Phys. Lett.* **94**, 203103 (2009).
22. S. Ghosh, D. L. Nika, E. P. Pokatilov, and A. A. Balandin, *New J. of Phys.* **11**, 095012 (2009).
23. S. Ghosh, W. Bao, D. L. Nika, S. Subrina, E. P. Pokatilov, C. N. Lau, and A. A. Balandin, *Nat. Mater.* **9**, 555 (2010).
24. A. A. Balandin, S. Ghosh, D. L. Nika, and E. P. Pokatilov, *Fullerenes, Nanotubes and Carbon Nanostructures* **18**, 474 (2010).
25. B. Partoens and F. M. Peeters, *Phys. Rev. B* **74**, 075404 (2006).
26. I. Calizo, F. Miao, W. Bao, C. N. Lau, and A. A. Balandin, *Appl. Phys. Lett.* **91**, 071913 (2007).

27. S. Bae, H. Kim, Y. Lee, X. Xu, J. S. Park, Y. Zheng, J. Balakrishnan, T. Lei, H. R. Kim, Y. Song, Y. J. Kim, K. S. Kim, B. Ozyilmaz, J. H. Ahn, B. H. Hong, and S. Iijima, *Nature Nanotechnology* **5**, 574 (2010).
28. X. Li, W. Cai, J. An, S. Kim, J. Nah, D. Yang, R. Piner, A. Velamakanni, I. Jung, E. Tutuc, S. K. Banerjee, L. Colombo, and R. S. Ruoff, *Nature* **324**, 1312 (2009).
29. C. Berger, Z. Song, T. Li, X. Li, A. Y. Ogbazghi, R. Feng, Z. Dai, A. N. Marchenkov, E. H. Conrad, P. N. First, and W. A. de Heer, *J. Phys. Chem. B* **108**, 19912 (2004).
30. L. Zhang, J. Liang, Y. Huang, Y. Ma, Y. Wang, and Y. Chen, *Carbon* **47**, 3665 (2009).
31. L. C. Campos, V. R. Manfrinato, J. D. Sanchez-Yamagishi, J. Kong, and P. Jarillo-Herrero, *Nano Lett.* **9**, 2600 (2009).
32. A. Ismach, C. Druzgalski, S. Penwell, A. Schwartzberg, M. Zheng, A. Javey, J. Bokor, and Y. Zhang, *Nano Lett.* **10**, 1542 (2010).
33. X. Ding, G. Ding, X. Xie, F. Huang, and M. Jiang, *Carbon* **49**, 2522 (2011).
34. K. Lee, S. Kim, M. S. Points, T. E. Beechem, T. Ohta, and E. Tutuc, *Nano Lett.* **11,** 3624 (2011).
35. W. Strupinski, K. Grodecki, A. Wysmolek, R. Stepniewski, T. Szkopek, P. E. Gaskell, A. Gruneis, D. Haberer, R. Bozek, J. Krupka, and J. M. Baranowski, *Nano Lett.* **11**, 1786 (2011).
36. J. Wu, M. Agrawal, H. A. Becerril, Z. Bao, Z. Liu, Y. Chen, and P. Peumans, *ACS Nano* **4**, 43 (2010).

37. D. Teweldebrhan and A. A. Balandin, *Appl. Phys. Lett.* **94**, 013101 (2009).

38. D. Teweldebrhan and A. A. Balandin, *App. Phys. Lett.* **95**, 246102 (2009).

39. A. C. Ferrari, J. C. Meyer, V. Scardaci, C. Casiraghi, M. Lazzeri, F. Mauri, S. Piscanec, D. Jiang, K. S. Novoselvo, S. Roth, and A. K. Geim, *Phys. Rev. Lett.* **97**, 187401 (2006).

40. A. Gupta, G. Chen, P. Joshi, S. Tadigadapa, and P. C. Eklund, *Nano Lett.* **6**, 12, 2667 (2006).

41. C. Virojanadara, M. Syvajarvi, R. Yakimova, L. I. Johansson, A. A. Zakharov, and T. Balasubramanian, *Phys. Rev. B* **78**, 245403 (2008).

42. H. Hibino, H. Kageshima, F. Maeda, M. Nagase, Y. Kobayashi, and H. Yamaguchi, *Phys. Rev. B* **77**, 075413 (2008).

43. E. Stolyarova, K. T. Rim, S. Ryu, J. Maultzsch, P. Kim, L. E. Brus, T. F. Heinz, M. S. Hybertsen, and G. W. Flynn, *PNAS* **104**, 9209 (2007).

44. P. E. Gaskell, H. S. Skulason, C. Rodenchuk, and T. Szkopek, *Appl. Phys. Lett.* **94**, 143101 (2009).

45. T. Jun, L. Zhong-Liang, K. Chao-Yang, P. Hai-Bin, W. Shi-Qiang, X. Peng-Shou, G. Yu-Qiang, and X. Xian-Gang, *Chinese Phys. Lett.* **26**, 088104 (2009).

Chapter 2

Background: Properties of Graphene and Nanomaterials

Graphene and other atomically-thin quasi two-dimensional (2D) Dirac materials such as bismuth telluride family of materials have been studied for their exceptional intrinsic properties especially at room temperature. These properties have attracted great interest for their potential to advance semiconductors in device applications such as thermal management, mobility enhancement, and many others. Recent studies have proven that enhancement of nanomaterials consisting of layered quasi-2D stacks is possible by extracting low dimensional forms of these thin films by breaking their Van der Waals 'gaps' (binding force) within their vertical out-of-plane cross-section and isolating individual layers. This can lead to either high mobility, greater thermal conductivity, or a higher ZT value depending on the isolated properties that are particular to the specific quasi-2D Dirac material.

2.1 NANOMATERIALS OVERVIEW

Nanotechnology has been growing rapidly with areas broadening in complexity, where focus has been on nanostructured materials with varied chemical composition. Fabrication of nanoparticles, nanowires, thin-films, quasi-two-dimensional sheets, nanotubes, and other nano-sized colloids have been produced which continue to be studied. The foundation of nanomaterials lies within the genre of being larger than single

atoms and molecules but smaller than their bulk composites. The properties of these materials cannot be classified through the laws of classical physics nor do they abide by absolute quantum chemistry. Two major factors account for the reasoning behind this uniquely defined physical regime different from others. The first factor lies within the dispersion of nanometer-scaled crystalline systems [1]. As crystal size decreases, the quantity of atoms at the surface of the crystal compared to the quantity of atoms within the crystal itself, increases. The second factor is size quantization which comes into effect when the size of the nanomaterial is around the same order as the de Broglie wavelength of its charge carriers [2]. Essentially when these materials become on the order of below 20nm they experience a transition from semiconducting behavior to molecular behavior. This is due to the spatial confinement of charge carriers, whereby the valence and conduction band edges split into discrete electronic levels that are quantized. Similarly, these electronic levels are close to that of atoms and molecules. From here, their properties (electrical, optical, chemical, mechanical, magnetic, etc.) can be manipulated by engineering the size, composition, and morphology of these nanomaterials which create enhanced features different from their derivative parent materials (bulk).

2.2 ATOMIC STRUCTURE AND ELECTRONIC PROPERTIES OF GRAPHENE

Graphene consists of two-dimensional sheets containing a hexagonal crystal structure of carbon atoms as a triangular lattice with a basis of two atoms per unit cell. The crystal lattice of graphene can be represented in real-space and in reciprocal space. In the real-

space vectors a_1 and a_2 are primitive vectors where a~1.42Å represents the carbon-carbon distance. The length between lattice spacing is 2.46 Å creating a strong bonding in-plane. However, the much larger interlayer spacing of 3.35 Å makes interlayer binding in graphene weak. In addition, the nearest neighborhood distances between atoms are $\delta_1, \delta_2, \delta_3$. In the k-space / momentum space, the reciprocal lattice vectors are b_1 and b_2 where dashed lines complete the rhombus forming the unit cell in reciprocal space. High symmetry points Γ, *K*, and *M* with Dirac cones are located at K and K$^{'}$ points [3] between the conduction and valance band at each of the six k points in the Brillion zone respective to the k-space (momentum space). The two-dimensional (2D) monatomic arrangement of sp^2 bonded carbon atoms in a hexagonal crystal lattice creates a unique real-space by using one s and two p orbitals (one being a p_x orbital and one being a p_y orbital) resulting in the special k-space that we see. Between each graphene layer in the real-space, a p_z orbital exists where stacking between graphene layers is shifted and weakly binded together with dispersion forces consisting of a-b, π-π* bond stacking order as "Van der Waals gaps" [3]. The Dirac point in the electronic band structure of graphene produces a linear dispersion at low energies described by a 2D mass less electron gas modeled after E~k from the Dirac equation where derivation of effective mass for this case becomes zero at rest. This is proven by showing that these relativistic particles change cyclotron mass with charge carrier density increase, following the Dirac Equation, as to the usual parabolic Schrodinger dispersion $E \sim k^2$ having a constant cyclotron mass independent of charge carrier density. This means at the k-points for low energies mass less Dirac quasi-particles in graphene can effectively move at or near the speed of light $v_F = 10^6 m^{-1}$ [3].

The k-space of graphene can be calculated using the tight-binding model approximation representing energy dispersion [4].

2.3 RAMAN SPECTROSCOPIC CHARACTERIZATION

Raman spectroscopy is used as a powerful tool that is effective and non-destructive (at low power) for characterizing semiconductors in a variety of forms such as device, bulk, thin-film, or nanostructures. This technique is quick, does not require sample preparation, and can measure very small samples. More specifically, the Raman spectrum allows for differentiation of one material different from another by measuring the molecular vibrations sensitive to specific bonds within each material. Moreover, C. V. Raman was credited with the Nobel Prize in physics in 1930 for discovering the Raman scattering effect which resulted from his findings that a photon from incident light was annihilated while simultaneously creating a scattered photon interaction within a medium [5].

Conceptually, the Raman scattering process entails incident photons ω_i interacting with a medium where scattering processes occur whereby photons are emitted back out. When these incident protons interact with a solid-state crystalline material, the atoms vibrate about their equilibrium positions over the entire structure. This effectively scatters these photons from lattice vibrations which quantize and transfer throughout the material as phonons abiding by Bose-Einstein statistics. More specifically, the lattice releases or absorbs energy $\eta\omega$ where η is Planck's constant and ω is the characteristic phonon frequency corresponding directly to the increase or decrease in scattered photon frequency ω_S where $\omega_S = \omega_i \pm \omega$. An Anti-Stokes process occurs when a phonon is

absorbed and the emitted photon frequency is increased. The opposite case happens for a Stokes process when a phonon is annihilated and the emitted photon frequency is decreased detailed in Figure 2.1. Further details can describe these processes where Figure 2.2 illustrates a visual representation of these Raman scattering processes (left) with a corresponding phonon dispersion graph to show typical propagation through a crystal lattice in the first Brillion zone (right). In Raman spectroscopy measurements, the wavelengths of measured photon emission generally follow unit notation of cm^{-1} and display intensity of photon emission characteristically by their density of states (DOS).

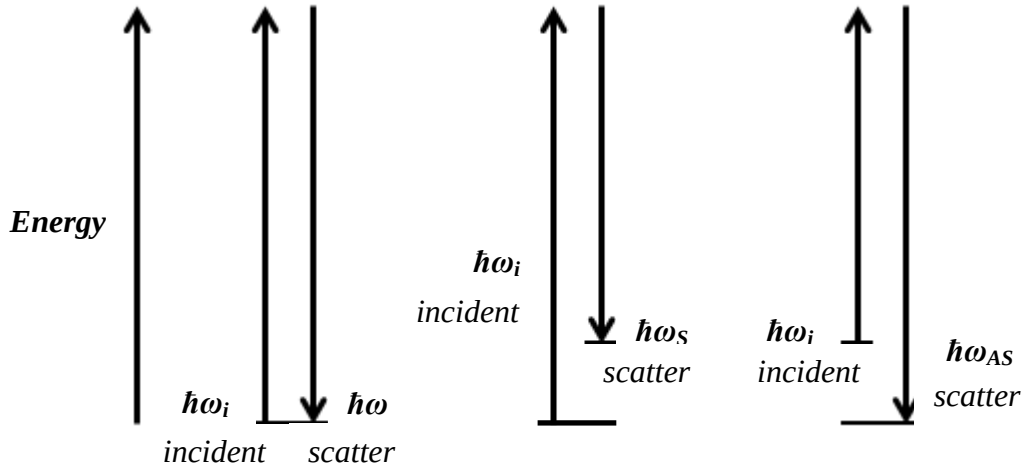

Figure 2.1: Illustration of scattering processes; Rayleigh where conservation of elastic light takes place; Raman Stokes where a phonon is annihilated and photon energy emitted is decreased; Raman Anti-Stokes where a phonon is adsorbed and photon energy emitted is increased.

As for practical use with graphene, Raman spectroscopy can provide a number of different uses for characterizing this material. First graphite, the derivative of graphene, exhibits two characteristic signature peaks that define this material. These two vibration

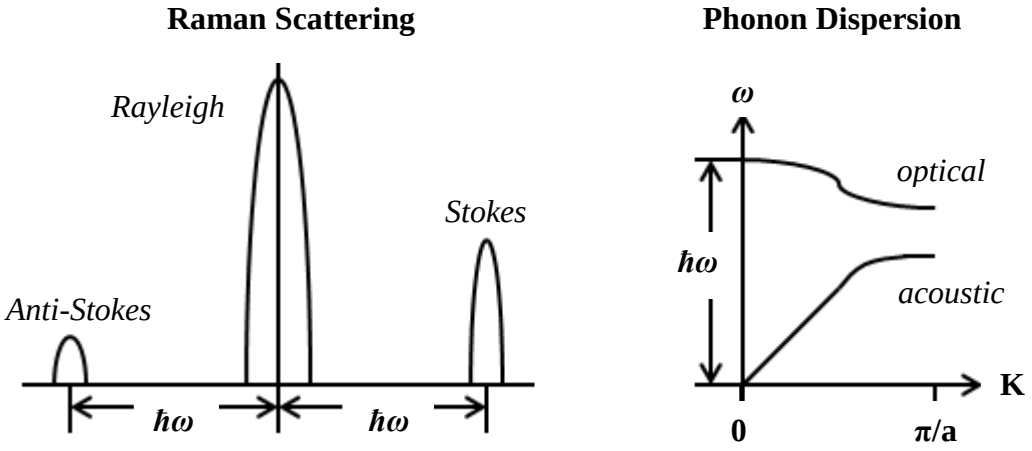

Figure 2.2: Illustration of Raman scattering (left) where inelastic light scattering takes place; a photon is emitted as a Stokes process where a phonon is released and a photon is emitted as an anti-Stokes process where a phonon is absorbed. Illustration of Phonon Dispersion (right) where the energy of the optical phonon matches that of the Raman scattering (left).

peaks include doubly degenerate zone-center G-peak at 1580cm^{-1} and G$^{'}$ peak at 2700cm^{-1} which has nothing to do with G-peak but is the 2nd order of zone-boundary phonons. If defects or impurities occur within the graphene layers, then a D-peak shows up at 1350cm^{-1} which can be explained by the double resonance model derived from Thomsen et al. [6]. Essentially the concept behind the double resonance model works by the following process: an incident photon is emitted (electron hole pair), a phonon of energy $\Delta\omega_{ph}$ is emitted as the photon is inelastically traversing (scattered) across the crystal lattice, if there is a defect then the photon is elastically back-scattered across the crystal lattice where a photon is emitted back (electron-hole recombination). This conservation of energy produces the double resonant condition. Meanwhile, regardless if elastic backscattering takes place, the photons backscatter and continue to scatter inelastically across the crystal lattice until they reach the zone-boundary phonon branch where the last photon is emitted (electron-hole recombination). Since the G$^{'}$-peak shows up at twice the

D-peak, we refer to the G'-peak as the 2D-peak for clarification. After normalization graphene layer counting can be observed by normalizing these peaks and then quantifying the G-peak to 2D-peak ratio intensity [6]. It was found that if this ratio (488nm laser atop SiO_2) was 1:4 then single layer graphene is observed, ratio of 2:1 to 1:1 then bi-layer graphene is observed, and below that ratio +1:1 then few-layer graphene to bulk graphite is observed shown by Ferrari et al. [7]. The G-peak is likely to decrease due to the interaction volume decreasing from the thinning of graphene layers. This peak focuses its vibration dependence mainly on in-plane movement due to the bond stretching of all pairs of sp^2 atoms in both rings and chains and not having to do much with out-of-plane vibrations [7]. The 2D-Peak is likely to increase because with the thinning of graphene layers out-of-plane movement is less suppressed. This peak focuses its vibration dependence to include out-of-plane movement due to its location near the K-point.

2.4 OPTICAL PROPERTIES

Graphene exhibits unique adsorption properties due to the Dirac point in the electronic band structure. Since electrons act effectively as relativistic massless fermions at low energy, the fine structure constant solely defines the opacity of suspended graphene as $\alpha = e^2 / \eta c \approx 1/137$ where c is the speed of light, e is the electron charge, and η is planck's constant [8]. The fine structure constant is a parameter that is customarily used in quantum electrodynamics to describe coupling between light and relativistic electrons. Graphene absorbs a large ($\pi\alpha$ = 2.3%) portion of white light which is due to its unique band structure which can be shown through calculating the adsorption of light using two-

dimensional massless electron gas with Fermi's golden rule [8] shown by Nair et al. Each additional layer of graphene exhibits decreases transparency by another 2.3% through adsorption which is miraculous from the thickness of graphene layers being only 0.34nm. Although, below λ<500nm there is slightly less transmittance noted due to hydrocarbon contamination [8].

Over the spectrum from UV to visible to FIR, the adsorption of large-area CVD grown graphene changes drastically consequently causing major optical changes over these three regions. In the uv-region an excitonic adsorption peak forms at $\eta\omega = 4.6eV$. In the infrared (IR) to visible region, a constant inter-band adorption of $\sigma_1(\omega) = e^2 / 4\eta$ independent of wavelength is seen. Lastly in the far-IR range a Drude peak is observed due to graphene having no free carrier when the Fermi level lies at the Dirac point unless there are charged impurities on the substrate to change this Fermi level [9].

Traditionally, the Fresnel coefficients are applied when observing the adsorption, transmittance, and reflectance of two interfaces of different refractive indices normal to the surface. Light propagating through two interfaces is explained traditionally by using Snell's law $\sin\theta_1/\sin\theta_2=n_2/n_1$ and law of reflection $\theta_1=\theta_1$, where incident angle $\theta_i=\theta_r$ reflected angle are generically modeled. When using multiple interfaces, each interface has to be factored into the equation including all reflections, adsorptions, and transmissions in order to accurately model the contrast change between the substrate the medium of interest. The most common way to calculate this is by using the transfer matrix method [10]. For our purposes, we look at the layered structure of graphene on 300nm of SiO_2 on >500nm of Si. Index of refraction of each material, thickness, and

wavelength play a significant role in the overall contrast of graphene on top of substrates. Although suspended graphene may appear to adsorb 2.3% of light, when graphene is coupled to a substrate the optical properties change due to the substrate materials having different index of refraction values changing with wavelength due to its dependency vs. graphene which is wavelength independent over the visible spectrum. Stacked mediums and their corresponding refraction indices e.g. the index of refraction of air is 1 and graphene is 2.6-1.3i (takes from in-plane bulk graphite) which are both wavelength independent, whereas SiO_2 and Si are wavelength dependent which change their index of refraction at different wavelengths within the visible spectrum are modeled in Blake et al. [11]. Overall contrast is measured by $C = I(n_1=1) – I(n_1\neq1)/I(n_1=1)$ where I is the relative intensity of reflected light with graphene ($n_1\neq1$) and without graphene ($n_1=1$) which is displayed over the visible spectrum for various thicknesses of SiO_2 [11]. In Blake et al. clear demonstration shows the highest contrast difference that graphene exhibits from its substrate peaks at specific wavelengths rather than white light flooding the entire λ spectrum. The use of a bandpass notch filter can help achieve a narrow λ for achieving the most contrast visibility by focusing on thicknesses chosen through modeling to maximize optical constructive interference allowing enhanced contrast between each graphene layer and the substrate its coupled to [11]. Thereby, appearing with 12% contrast in some cases as in λ=560nm on top of 300nm SiO_2 or eliminating optical interference making graphene layers completely invisible [11].

2.5 IMAGE PROCESSING OVERVIEW

The following is a conceptual image processing overview relevant to this work since the materials science discipline is largely unrelated to the image processing discipline. Overall, image processing entails capturing an image with a camera CCD (Charge-Coupled Device), where individual pixels of the image are analyzed through computational algorithms. Figure 2.3 shows an overview of pixel analysis from a captured image with a caption elaborating on these details.

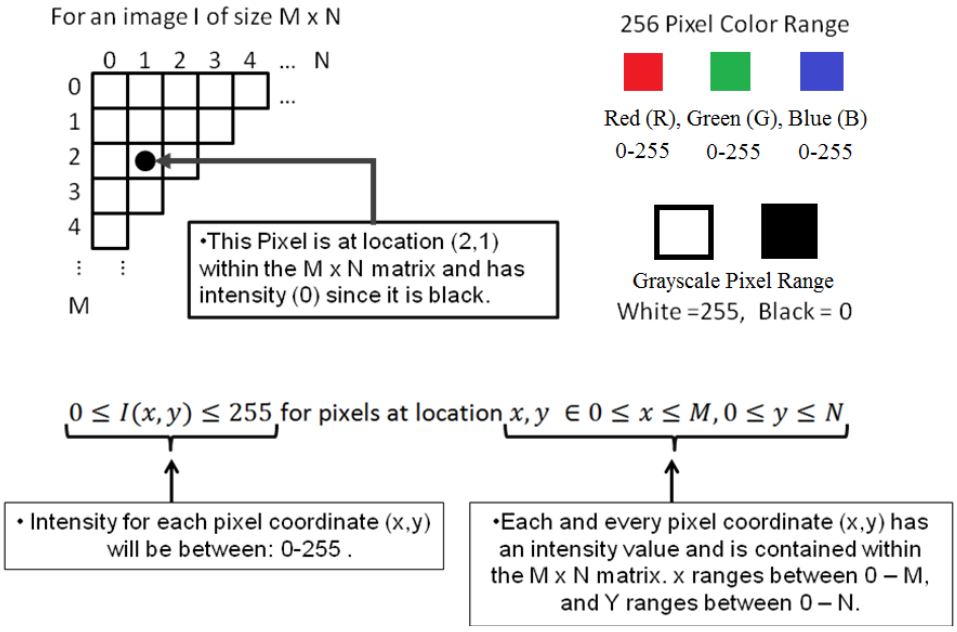

Figure 2.3: Computational input of a captured image includes; breakdown of an image into individual pixels with size M x N at location (x,y), the values (red, green, blue (RGB)) or value (grayscale contains a percentage of RGB values) of each pixel between 0-255 range.

Numerous computational algorithms can be utilized with only the limitation of processing time for analysis of captured images. The large array of statistical analysis that can be performed is innumerable which would be beneficial for industrial inspection of

graphene growth over wafer-sized substrates. This would also help to improve CVD graphene growth processes as mentioned previously. Ultimately, image processing for materials science applications is inexpensive (cost of computer and developing software) comparative to most other quality control methods used in industry.

2.6 GRAPHENE PRODUCTION: EXFOLIATION TO GROWTH

Initial experimental studies of graphene consisted of mechanical exfoliation (rubbing adhesive "scotch tape" from highly oriented pyrolythic graphite (HOPG) to a substrate) limited to small-areas in 2004 [12, 13]. Graphene growth processes quickly followed and within 6 years, a 30-inch roll-to-roll fabrication process of large-area CVD graphene was developed for commercial applications [14]. The outcome of this fabrication process produces large-area graphene films that can be pressed onto any target substrate of interest. The first prototype of a graphene-based touch-screen panel from this process was debuted at the Computer Electronics Show in Las Vegas, 2010 [14] as well as the development of a prototype of a flexible transparent graphene-based electrode.

Although few large-area graphene-based applications have been actualized, many high interest potential devices have yet to be produced due a number of limitations concerning CVD graphene growth. So far, large grain sizes of up to 100μm have been grown with virtually limitless areas of fabrication where 30-inch area rolls have been produced [14]. Also, optical characterization remains consistent for exfoliated graphene vs. CVD grown graphene by having the same adsorption of 2.3% for each graphene layer as the index of refraction remains constant for the visible spectrum independent of

wavelength [14]. One major issue remains, uniformity of graphene layering over a large-area. This is important due to the suppression of properties between the sheets of different graphene layers outlined previously in the motivations section of this document. In Bae et al. [14] one can see that there is no consistency of uniform layering for graphene over a 10μm region for the 30-inch rolls of CVD graphene which produced the graphene-based touch screen panels. Furthermore, the current progress of CVD graphene grown on Ni ranges from 3-6 layers and 1-3 layers on Cu which are all non-uniform without consistent layering control [15]. Different colorations in Reina et al. [15] show non-uniform graphene layering representing a clear reliability problem of same layered graphene growth due to the random and uncontrolled layering growth.

Issues in large-area characterization of CVD grown graphene also presents some limitations. In one example Raman spectroscopy which is the most robust method for graphene characterization is limited to a small scanning spot size of a few micrometers. It would be time consuming to acquire the Raman spectrum for a large-area flake. Furthermore, the Raman spectroscopy method is limited to FLG films with the number of atomic planes smaller than n=5-7. For thicker films the Raman spectrum becomes too close to that from bulk graphite. There are also indications that Raman spectroscopy becomes less efficient for CVD graphene rather than for mechanically exfoliated graphene. The latter is explained by the increased $\pi - \pi^*$ bond stacking order [14], which intensifies 2D peak from the out-of-plane modes and preserves G peak of the in-plane modes, thus changing the well known G peak to 2D peak intensity ratio [6, 16, 17] and complicating interpretation of the Raman spectrum.

REFERENCES

1. H. Weller, *Advanced Mater.* **5**, 88 (1993).
2. A. Henglein, *Progr. Colloid Polymer Sci.* **73**, 1 (1987).
3. A. H. Castro Neto, F. Guinea, N. M. R. Peres, K. S. Novoselov, and A. K. Geim, *Rev. Mod. Phys.* **81**, 109 (2009).
4. P. R. Wallace, *Phys. Rev.* **71**, 622 (1947).
5. C. V. Raman and K. S. Krishnan, *Nature* **121**, 501 (1928).
6. C. Thomsen and S. Reich, *Phys. Rev. Lett.* **85**, 5214 (2000).
7. A. C. Ferrari, *Solid State Comm.* **143**, 47 (2007).
8. R. R. Nair, P. Blake, A. N. Grigorenko, K. S. Novoselov, T. J. Booth, T. Stauber, N. M. R. Peres, and A. K. Geim, *Science* **320**, 1308 (2008).
9. C. Lee, J. Y. Kim, S. Bae, K. S. Kim, B. H. Hong, and E. J. Choi, *App. Phys. Lett.* **98**, 071905 (2011).
10. O. S. Heavens. *Optical Properties of Thin Films.* Butterworth, London (1955).
11. P. Blake, E. W. Hill, A. H. Castro Neto, K. S. Novoselov, D. Jiang, R. Yang, T. J. Booth, and A. K. Geim, *Appl. Phys. Lett.* **91**, 063124 (2007).
12. K. S. Novoselov, A. K. Geim, S. V. Morozov, D. Jiang, Y. Zhang, S. V. Dubonos, I. V. Grigorieva, and A. A. Firsov, *Science* **306**, 666 (2004).
13. K. S. Novoselov, D. Jiang, F. Schedin, T. J. Booth, V. V. Khotkevich, S. V. Morozov, and A. K. Geim, *Proc. Natl. Acad. Sci.* **102**, 10451 (2005).

14. S. Bae, H. Kim, Y. Lee, X. Xu, J. S. Park, Y. Zheng, J. Balakrishnan, T. Lei, H. R. Kim, Y. Song, Y. J. Kim, K. S. Kim, B. Ozyilmaz, J. H. Ahn, B. H. Hong, and S. Iijima, *Nature Nanotechnology* **5**, 574 (2010).
15. A. Reina, X. Jia, J. Ho, D. Nezich, H. Son, V. Bulovic, M. S. Dresselhaus, and J. Kong, *Nano Lett.* **9**, 1 (2009).
16. A. C. Ferrari, *Solid State Commun.* **143**, 47 (2007).
17. D. M. Basko, *Phys. Rev. B* **76**, 081405(R) (2007).

Chapter 3

Material Layer Identification Technique

From the beginning stages of the semiconductor industry, metrology tools and techniques have evolved significantly over time as new technologies bring demand for ever growing changes to present measurement schemes. The aim of this work focuses on an important challenge recently plaguing a high interest research area revolved around quasi-two-dimensional materials, which is to investigate via experimental research to provide a metrology tool for high throughput large-area atomic layer identification. Since characterization metrology goes hand-in-hand with understanding the makeup of any material, an additional study is given to provide further details on the specific materials used.

Results achieved in this chapter include the completion of an automated identification method for detecting graphene and graphene multilayers for use in a large-area for mechanically exfoliated graphene originating from HOPG bulk ingot and for CVD grown graphene on top of a Ni substrate. Expansion was extended to the identification other atomically-thin layered materials, namely bismuth telluride family of materials (Bi_2Te_3 FOM), which exhibits similar adsorption patterns. Robust characterization of these materials were measured for 80-90 different points blindly to ensure the quality and reliability this technique and methodology.

3.1 AUTOMATED IDENTIFICATION METROLOGY TECHNIQUE *VIA* IMAGE PROCESSING

Here we describe a process for the large-area graphene identification and quality control that is automated, cheap, robust, high-throughput, time-effective and highly efficient. The technique is based on a combination of the modified optical contrast method with several optical filters and image processing algorithms. The calibration of the process is carried out using micro-Raman spectroscopy. The overall approach is illustrated in Figure 3.1

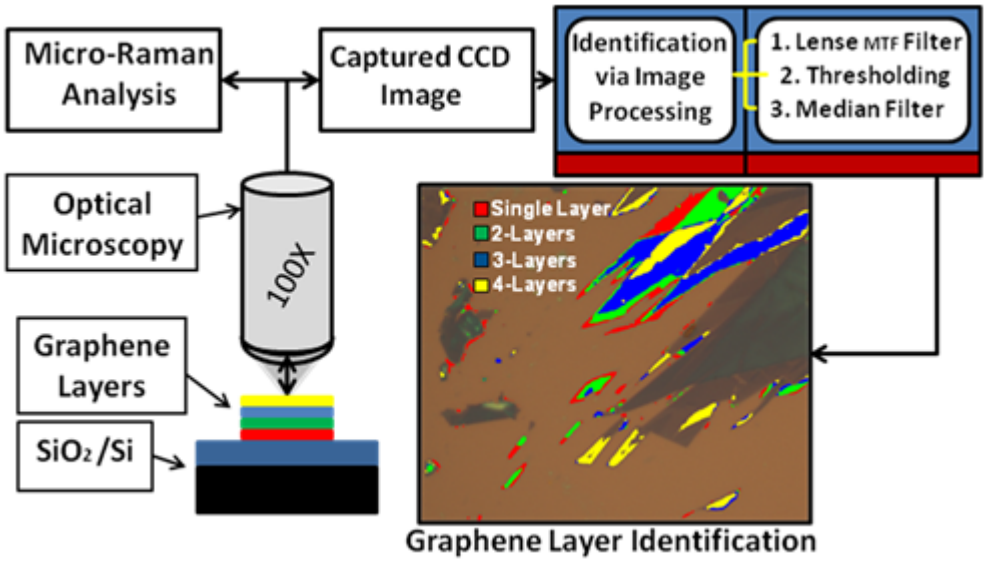

Figure 3.1: Schematic of the process for determining the number of layers in graphene and few-layer graphene films. The image of graphene sample is acquired via optical microscope, followed by micro-Raman calibration, background subtraction, light non-uniformity correction, and application of the original image processing algorithm to identify the regions with different number of atomic planes and map them with pseudo-colors. (Reprinted with permission from C. M. Nolen et al., ACS Nano **5**, 914 (2011). Copyright (2011) American Chemical Society.)

which shows a schematic of the process starting from a captured image via an optical microscope, micro-Raman calibration, and image processing algorithm, which completes the recognition process. Below we provide a detailed step-by-step description of the

process, which allows one to count the number of atomic planes (graphene layers) for a large-area and clearly identify the borderlines between regions with different thickness (i.e. number of atomic planes).

3.2 GRAPHENE IDENTIFICATION: SIX STEP PROCESS

To test the recognition process we prepared a large number of samples with graphene films. Graphene and FLG were produced by the standard mechanical exfoliation from HOPG and placed on top of the SiO_2 (300 nm)/ Si substrate [1, 2]. It is known that the 300-nm thickness of SiO_2 allows one to visualize FLG regions under regular light conditions [3-5]. The high resolution optical microscopy images of the samples were captured by a digital camera attached to an optical microscope (Nikon Eclipse LV150) in "white" light produced by a quartz tungsten halogen light source.

Step 1: We start by capturing two optical images. The first is of the substrate material (usually SiO_2/Si but other substrates are also suitable) while the second image is of the FLG sample on the same substrate or different substrate made from the same material (see Figure 3.2). We intentionally selected samples with FLG regions containing different number of atomic planes n and having irregular shape boundaries. For convenience, we use the following notation: substrate without graphene – Image O and substrate with graphene – Image I.

Figure 3.2: Microscopy images of the substrate (left panel) and FLG on substrate (right panel) obtained with 100X-objective. The image O is used for the background subtraction – a required step for the large area graphene identification. Image I is used for the overall for graphene layer identification experiment. (Reprinted with permission from C. M. Nolen et al., ACS Nano **5**, 914 (2011). Copyright (2011) American Chemical Society.)

Step 2: We perform the calibration procedure, which can be done locally on a selected region where visual inspection suggest a presence of SLG, BLG, etc. This step involves collection of Raman spectrum from a few spots or performing a Raman line-scan. Raman spectroscopy has proven to be very reliable for identification of FLG with n=1, 2, 3, 4 and 5 via deconvolution of 2D band and measuring the ratio of the intensities I(G)/I(2D). In most of cases, a single line scan is sufficient to identify at least one spot for each n. The coordinates of the spots, corresponding to n=1, 2, 3, 4, and 5 are recorded and correlated with the color information obtained in the previous step (both on Image O and Image I). This procedure accomplishes the labeling of several spots with the number of atomic planes (see Figure 3.3). This calibration step does not take much time because it is done locally and does not need to be repeated for the whole substrate coated with graphene or the whole wafer with CVD grown graphene. Moreover, once it is done for graphene on a certain substrate it can be omitted for other graphene samples on the same

type of the substrates under the same illumination. We verify the Raman calibration via atomic force microscopy (AFM) inspection for randomly selected samples.

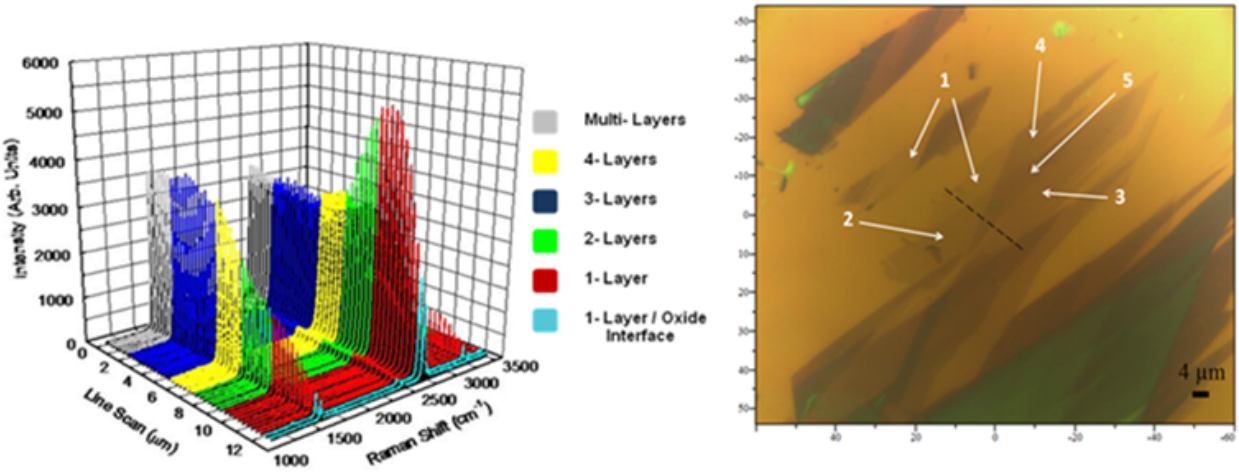

Figure 3.3: Raman line-scan showing the characteristic G peak and 2D band used for identification of the number of atomic planes n in FLG regions (left panel). The colors denote FLG with the number of planes varying from 1 to 4 and above. The Raman scans were taken along dotted line (12.5μm length) indicated on the right panel. The white numbers label the number of atomic planes in different regions of FLG sample (right panel). (Reprinted with permission from C. M. Nolen et al., ACS Nano **5**, 914 (2011). Copyright (2011) American Chemical Society.)

This procedure completed the preliminary (i.e. calibration steps) that do not have to be repeated for each new sample if the substrate and light conditions are kept the same. The following steps constitute the image processing algorithm applied to the captured optical images (Image I and Image O). In order to describe these steps ones needs to define and introduce a few concepts and variables, commonly used in image processing. We begin by noting that each optical image can be broken into a matrix of pixels with dimensions $M \times N$, where pixel row and column locations are in the range of $x, y \in 0 \le x \le M$, $0 \le y \le N$. Each pixel is assigned a light intensity in the range

$I_{\min} \le I(x,y) \le I_{\max}$ for a given light source intensity. Here, $I_{\max}$ is the maximum intensity allowable (conventionally assumed to be 255), and $I_{\min}$ is the minimum intensity allowable (conventionally assumed to be 0), while *x* and *y* indicate the row and column (or coordinates) of the locations being computed. The intensity of each pixel can be represented as a combination of red (R), green (G), and blue (B) intensity values: $I(x,y) = [I_R(x,y), I_G(x,y), I_B(x,y)]$, where I_R is the red intensity value, I_G is the green intensity value, and I_B is the blue intensity value. With this in mind we can proceed to the next step.

Step 3: Since the main motivation for this research is development of the automatic scalable technique for large-area graphene wafers, one needs to take into account the non-uniformity in wafer illumination. The optical images are taken using optical microscopes and unavoidably affected by the objective lenses, which do not produce uniform intensity of lighting throughout the image. The light is at its maximum intensity at the focal center and is the dimmest at the corner edges of the image. The illumination of the lighting non-uniformity is accomplished with the help of the reference substrate image (Image O). The intensity profile is found from Image O (see Figure 3.4) and then subtracted from Image I. This equalizes the lighting conditions over the whole substrate for the following image processing steps. The details of the non-uniform lighting removal process are given in the Methods section (see Section entitled *Non-Uniform Lighting Elimination*).

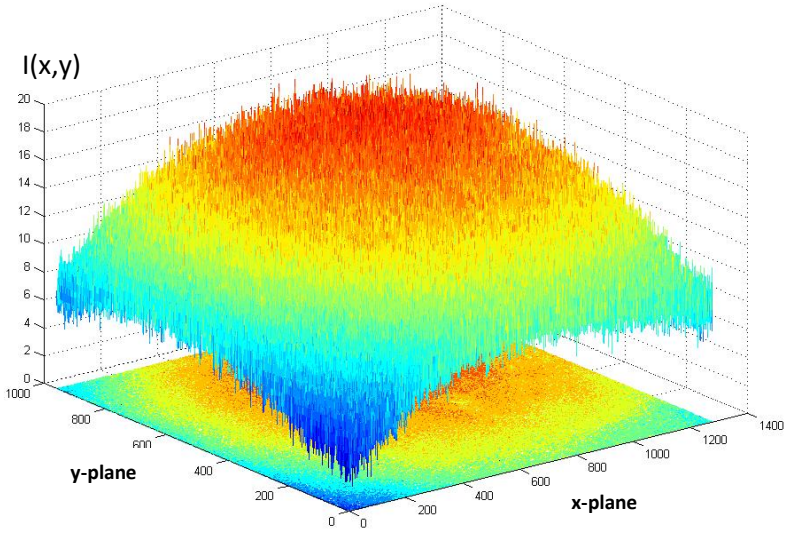

Figure 3.4: Non-uniform illumination intensity I(x, y), expressed in arbitrary units, is shown as a function of the substrate coordinates x and y. The non-uniformity caused by the circular confocal lens aberration is corrected by the lens modulation transfer function (L_{MTF}) filter introduced to the recognition procedure. (Reprinted with permission from C. M. Nolen et al., ACS Nano **5**, 914 (2011). Copyright (2011) American Chemical Society.)

Step 4: Once the uniformity of light illumination is achieved for the whole image one can extract the contrast information for different FLG regions (referenced to the background). To conduct such a process for Image I, we define the red, green, and blue (RGB) values for each pixel of the image. From the step 2, we know what RGB values correspond to regions with n=1, 2, 3, 4 or 5 (see Figure 3.3). This determines the range of RGB values that ensure that the region has the number of atomic planes within n=1-5. Using this information we identify regions of FLG throughout the whole image or wafer. After we have specified all FLG regions of interest (e.g. with n<4) in pixels within $M \times N$ we can exclude all other thicker regions (e.g. with n>4). The exclusion is based on

subtracting all points of the image that have RGB levels above or below the allowable RGB previously specified for each *n* (see Figure 3.5). The detail algorithm for the RGB assignment and image processing exclusion of regions that do not belong to the needed n range are described in the Methods section (see *Background Subtraction*).

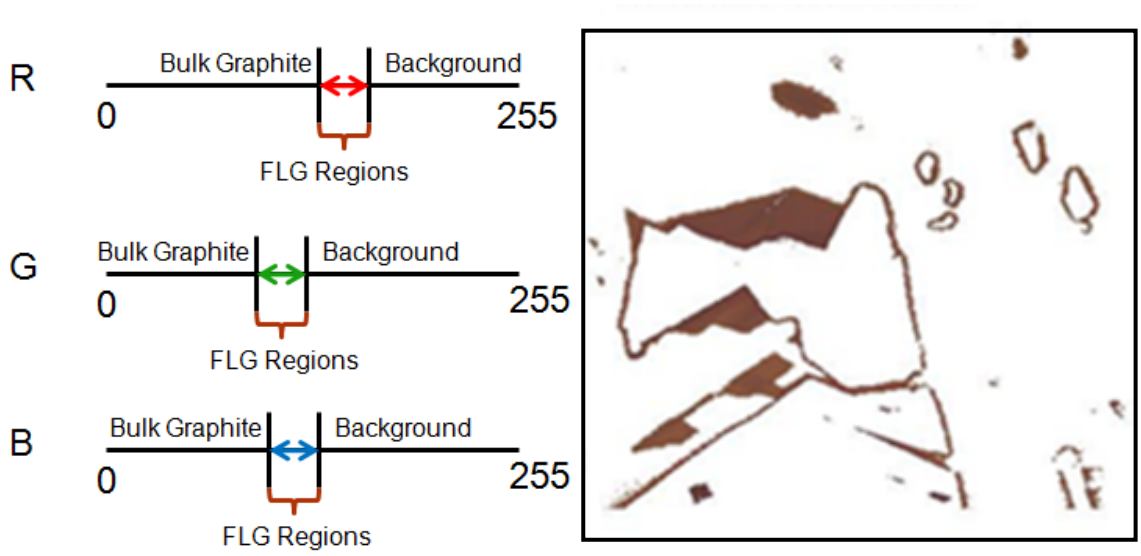

Figure 3.5: Range of the red, green and blue (RGB) light intensity values that corresponds to the FLG regions (left panel). The RGB ranges can be used for the background subtraction and exclusion of the regions with thicker films (e.g. bulk graphite). Optical image (100X magnification) after RGB processing, which restricted the light intensity values to FLG regions (right panel). Only the dark regions consist of FLG with *n*=1-4, the rest of the regions (white) are either substrate or thicker films (e.g. bulk graphite). (Reprinted with permission from C. M. Nolen et al., ACS Nano **5**, 914 (2011). Copyright (2011) American Chemical Society.)

Step 5: We can now refine the recognition process and perform identification of each graphene layer (with specific *n*) from the determined FLG regions. To accomplish this task we start by converting the RGB data (defined for FLG regions in Image I) that contains 3 values per pixel to the grayscale that contains 1 value per pixel. The latter is accomplished through the process called segmentation (see Methods section entitled

Graphene Layer Identification). We label the grayscale contrast range for FLG regions, defined as $\Sigma\Delta I_n$, and find the minimum – maximum boundary range for the graphene layers with specified *n* (see Figure 3.6). The intensity range for graphene layers with a given *n* is labeled as ΔI_n (it is contained within $\Sigma\Delta I_n$ range). The use of grayscale can only be efficient for FLG regions after removal of the background and regions that correspond to the thick graphitic films.

The optical adsorption of each graphene layer for different brightness intensities is shown in Figure 3.6, where ΔI_n contains the range of the light intensity values associated with a specific graphene layer of interest (specified by a given *n*) and $\Sigma\Delta I_n$ shows the light intensity range of values for the entire FLG region. The range of these light intensity values depends on the brightness of the light source of the optical microscope. The dependence of ΔI_n on the intensity of the light source is important for this automated identification process.

For clear visual recognition, the unique pseudo colors are assigned to the contrast ranges ΔI_n for each graphene layer with a given *n*. This is done by further filtering out separately the regions for SLG, BLG, and FLG with *n*=3 and 4 from the grayscale FLG region. In Figure 3.7, we show how such filtering results in the separated regions. The white spots correspond to the regions with a specific number of atomic planes *n*. The entire M x N transparent image with identified pseudo colored regions is then laid on top of the original optical image (Image I), for visual identification of FLG regions with

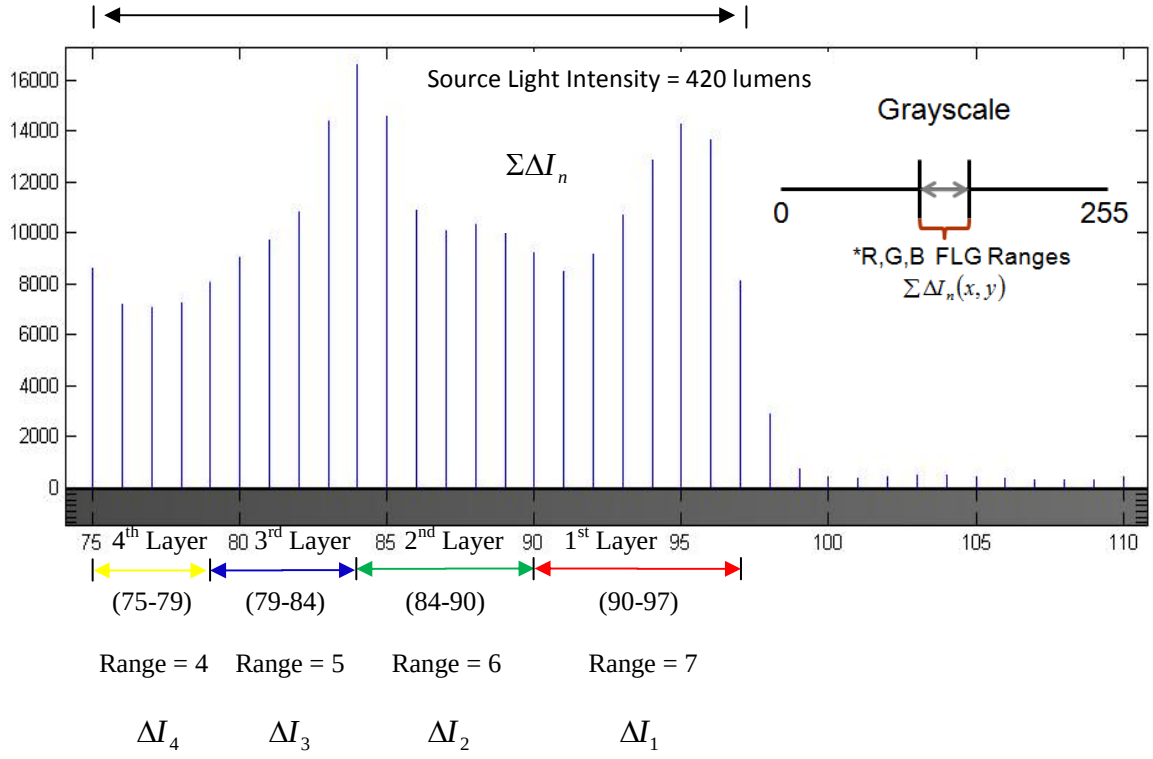

Figure 3.6: Illustration of the conversion process of RGB values to the grayscale (upper panel). The grayscale allows for easier identification of the regions with a specific number of atomic planes *n*. The grayscale range of FLG is sectioned into the respective light intensity ranges for each individual layer of graphene with a given *n* (lower panel). (Reprinted with permission from C. M. Nolen et al., ACS Nano **5**, 914 (2011). Copyright (2011) American Chemical Society.)

desired *n*. The mathematical details of the process are described in the Methods section (see *Graphene Layer Identification*).

***Step 6*:** The graphene identification procedure is completed with an application of the median filter and utilization of pseudo colors for better visualization. The median filtering step involves the statistical pixel-to-pixel neighboring analysis technique to improve the image resolution within the identified region and clarify the boundaries

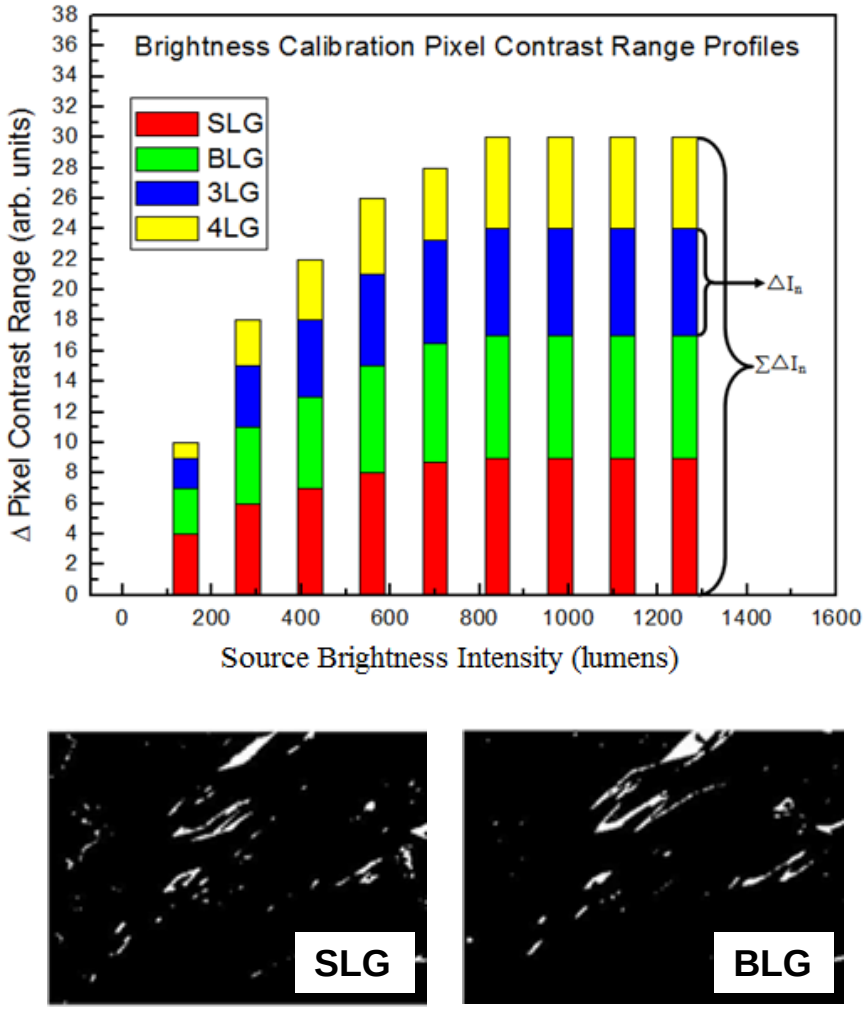

Figure 3.7: Optical brightness ranges ΔI_n associated with a specific graphene layer of interest (defined by *n*) and combined range $\Sigma\Delta I_n$ for the entire FLG region shown as functions of the source brightness (upper panel). The white spots on the sample surface are identified regions of SLG (n=1) and BLG (n=2) (lower panel). The dark background is the rest of the sample surface (i.e. regions of substrate without graphene or regions with other thicknesses). The presented technique can be used for wafer size samples without any major modification or processing time increase. (Reprinted with permission from C. M. Nolen et al., ACS Nano **5**, 914 (2011). Copyright (2011) American Chemical Society.)

between any two regions with different number of atomic planes *n* (see also the *Median Filter* in the Methods section). The median filter allows one to eradicate the high frequency impulse noise commonly known in image processing as "salt and pepper" noise. In our approach, this noise may cause the identified regions of graphene to appear patchy reducing the accuracy when determining the borderlines of the regions. After the filtering process, we assign the pseudo-color to each region with a given *n*, and present the final result on the sample map (see Figure 3.8). This map clearly marks the number of atomic planes at each location of the sample surface by color: red, green, blue or yellow. The remaining brown regions are the substrate itself without graphene flakes while the dark regions are the thicker graphite films.

It is easy to see that the approach can be extended to the wafer size or rolls of CVD graphene on flexible substrates. Since the only size limitation is the area of the optical image our approach is suitable for industry scale high-throughput applications. The high speed of the image processing algorithms allows for the *in situ* identification of the number of atomic planes. As a result, the throughput for the industrial scale inspection of many wafers will be determined by the speed of mechanical motion of the wafers to and from the light source. A similar scale of the graphene identification cannot be achieved with Raman spectroscopy. The two-dimensional Raman scan of the whole sample surface will be extremely long time (the spectroscopic data accumulation for each point on the sample surface takes from ~1 minute to ~30 minutes with conventional spectrometers). The lateral resolution of Raman spectrometers is determined by the laser spot size, which is on the order of 0.5 – 1.0 μm. In our approach, Raman

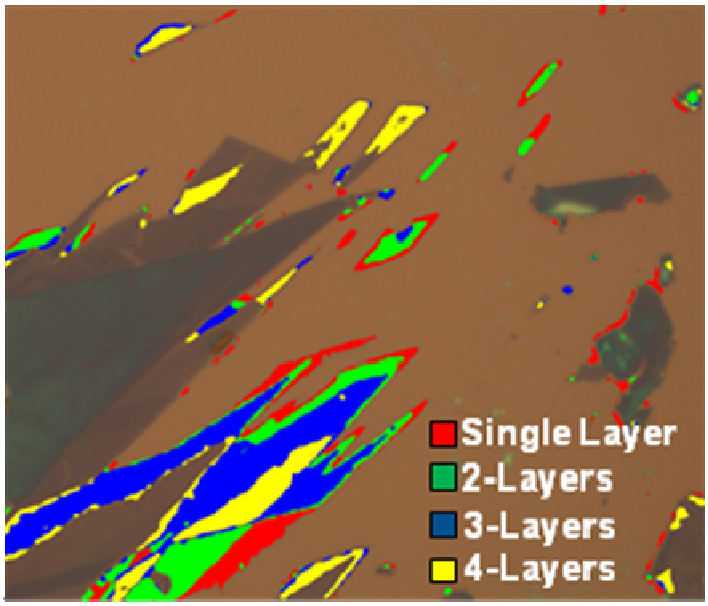

Figure 3.8: Statistical nanometrology layer counting analysis is performed by sectioning out a specific individual graphene layer different from the bulk, substrate, and other graphene layers. (Reprinted with permission from C. M. Nolen et al., ACS Nano **5**, 914 (2011). Copyright (2011) American Chemical Society.)

spectroscopy is used only for the calibration of the process and can be done locally on a few stops or via a line scan.

The versatility of our metrology technique opens a door for a plethora of experimental and industrial applications. It can be applied to a number of various substrates and graphene samples produced by different methods [6-8]. Instead of micro-Raman spectroscopy, other calibration techniques can be used instead. We have tested this method on a large number of graphene samples produced by mechanical exfoliation. In some cases we intentionally used contaminated substrates and FLG flakes that had a large thickness variation (from SLG to bulk graphite). Our technique worked fine for all examined substrates. Moreover, we have tested our approach for another type of

atomically-thin materials – topological insulators of the bismuth telluride family [9-14]. The "graphene-like" exfoliated atomically-thin films of Bi_2Te_3 and Bi_2Se_3 [9-12] were placed on top of Si/SiO_2 substrates. The graphene identification technique performed for this type of samples as well. The accuracy of our technique can be enhanced further by application of other image enhancing, error reducing algorithms implemented in different software packages. Additional post-processing algorithms can provide further detection of through various statistical analyses revealing important characteristic parameters of the investigated graphene such as type of edge termination i.e.; zigzag or armchair graphene which would ultimately change the electronic state as being metallic or semi-conducting. An example of additional post-processing can be seen in the left side of Figure 3.9 where the entire image is classified from each graphene layer to the substrate and bulk. Then percentage coverage area for each graphene layer is deduced and plotted in the right side of Figure 3.9. Image processing applications in semiconductor industry have already helped to achieve major improvements in materials processing and chip fabrication at reduced cost [15]. The proposed large-scale graphene identification and quality control technology can become particularly useful for the newly developed graphene synthesis techniques [16, 17] and graphene practical applications in heat spreaders, interconnects and analog electronics [18-21].

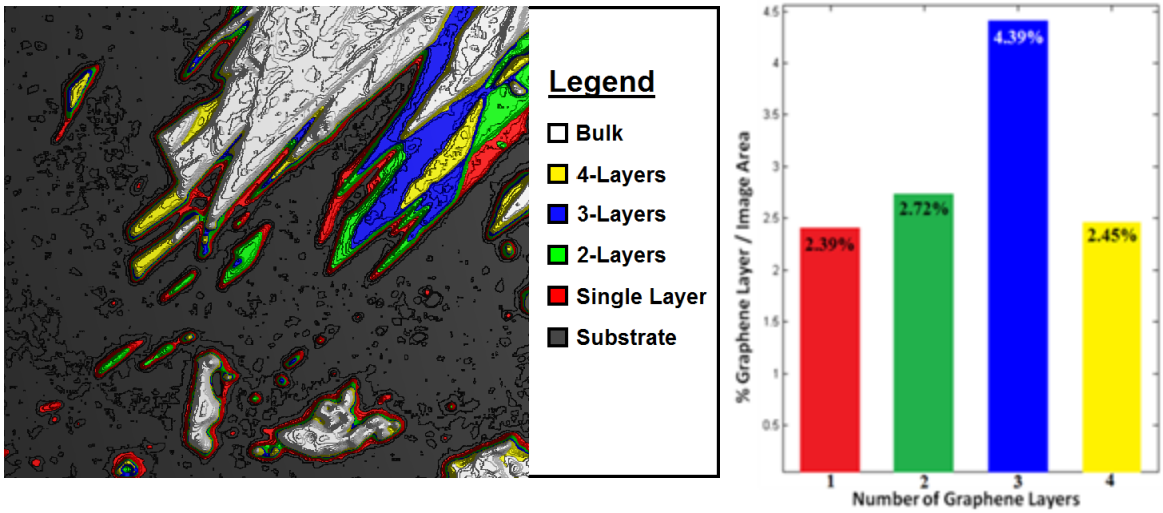

Figure 3.9: Image processing allows for clear identification and recognition of graphene layers (left panel). By altering the color schemes of identification pattern, we show that percent yield of each graphene layer (right panel) can be deduced through statistical analysis of each colored region within a designated area. (Reprinted with permission from C. M. Nolen et al., ACS Nano **5**, 914 (2011). Copyright (2011) American Chemical Society.)

3.3 METHODS

This section is divided into sub-sections, which provide details for specific steps of the large-scale graphene identification and quality control technique.

Non-Uniform Lighting Elimination

This description is pertinent to Step 3 of the procedure. To eliminate the non-uniform lighting across Image I, we apply a special filter, which subtracts the light intensity extracted from the background Image O. This is based upon the assumption that under perfect condition, the color intensity of the substrate is uniformly the same across the image. The whole procedure is presented step-by-step in Figure 3.9. It starts with accumulation of the typical light intensity distribution for Image O along the x or y axis.

This intensity distribution is non-uniform with the maximum attained usually around the center of the image. The distribution is modified by subtraction of the uniform background. The resulting non-uniform part is inverted and stored for further use with Image I. The next step is accumulation of the typical intensity distribution for Image I (the actual graphene sample on the substrate). The addition of the inverted light intensity, obtained for the reference Image O, to the intensity distribution in Image I results in the corrected intensity distribution for Image I with eliminated lighting non-uniformity (shown in the lower right panel in Figure 3.10).

Mathematically, this process is described as an application of the lens modulation transfer function (L_{MTF}) filter [22]. The filter corrects the circular lens aberration produced by the Gaussian-like distribution of non-uniform light intensity in both the x and y planes of Image I (see Figure 3.4 and 3.10). The application of the L_{MTF} filter is performed with the equation;

$$I_{n,C\in R,G,B}(x,y) = I_{C\in R,G,B}(x,y) - L_{MTF} \tag{1}$$

for each value I_R, I_G, I_B where $L_{MTF} = O_{C\in R,G,B}(x,y) - \min(O_{C\in R,G,B})$. The intensity function I_n now contains the corrected image with the evenly distributed light intensity across the entire image.

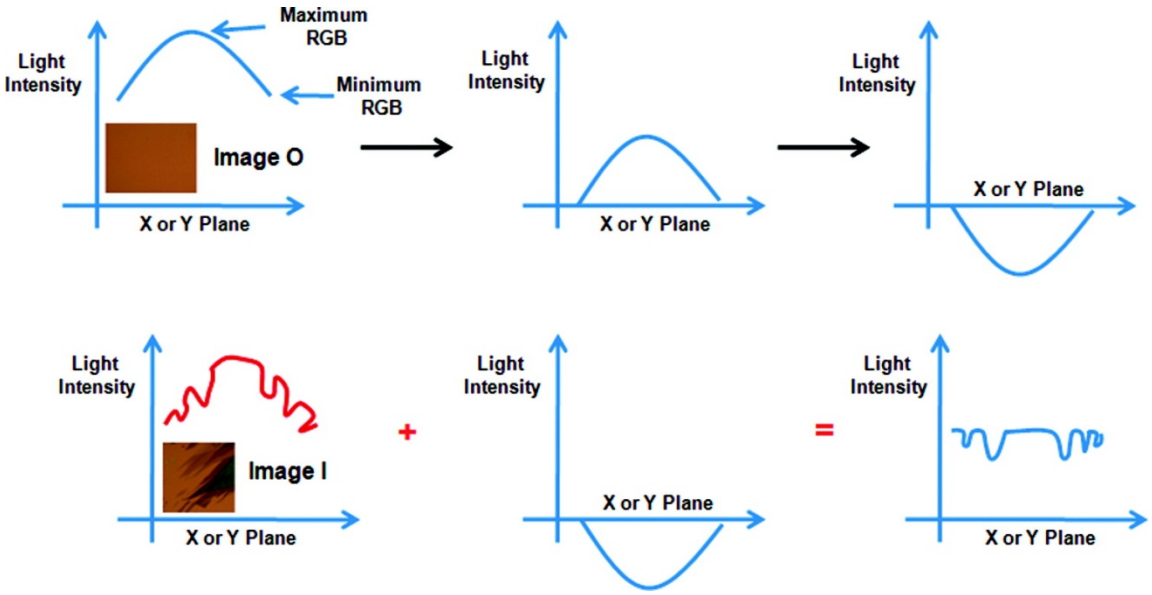

Figure 3.10: The upper left panel shows a typical non-uniform light intensity distribution for Image O along the *x* or *y* axis. The upper central panel is the non-uniform light intensity, which is left after subtraction of the uniform background lighting. The upper right panel shows the inverted light intensity obtained in the previous step. This completes the processing of data extracted from Image O. The lower left panel is a typical intensity distribution for Image I along the *x* or *y* axis. The modulation of the intensity profile is due to the presence of graphene flakes with different number of atomic planes. The addition of the inverted light intensity, obtained for Image O (upper right panel), to the Image I light intensity results in the final intensity distribution for Image I with eliminated lighting non-uniformity. The final result is shown in the lower right panel. (Reprinted with permission from C. M. Nolen et al., ACS Nano **5**, 914 (2011). Copyright (2011) American Chemical Society.)

Background Subtraction

This procedure is pertinent to Step 4. In order to subtract the background, we subtract the RGB value from all pixels that correspond to the same location in Image O and Image I. If the result is ~ 0, then the pixel in Image I is assumed to be a background pixel, in which case we change that RGB pixel value to white corresponding to (0, 0, 0). If the result is 1, then the pixel in Image I is assumed to not be a background pixel, in which case we do not change that RGB pixel value, retaining its original RGB value. This is

accomplished by performing the following procedure;

$$\mathrm{M}(\mathrm{x},\mathrm{y})=\begin{cases}0 \ if \ O_{C\in R,G,B}(x,y)-I_{C\in R,G,B}(x,y)\approx 0\\ 1 \ if \ O_{C\in R,G,B}(x,y)-I_{C\in R,G,B}(x,y)\neq 0\end{cases}, \tag{2}$$

where M contains the filter resulting from Image I with the substrate background subtracted. Next, by using the light contrast information from Figure 3.2, we can restrict each RGB value to only allow the light intensity range for FLG regions shown in Figure 3.5.

Graphene Layer Identification

This procedure is pertinent to Step 5. To perform the identification of graphene layers (i.e. distinguish SLG from BLG, etc.), each pixel in the entire image needs to be "segmented" [23] from RGB colors into a grayscale color. This makes the graphene layer extraction process simpler by converting three RGB values per pixel into one grayscale value per pixel, which comprises of a different percentage of each RGB value. The grayscale conversion is completed by changing the M regions of interest to grayscale and changing all other pixels that are not within the FLG contrast range to white by performing the following actions

$$I_{n,Gry}=0.30I_{n,R}+0.59I_{n,G}+0.11I_{n,B}$$

$$I_n(x,y)=\begin{cases}255 & if \ M(x,y)=0\\ I_{n,Gry}(x,y) & if \ M(x,y)=1\end{cases}. \tag{3}$$

Here I_n is an image containing only FLG. Next, the regions with specific number of atomic planes n (e.g. SLG or BLG) are determined from their grayscale light intensity range acquired from the optical Image I. The latter is achieved by applying the neighborhood thresholding [23], which allows one to extract the light intensity contrast range for each individual graphene layer with given *n* by performing the following operation;

$$\Sigma\Delta I_n(x,y)=\begin{cases}1 & L1_{\min}\le\Delta I_1(x,y)\le L1_{\max}\\ 2 & L2_{\min}\le\Delta I_2(x,y)\le L2_{\max}\\ 3 & L3_{\min}\le\Delta I_3(x,y)\le L3_{\max}\\ 4 & L4_{\min}\le\Delta I_4(x,y)\le L4_{\max}\\ 0 & other\end{cases} . \quad (4)$$

Here $\Sigma\Delta I_n$ represents the summation of the light intensity ranges for FLG regions containing each of the grouped layers and ΔI_n is the light intensity range for a specific graphene layer of interest, L1 is SLG, L2 is BLG, and L3, L4 are FLG with *n*=3 and *n*=4, respectively. The minimum and maximum values span the light intensity threshold range for each graphene layer (with given *n*). This process is repeated over the entire range of the source light intensities in order to provide a calibration lookup table for the image processing algorithms. As a result, the image processing algorithm can section out the graphene light intensity ranges for any light source intensity. The unique pseudo colors are then assigned to each graphene layer and overlaid atop of the original image for clear visual identification. The unique colors are assigned to the rest of the image, which include regions of the substrate or bulk graphite.

Median Filter

This procedure is pertinent to Step 6. To achieve the precision sufficient for the large-scale industrial implementation and automation, a median filter [23] is applied to eradicate the high frequency impulse noise. The median filter for each individual layer is implemented with the help of formula

$$M_F = \{ I_{T_{n\,jk}} \mid j \in \{1,2,...,W\} \ \ and \ \ k \in \{1,2,...,H\} \}, \tag{5}$$

where M_F is a median filter of size $W \times H$ for a neighborhood of pixels centered at $I_{T_n}(x, y)$. The median element of the window M_F is given by

$$I_{F_n}(x, y) = \begin{cases} M_{F_{SORT}}\left[\dfrac{m}{2}\right] & for\ an\ even\ \ m \\ M_{F_{SORT}}\left[\dfrac{m}{2}+1\right] & for\ an\ \ odd\ \ \ m \end{cases}, \tag{6}$$

where $M_{F_{SORT}}[i]$, $i = 1$, m, $m = W \times H$ and I_{F_n} is the resulting graphene layer of interest (with given *n*) after the impulse noise is removed. The median filter analyzes a set number of pixels in a user-defined matrix region to find the median value of the region currently being inspected. After the operation is performed, the filter is shifted to the next user-defined matrix region until the entire image is analyzed. We tuned our matrix size to effectively eliminate noise while maintaining the high resolution for the identified graphene regions (with given *n*) on the order of a few nanometers.

3.4 RESOLVED ISSUES AND PROOF OF CONCEPT

Initially, our automated identification procedure was somewhat successful yet not very accurate. After much experimentation, we discovered two major problematic errors by adjusting the range of light intensity for red, green, and blue (RGB) shown best by the visual representation of non-uniform illumination in the top panel of Figure 3.10. These problematic errors include: a non-uniform confocal light intensity distribution across the entire image and the second error being static impulse noise across the entire surface of the image. In the bottom panel of Figure 3.11, we display our attempt at graphene layer identification of individual FLG regions without filtering of a 50X optical image. This resulted in pseudo-colors resembling "spray paint" –like features strewn across the intended identified regions supposedly indicating specified graphene layers. For a 12.5µm radius within the center of peak light intensity in the bottom panel of Figure 3.11, graphene layer identification could be accomplished. Although, within these regions there appeared severe cases of impulse noise making identified FLG graphene regions "patchy". These patchy regions will become even more problematic when attempting to provide a quality layering analysis apparatus for industrial applications and would likely cause our method not to pass industrial quality control standards. Outside the 12.5µm radius center of peak light intensity in the bottom panel of Figure 3.11, our graphene layer identification technique incorrectly identifies darker regions as SLG, BLG, etc. without the integration of the non-uniform light elimination filter. These darker regions rapidly reduce their light intensity as they reach the farthest extents of the Gaussian light distribution curve away from the center of peak light intensity within the image. Now that

filter correction has been proven to be important, we have resolved our problematic concerns by providing two beneficial filters within the procedure of our technique. These filters include and are not limited to the following: lense modulation transfer function (L_{MTF}) filter [22] to eradicate non-uniform light illumination, providing uniform light intensity across the substrate. The second filter incorporated is the median filter [23] to smooth out the area of identified regions and eliminate extremely small identified regions of FLG that are insignificant.

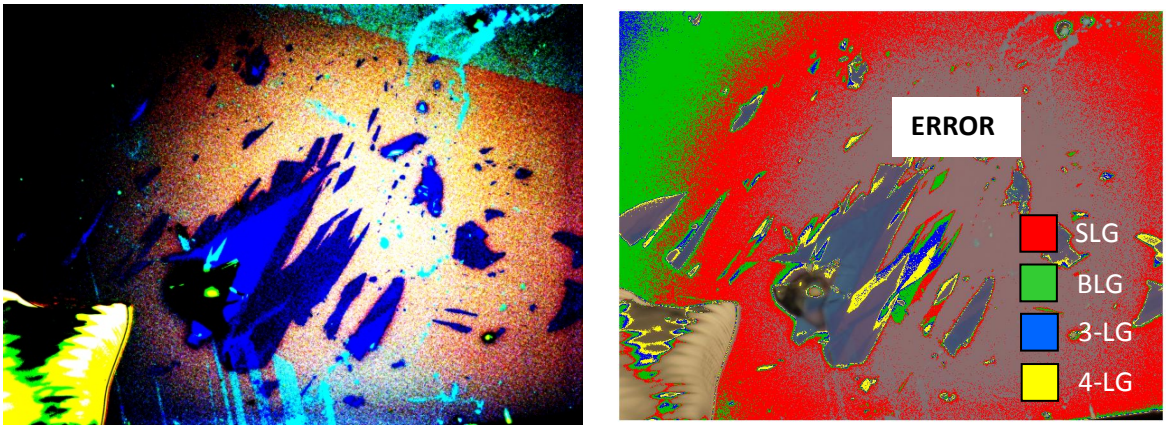

Figure 3.11: 50X optical microscopy image of exfoliated graphene on top of 300nm Si/SiO_2 substrate (left panel) is shown displaying a clear representation of the non-uniform light intensity caused by the confocal lense objective. The same image in the left panel is attempted for graphene layer identification (right panel) without any filtering resulting in numerous errors. (Reprinted with permission from C. M. Nolen et al., ACS Nano **5**, 914 (2011). Copyright (2011) American Chemical Society.)

One of two motivations for this work was to supply a research tool for the scientific community that targets, locates, and identifies specific thickness dependent graphene layered regions. In addition, we wanted to provide a universal technique which could be applied to graphene layers on any substrate that exhibited similar optical refraction properties providing discrete contrast between layers [6]. We also wanted to

expand this technique for use with other atomically-thin materials such as Bi_2Te_3 family of materials which have topological intrinsic properties [9, 10]. It is also possible to expand this to the following material systems: any other materials consisting of thin films or chemical vapor deposition (CVD), etc. that show optically transparent properties as c-axis thinning of the material goes from 3-dimensional (3D) down to 2-dimensions (2D).

Our apparatus for research application is robust and can be completed for an innumerable amount of wafers after calibration parameters have been set. The surface of an entire wafer can analyzed for potential graphene layers within a short amount of time depending on the wafer size. The process for the user becomes relatively simple and is completed only by the following two steps. Step 1) Capture an image of wafer with potential graphene layers. Step 2) Click a button on a software program or software "plug-in" that indicates the user's desire to inspect the captured image for graphene layers. Next, the result appears as in the bottom left panel of Figure 3.12. This simple process can be repeated an innumerable amount of times for any number of wafers that exhibits the same identifiable material on the top of the same type and thickness of substrate at the same light source brightness.

"Blind" verification of our technique is important to show the accuracy and viability of our technique. In Figure 3.12, we show the process of how our apparatus functions after initial calibration, with the exception of including the filtering process which was completed but not shown. Verification of our technique is conducted through "blind" identification of a random sample with potential FLG on top 300nm of Si/SiO_2

after our system has been calibrated. First, an optical image with potential graphene layers is captured by an optical microscope in Step 1) (top left panel). Then this image is analyzed by our automated layer identification technique shown briefly in Steps 2), 3), and 4) and the result is given in a within a few seconds. Step 2) restricts each R, G, B color range to the light intensity range that only corresponds to FLG, meanwhile the rest of the image is "background subtracted" and labeled with the color white. Step 3) Converts the RGB colors to grayscale, and then restricts FLG regions further to isolate SLG regions and BLG regions as a 'mask' where the black regions are labeled with a unique pseudo-color and white regions are transparent. In Step 4), the mask in Step 3) is overlaid on top of the original image in Step 1) resulting in clear visual identification of SLG regions and BLG regions. Filters were conducted as well, yet not shown in this figure due to simplification. The non-uniform light elimination filter was conducted between Steps 1) and 2) and the noise reduction median filter was conducted as the last process in step 4. Our automated identification technique has now been completed. To check the accuracy of our technique, we conducted Raman Spectroscopy on numerous spots that our technique identified as SLG regions and BLG regions and found ~100% verification with an example measurement shown in the bottom right panel.

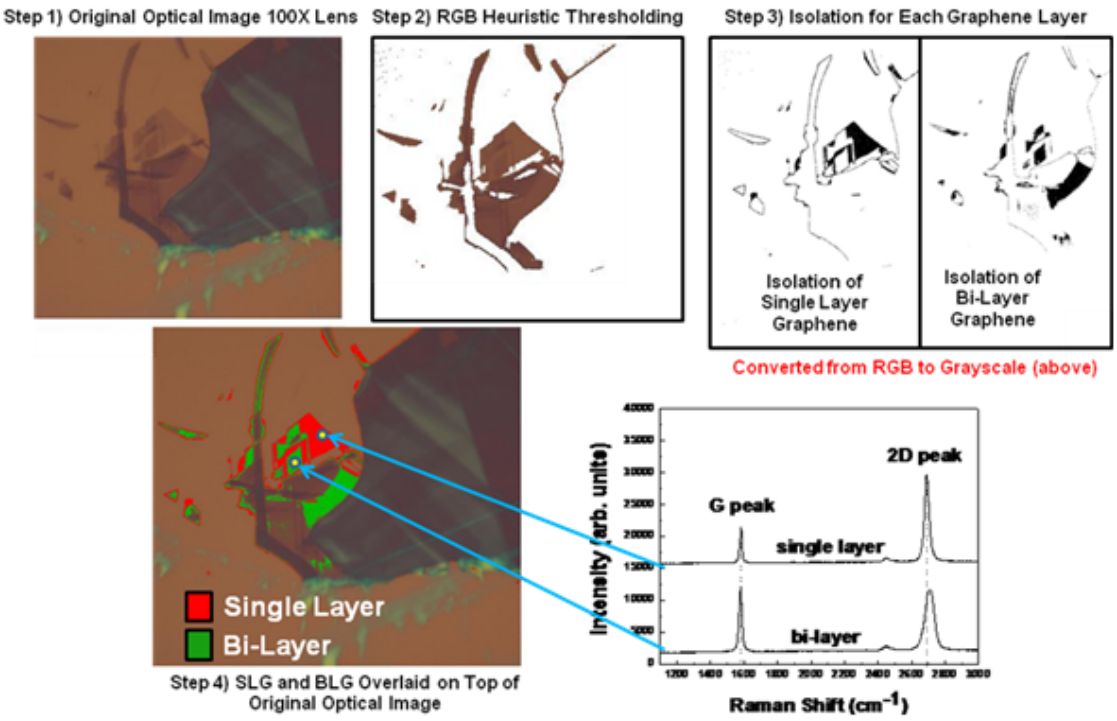

Figure 3.12: The "blind" identification process of validation conducted post calibration is outlined in four steps and then verified by Raman Spectroscopy. In Step 1) an optical microscopy image of a substrate with potential graphene layers is captured with a 100X objective. In Step 2) "background subtraction" is conducted to restrict the range of red, green, and blue colors to only FLG regions. In Step 3) the remaining optical image with only FLG regions is converted from RGB to grayscale and a mask is created by isolating the grayscale intensity range for SLG and BLG, each which are labeled and assigned with a unique pseudo-color, in this case red for SLG and green for BLG. Then in Step 4), this mask is overlaid on top of the original optical image in Step 1) to provide a clear visual representation of the location of SLG and BLG regions. Lastly, in the bottom right panel Raman Spectroscopy is conducted to provide robust verification of the identified SLG and BLG regions. (Reprinted with permission from C. M. Nolen et al., ACS Nano **5**, 914 (2011). Copyright (2011) American Chemical Society.)

3.5 LAYER IDENTIFICATION OF CVD GROWN GRAPHENE ON NI

Thus far, our graphene layer identification process was strictly limited to graphene and FLG produced by adhesive tape transfer by mechanical exfoliation from HOPG onto a 300nm of SiO_2 / Si substrate that makes use of standard constructive optical interference patterns [3]. Since the current state-of-the-art is growing graphene via CVD on top of metal substrate, extending this metrology technique for identifying graphene layers for this medium would significantly increase the value of this tool. More specifically, the development of a layering inspection process for graphene grown over an entire wafer-sized area before further device fabrication processing would enable a new quality control measure for atomically-thin layered grown materials after CVD growth.

A few notable changes in the graphene layer identification process differ from mechanically exfoliated graphene layer identification to CVD grown graphene on Ni. The first of these differences include a change in constructive optical interference (visibility of graphene layers against their substrate medium). Previously for mechanically exfoliated graphene, each layer was clearly visible to the naked eye when viewed under an optical microscope due to large contrast differences between each graphene layer and the substrate that they are placed upon. More specifically, constructive optical interference patterns produce this visible contrast due to the interaction between graphene and the specific thickness of 300nm SiO_2 resting on top of Si which is opaque allowing one to distinguish between one atom-thick planes. For thermal CVD graphene grown on 300nm of Ni, visual recognition of individual graphene layering differs depending on the contrast that each layer exhibits between one another. The second of these differences

include a slight change in the Raman spectrum of graphene where a slight intensifying of the 2700cm^{-1} 2D-peak is seen due to varied graphene layer stacking, yet still remains as a reliable method for counting the number of atomic planes [24]. The following paragraphs give a background and investigation, detailed process methodology, resulting figures, and discuss the increased capabilities that this work offers detailing the importance and industrial motivations for conducting graphene layer identification for detection analysis of grown graphene layers atop their growth mediums.

3.5.1. Background and Investigation

Recently, the focus of graphene research has shifted towards efforts to grow consistent same-layered monolayer graphene (1ML) over wafer-sized areas via chemical vapor deposition (CVD) on metals; Ni [25], Cu [26] and both 1ML or hydrogen intercalated Bernal stacked bi-layer graphene (2ML) via molecular beam epitaxy (MBE) on Si-face 4H-SiC (0001) [27,28], 1ML on Ru (0001) [29], 1ML on Pt(111) [30], and 1ML on Ir(111) [31,32]. More recently, the primary set-back of graphene growth was transferring grown graphene from a metal to a dielectric insulating substrate without damaging [33] or contaminating the grown graphene sheets with residues [34]. This was until recent advancements of a demonstrated technique for growing graphene directly on any dielectric insulator by growing CVD graphene on deposited high-purity Cu, where the Cu was initially deposited directly onto various target dielectric substrates, followed by evaporation of the Cu at high temperature allowing for high-quality graphene to be transferred to a wide variety of dielectric substrates [35]. Although efforts to grow

graphene controllably over various sizable areas have been largely successful [36], the ability to grow predominantly same layered graphene remains a challenge.

As commercialization of graphene nears with recent production of ink-jet printing machines being developed [37], the importance of growing a predominantly synonymous graphene layer across the entirety of its growth medium becomes increasingly important. This high-quality uniform graphene layer becomes paramount for actualizing high-yield, reliable, and reproducible arrays of graphene-based devices. Unfortunately, these said graphene-based devices are sensitive to fluctuation in layering within their working device areas. Direct examples of this problem include; thermal applications and electronic device applications. Thermal graphene-based device applications are affected when graphene is used as a passive lateral heat spreader where thermal boundary resistance (TBR) is largely affected due to phonon scattering as layering consistency is broken inducing Umpklapp scattering [38] causing heat build-up due to a vast change in room temperature (RT) intrinsic thermal properties; 1ML is ~3500W/mK [39] and 2ML is ~1500W/mK [40,41]. Electronic graphene-based device applications such as high-frequency 100 GHz graphene transistors [42] to THz graphene photo detectors [43] are also largely affected by the inconsistency of graphene layering due to the sensitivity of carrier scattering from a large change in RT intrinsic mobility between 1ML ~ 40,000 to 400,000 $cm^2V^{-1}s^{-1}$ [44] and 2ML ~ 3,000 to 8,000 $cm^2V^{-1}s^{-1}$ [45] with 1/f noise [46, 47] being directly affected as well.

High-throughput graphene layer identification for large-area application was initially developed by our research team [48] and then utilized for a number of scalable

inspection processes to provide quality layering control for graphene-based applications [49-51]. These include; thickness determination via gold deposition [49], layer detection process within fabricating suspended structures [50], and grown graphene on Cu transferred to glass for wafer-sized areas [51] having major optoelectronic application potential as a transparent material for solar cells [52], light emitting diode (LED) [53] and organic (OLED) [54] applications. Meanwhile, other graphene identification techniques exist to assess the number of graphene layers or quality of graphene in respect to the purity and presence of lattice defects, but limitation of being slow, expensive, and non-automated hinder their potential use for future industrial applications [48]. To date, no graphene layer identification process has been developed for identifying graphene layers directly on its growth medium before transfer.

Here we report a scalable method for graphene layer identification directly on its growth medium through image processing algorithms which are capable of integration as an automated wafer-scale graphene layer inspection process using the MATLAB image processing toolbox add-on. Our process incorporates a step-by-step procedure following [48] additional post-processing steps to provide statistical interpretation of the identified masked results. As a proof of concept demonstration, we assigned regions of optical microscopic images of ~100µm x 100µm areas to corresponding micro-Raman spectroscopic characterization. Then we performed additional post-processing on the binary output masks detected (shown in Fig. 3.15) using various statistical analysis which we thought would provide pertinent statistical information for improving critical graphene growth parameters and also aid in the development of potential integrated

industrial-scale graphene layer inspection processes. In short, we set out to develop a graphene layer detection process for specifically graphene grown directly on their growth mediums to improve graphene growth, potentially enabling growth of entirely uniform high-quality graphene sheets across wafer-sized areas.

This technique relies on initial calibration of our image processing algorithms in accordance to the Raman spectrum of graphite/graphene to both; identify the unique 'fingerprint' vibrational modes of graphite (G-peak at 1580cm^{-1} (primarily in-plane mode contributions), 2D-peak at 2700cm^{-1} (both in-plane and out-of-plane contributions), defect contribution [55-57] D-peak at 1350cm^{-1}, and count the number of atomic graphene planes by analyzing the ratio of the G-peak to 2D-peak vibrational modes [58]. This ratio is dependent upon two main factors; the substrate that it lays atop of due to interaction and deposition method of graphene by CVD growth or epitaxial MBE growth or mechanically exfoliated from initial HOPG ingot. Traditionally the Raman spectrum for mechanically exfoliated graphene on top of 300 nm of SiO_2/Si has a G-peak to 2D-peak ratio of ~1:4 for λ=488nm and ~1:2 for λ=633nm laser wavelength for single-layer graphene (SLG), ~1:1 G-peak to 2D-peak ratio regardless of laser wavelength for bi-layer graphene (BLG), a slightly higher G-peak than 2D-peak ratio without a visible shoulder on the 2D-peak contribution for (~3-7) few-layered graphene (FLG), and a significantly higher G-peak than 2D-peak ratio with a visible shoulder on the 2D-peak contribution becoming closer to that of bulk graphite comprising of multiple stacked layers (7+) of graphene [58]. Although Raman nanometrology may become less efficient for counting the number graphene layers on CVD grown graphene as compared to mechanically

exfoliated, it is still entirely possible to use the Raman spectrum to count the number of layers [41]. An explanation of this can be understood by observing the increased π- π* bond stacking sequence, where the 2D-peak becomes intensified slightly due to the increased out-of-plane mode interactions as to the G-peak remains unaltered due to having only in-plane interactions. As for counting the number of graphene layers for CVD grown graphene on Ni with Raman spectroscopy, studies have shown that this is entirely possible taking into account the increased 2D-peak intensification [59].

3.5.2 Methodology of Layer Detection

Our procedure follows a step-by-step process to assign, classify, and statistically analyze identified graphene layers. Step 1: generally it is necessary to first model constructive optical interference patterns to find a correct thickness for our growth medium whereby a large contrast between the grown graphene and the substrate is seen. Although when growing graphene on top of a metal, which is usually highly reflective, no modeling needs to be done as each layer of graphene absorbs 2.3% of light and is directly reflected back with no transmission. A more in depth explanation corresponding to step 1 section. Step 2: grow graphene layers via CVD on a specific thickness, purity, and crystallographic orientation which promotes uniform same layer graphene growth. Note there also is 10nm of Pt deposited serving as an adhesion layer all atop a thick Si substrate. Detailed CVD graphene growth on Ni process explained in corresponding step 2 section. Step 3: capture images of grown graphene from an optical microscope in conjunction with using micro-Raman spectroscopy to verify that high-quality graphene

growth was not only grown, but also to ensure that type of graphene that was grown is within one of the most challenging scenarios for graphene layer identification where most of the wafer-sized area contains predominantly varied regions of 1ML, 2ML and few-layered graphene (FLG). Step 4: perform illumination equalization by subtracting the illumination intensity of two optical microscopy images where an image of only the background Ni substrate (without graphene growth) is subtracted from an image of the actual experiment graphene grown on Ni using image processing. Detailed illumination equalization correction process explanation in corresponding step 4 section. Step 5: calibrate image processing algorithms by assigning graphene layered regions and borders of regions verified by micro-Raman spectroscopy. Then classify these regions with unique pseudo-colors with the number of graphene layers that they correspond to. Detailed graphene layer assignment process using image processing explained in corresponding step 5 section. Step 6: median filtering via image processing on each identified graphene layer masks was used to remove salt and pepper charged-coupled device (CCD) noise to improve graphene layer detection accuracy. Detailed median filter processing using image processing explained in corresponding step 5 section. At this point statistical analysis information can now be extracted from identified graphene layer regions by completing additional post-processing by modifying various previously defined image processing algorithms. Step 7: detection of cluster areas, quantification of same layered graphene growth clusters, and perimeter contour detection classified for each graphene layer binary output mask or generic non-specific classification using image processing over the entire image area is explained in further detail in

corresponding step 7 section. This completes our step-by-step graphene growth, layer detection, and post-processing statistical analysis procedure.

Step 1: Optical Constructive Interference for Graphene Grown on Ni

Raw optical visualization of graphene contrasted against the substrate is achieved by using a comparative analysis of constructive optical interference between SiO_2 and Ni. Traditionally individual layers of mechanically exfoliated graphene have been successfully detected under an optical microscope by depositing 300nm of SiO_2 on top of the Si p-doped substrate which is opaque [3]. Similarly for layers of thermal CVD graphene growth a 300nm of Ni was deposited as ~300nm has an index of refraction constant of 1.74 (n) and an extinction coefficient of 1.99 (k) [60]. Also ~10nm of Ti is deposited underneath the Ni layer for adhesion which contains an n value of 0 and k value of 0.0139 for this specific thickness [60]. Although only the n and k values of Ni contribute in total reflection due to the opaque nature that 300nm of Ni resembles where naturally graphene absorbs 2.3% of light illumination [4] for each graphene layer so contrast is directly absorbed with near 100% Ni reflection. This contrast between each graphene layer allows our graphene layer detection technique to determine the number atomic planes of graphene against the substrate after Raman spectroscopy calibration.

Step 2 and Step 3: Graphene Growth on Ni via thermal CVD

The processed substrate consisted of a 4-inch p-doped silicon substrate with the following layers of material atop; 300nm of SiO_2 was created due to thermal oxidation, 10 nm of Ti

was deposited via sputtering as the adhesion layer, and then 300 nm Ni were deposited via e-beam evaporation method as the catalyst for the growth of graphene. A commercial, large-area thermal/PECVD system from Atomate Inc, CA installed in the clean room at Center for Nanoscale Materials at Argonne National Laboratory was used for the Graphene growth. Above mentioned wafer was loaded into the quartz tube (diameter 5 inch) and then transferred into the system for the growth. The base pressure in the growth furnace was evacuated down to 10^{-2} and then purged with Ar for a few minutes. The Ar gas flowed into the growth chamber with flow rate 2000 sccm and the chamber pressure was raised to 300 Torr, followed by increasing the furnace temperature up to 1000 ^{o}C. The process including the temperature ramp to reach 1000 ^{o}C took about 15 minutes and later we kept all conditions same for additional 5 minutes. We call this step as annealing and this helps to get rid of any contaminants on the Ni surface as well as causes grain growth of Ni. After this step, the chamber pressure was lowered down to 100 Torr and Ethanol vapors were introduced into the growth chamber to initiate graphene growth. Ethanol vapors were introduced using Ar as a carrier gas which was bubbled through an Ethanol containing canister. The temperature of the Ethanol containing canister was maintained at 5^{o}C and the outlet of the Ethanol canister was connected to the mass flow meter to regulate the flow of ethanol vapors and it was set at 500 sccm. No hydrogen was used during the growth process. The growth of graphene was carried out for 3 mins. After the growth, all gases were switched off along with switching off the heater simultaneously and the chamber was evacuated down to 10^{-2} Torr while maintaining constant pressure for a few minutes. In order to accelerate cooling down, Ar and H_2 gases

were introduced with a flow rate of 500 sccm respectively raising the chamber pressure to 1 Torr. The cooling rate ranged from 30^{o}C/min at the beginning to 10-15 ^{o}C/min at the later stage. The sample was removed from the growth chamber after cool down and subjected to optical and Raman spectroscopy for further characterization.

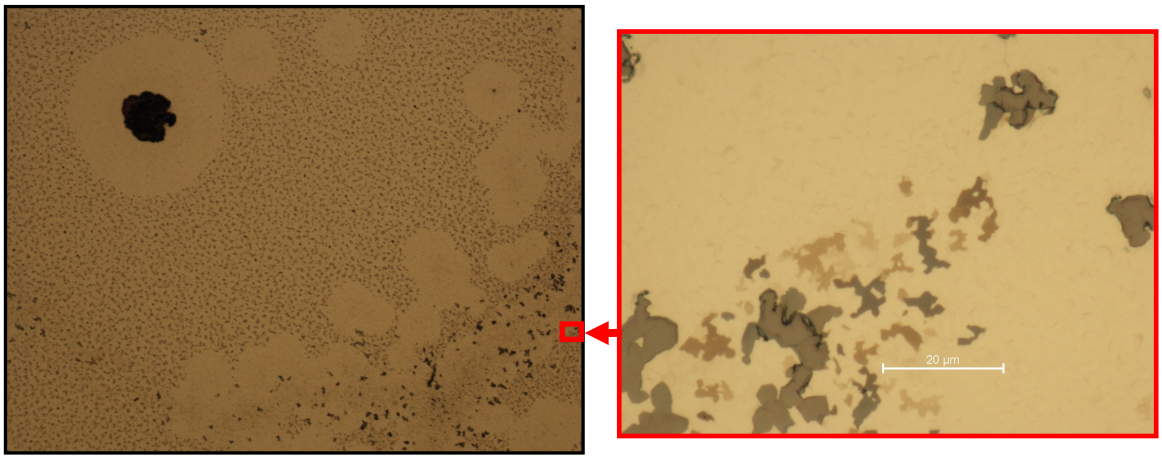

Figure 3.13: (Left panel) Optical microscopy image of CVD graphene layers grown on Ni taken at 50X. (Right panel) Red box inset of a preprocessed optical microscopy image captured at 1000X used for graphene layer detection.

Step 4: Illumination Non-uniformity Correction

Our illumination non-uniformity correction procedure follows the methods section outlined in [48]. This correction procedure is necessary because any illumination that is captured by a CCD is initially altered by the confocal lens before it is reflected off the substrate and then captured by the CCD camera. To reverse this confocal lens effect, it is necessary to capture the additional illumination information from an optical microscopy image of only the background substrate (Image A) and use the additional illumination information to subtract this light from a second captured image being the sample of

interest of CVD grown graphene on Ni using image processing pixel-by-pixel. Mathematically, this algorithm is best explained as a lens modulation transfer function (L_{MTF}) filter [61] used for both x and y planes outlined in equation (1) where the L_{MTF}

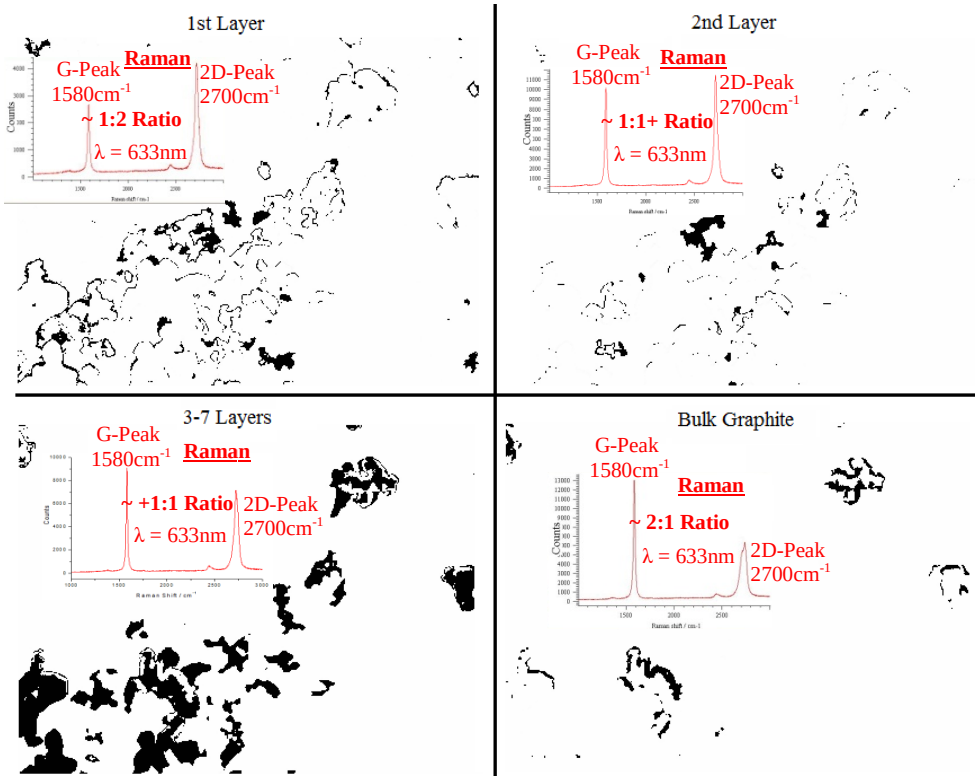

Figure 3.14: Binary output mask of detected CVD grown graphene layers on Ni corresponding to four quadrants according to layering verified by Raman spectras; 1st (top left panel), 2nd (top right panel), 3-7 layers (bottom left panel), bulk graphite (bottom right panel).

extracts the additional illumination from background Image A by subtracting the minimum red, green, and blue (RGB) values from the entire image from every pixel of the image to store the additional illumination information. Then the L_{MTF} equation (1) is subtracted from Image B of the CVD grown graphene layers on Ni in equation (2) for every color of red, green, and blue (RGB).

$$L_{MTF} = I^{A}{}_{C\in R,G,B}(x,y) - min\left(I^{A}{}_{C\in R,G,B}\right) \quad (1)$$

$$I^{B}{}_{n,C\in R,G,B}(x,y) = I^{B}{}_{C\in R,G,B}(x,y) - L_{MTF} \quad (2)$$

where I^A is illumination intensity for Image A, I^B is illumination intensity for Image B, n is the number of graphene layers, C is color, R is red, G is green, B is blue, and L_{MTF} is lens modulation transfer function as previously defined. After application of this filter algorithm procedure, the non-uniform light from the confocal lens aberration is removed.

Step 5: CVD Grown Graphene Layer Detection and Classification

Our CVD grown graphene layer detection and classification largely followed [48]. We carried out this graphene layer detection process by the following 4-step process using image processing. Step 5.1: define a strict range for the three RGB values corresponding to the identified graphene layer range (1 to 7+ bulk graphite number of stacked layers) from prior Raman spectroscopy results. Step 5.2: convert Image B from 3 RGB values per pixel to 1 grayscale value per pixel to simplify mask defining completed in the next step mathematically represented in equation (3) where $I_{n,gry}$ is the illumination intensity values of 'n' number of graphene layers as a scalar grayscale value for each pixel and $I_{n,R \text{ or } G \text{ or } B}$ are the red, green, or blue illumination intensity values of 'n' number of graphene layers for each pixel which are extracted in percentages to complete the conversion of an RGB vector to a singular scalar grayscale value within the range of values between 0 and 255.

$$I_{n,gry} = 0.30I_{n,R} + 0.59I_{n,G} + 0.11I_{n,B} \quad (3)$$

Step 5.3: create individual graphene layer masks of their individual layered regions and borders of regions by assigning the precise pixel range for each graphene layer or range of multiple graphene layers of the x and y planes of Image B to corresponding Raman spectroscopy signatures which encapsulate not only the unique carbon graphite photon-phonon vibrational signature, but also their layer stacking information of the number of atomic planes from the G-peak to 2D-peak ratio [55-57] shown in Figure 3.14. Step 5.4: classify these individual graphene layer or multiple graphene layer range masks by assigning them with unique pseudo-colors for clear visual representation shown in Figure 3.15. Then rewrite these values over the top of Image B outlined mathematically in equation (4) where ΔI_n is the graphene layer illumination intensity range, L is graphene layer, SLG is single layer graphene, BLG is bi-layer graphene, FLG is few-layer graphene (n=3-7 layers), and BULK is bulk graphite (n=8+ layers). Optional Step 5: use the identified binary output masks for each graphene layer or layers to divide over the entire area of Image B to extract basic statistical information deducing the percent CVD graphene growth coverage area over a specific image area of interest. A bar graph contained as an inset within Figure 3.15. shows the graphene layer area percentage for each identified graphene layer or layers over the entire image area of interest (Image B). We used equation (4) in graphene layer classification

$$\sum \Delta I_n(x,y) = \begin{cases} 1, SLG & L1_{min} \le \Delta I_1(x,y) \le L1_{max} \\ 2, BLG & L2_{min} \le \Delta I_2(x,y) \le L2_{max} \\ 3-7, FLG & L37_{min} \le \Delta I_{37}(x,y) \le L37_{max} \\ 8+, Bulk & L8+_{min} \le \Delta I_{8+}(x,y) \le L8+_{max} \\ 0 & other \end{cases} \quad (4)$$

where $\sum \Delta I_n$ is the summation of light intensity ranges for FLG regions containing each of the grouped layers and ΔI_n is the light intensity range for a specific graphene layer of interest. The minimum values span the light intensity threshold range for each graphene layer for a given n.

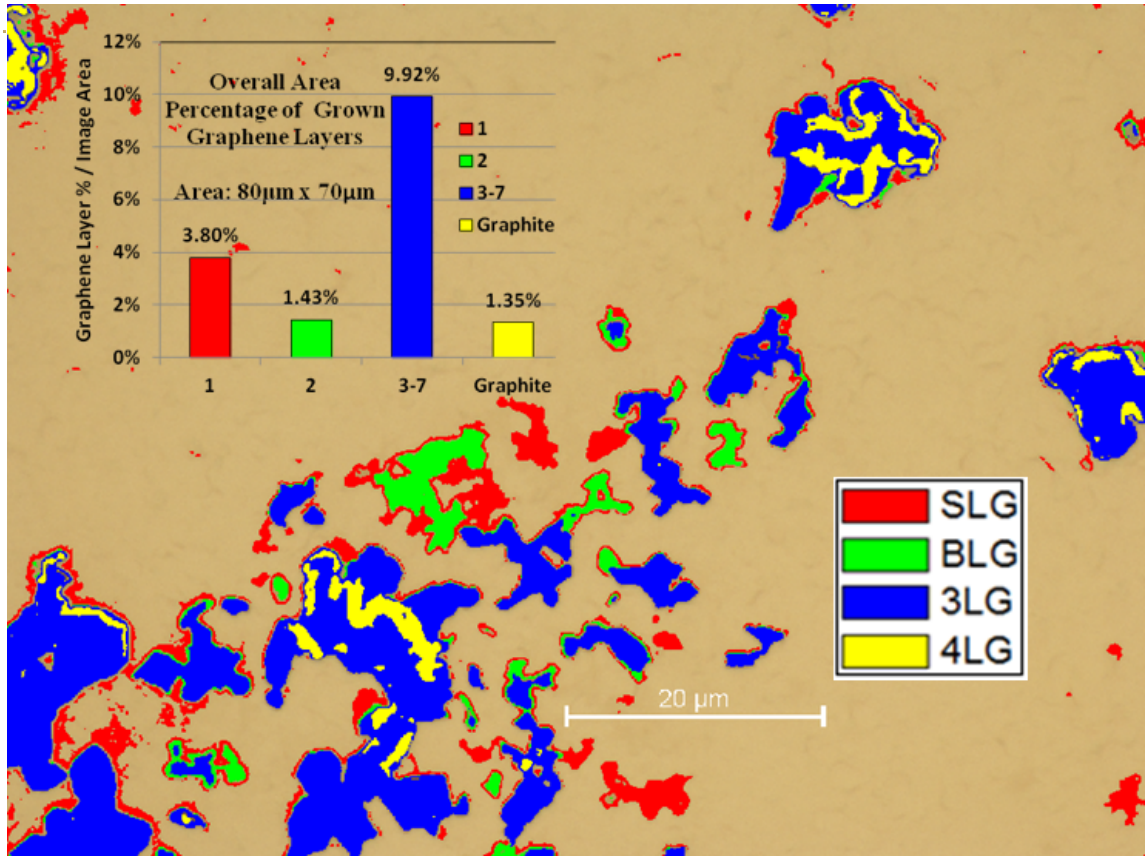

Figure 3.15: Post processed graphene layer detection of Image B by individual unique pseudo-color masks overwritten on top of the original image of CVD grown graphene on Ni shown in the right panel of Fig 3.15. Inset graph shows percentage of each graphene layer over entire 70µm x 80µm image area.

Step 6: Median Filter Correction

The median filter algorithm largely followed [48]. This filter was intended to remove high-frequency impulse noise produced by the CCD device to provide 'smoothing' for more accurate graphene layer detection by only allowing detected pixels to stay if their cluster size is large enough [62]. This is completed by analyzing the center pixel of a defined matrix, sorting the analyzed numbers, then returning the median value. To perform this function in mathematical terms, we define a median filter matrix of W x H size shown in equation (5) where M_F is median filter and $I_{T_{n_{jk}}}$ is defined neighborhood of pixels centered at I_{T_n} located at j, k of a window size of W x H.

$$M_F\left\{I_{T_{n_{jk}}}|j \in \{1,2,\dots,W\}\ and\ k \in \{1,2,\dots,H\}|\right\} \tag{5}$$

Next we pad the border of Image B with 0's in order to properly analyze the edge of the image since the analyzed pixel is always the center pixel so there must be outside defined values when processing any edge pixel. Next we apply equation (6) which sorts the defined matrix and selects the median pixel where $M_{F_{SORT}}[i]$, i = 1, m, m = W x H, and I_{F_n} is the n graphene layer of interest the defined matrix to be sorted.

$$I_{F_n}(x,y) = \begin{cases} M_{F_{SORT}}\left[\frac{m}{2}\right]\ for\ an\ even\ m \\ M_{F_{SORT}}\left[\frac{m}{2}+1\right]\ for\ an\ odd\ m \end{cases} \tag{6}$$

Furthermore, the defined median filter size was tuned for the highest ratio of removing CCD high-frequency impulse noise to highest percentage yield for an identified n graphene layer.

Step 7: Cluster Area Detection, Quantification, and Perimeter Contour Detection

Our algorithm largely followed the sequential region labeling section for binary images in chapter 2 of [63]. Essentially we used an algorithm to perform additional image processing analysis to detect and quantify individual cluster areas of connected neighboring pixels within Image B. To perform this function in mathematical terms, we define a cluster area matrix of W x H size shown in equation (7) where C_A is cluster area and $I_{T_{n_{jk}}}$ is defined neighborhood of pixels centered at I_{T_n} located at j, k of a window size of W x H.

$$C_A\left\{I_{T_{n_{jk}}}|j \in \{1,2,\dots,W\}\ and\ k \in \{1,2,\dots,H\}|\right\} \quad (7)$$

Next we pad the border of Image B with 0's in order to properly analyze the edge of the image since the analyzed pixel is always the center pixel so there must be outside defined values when processing any edge pixel. Next inspect the current pixel and select either to do nothing if a background pixel 0 is detected or if an unlabeled foreground pixel 1 is detected, then the defined matrix extracts generally 8 connected neighbor pixel values plus the centered pixel value from a 3 x 3 C_A matrix. Meanwhile a label assigning algorithm is called (if 1 is detected) to determine the output on a case by case basis where $C_A[i]$, $i = 1$, m, m = W x H, and $I_{S_n}(x, y)$ is the pixel currently being inspected for n graphene layer. Then this label assigning algorithm calls a case A, B, C, or D depending on the values contained inside matrix C_A. Case A is called when no present labeled pixels are extracted from matrix C_A (only returning values 0 or 1) where a new label is assigned

starting from 2 (increased n+1 for every new label) and outputted. Case B is called when only one labeled pixel is extracted from matrix C_A (returning one >1 value meanwhile all other values are 0 and 1) where this previously labeled pixel is propagated with the same label and outputted. Case C is called when more than one labeled pixels are extracted from matrix C_A (returning multiple >1 values) where the lowest numbered labeled pixel is propagated with the same label as the lowest number pixel and outputted. Meanwhile a collision algorithm is called which records the locations and values of these two pixels. Finally, case D is called after all pixels within the image are inspected where the collision algorithm analyzing each pair of collided pixels by comparing each labeled pixel values and choosing the lowest labeled pixel lowest value. Then this collision algorithm takes all identical labeled pixel values that equal the higher value labeled pixel value in this specific collision comparison and replaces these pixel values with the lower labeled pixel value analyzed in this specific collision. Next each cluster area is quantified and given unique pseudo-colors for each individual cluster area (shown in Figure 3.16).

To provide detection of the perimeter contour of these cluster areas, an additional perimeter contour label algorithm can be implemented after sequential region labeling. This algorithm records the location and pixel label value for a sequence progression of two pixels where a background pixel 0 is detected before or after a labeled region >1. Then this labeled pixel value is outputted as a first pass over Image B with either a; unique pseudo-color of the each individual recorded labeled pixel value for every individual cluster area, unique pseudo-color of all recorded labeled pixel values of cluster

areas corresponding to each graphene layer binary output mask (shown in Figure 3.17), or generic white pixel value for cluster areas.

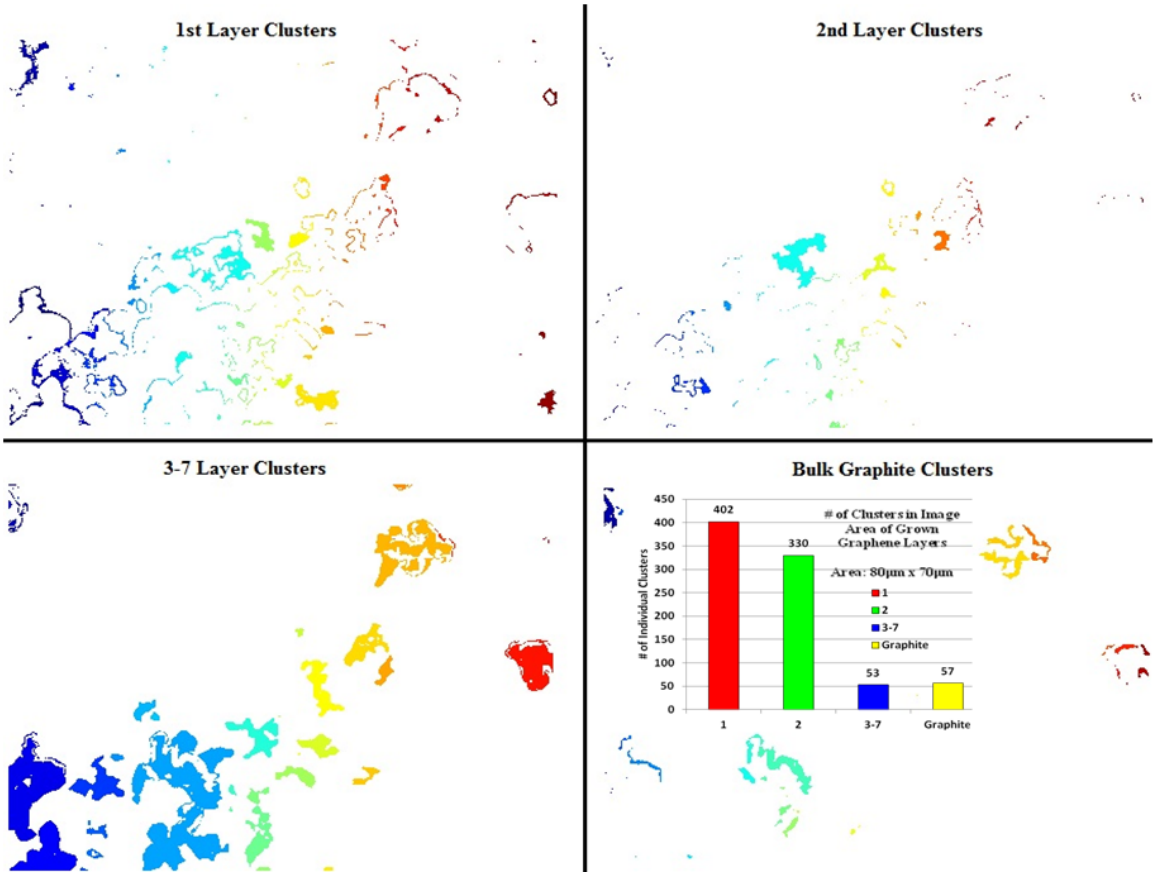

Figure 3.16: Quantification of cluster 'area' formations represented each by different pseudo-colors for each graphene layer corresponding to four quadrants according to their respective layer; 1st (top left panel), 2nd (top right panel), 3-7 layers (bottom left panel), bulk graphite (bottom right panel). Inset graph in the bottom-right panel shows the number of clusters accumulated for different graphene layering over a 80um x 70um area for CVD grown graphene on Ni.

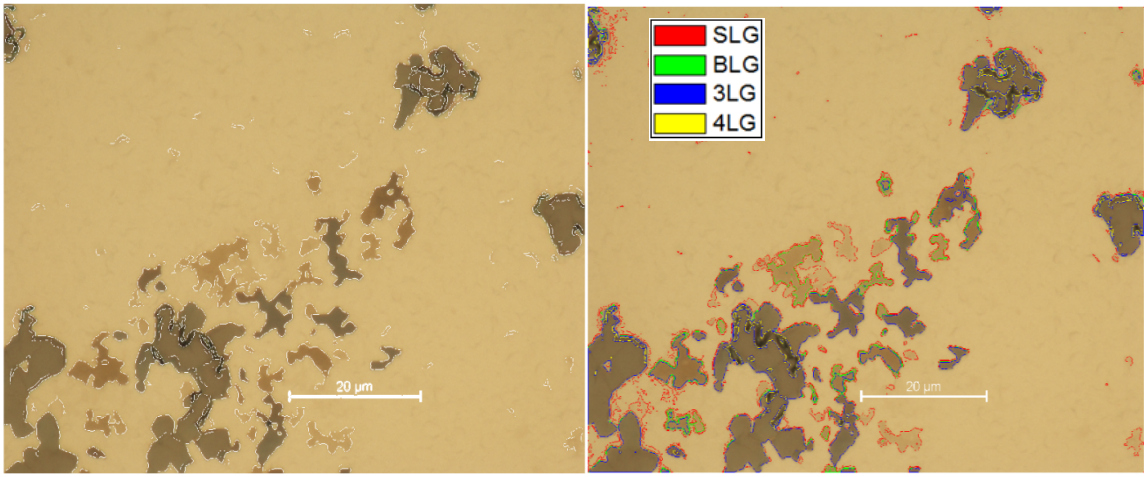

Figure 3.17: (Left panel) Perimeter detection of the right panel in Fig 3.14 for all graphene layer area perimeters outlined in white. (Right panel) Perimeter detection of the right panel in Fig 3.14 classified with unique pseudo-colors pertaining to their assigned layer number. Using these perimeters one may be able to deduce orientation of edges.

3.5.3 CVD Graphene Layer Detection Results

Scalable CVD Grown Graphene Layer Identification

Modeling optical constructive interference patterns provided us with the ability to visually see the CVD grown graphene layers on top of the Ni substrate due to a clear visual contrast difference enabling one to distinguish easily between each stacked additional layer as compared to the substrate providing us with the capability to define precise individual graphene layer ranges coinciding directly with Raman spectroscopy data. We selected 300nm of Ni because this thickness represented reasonable optical constructive interference when compared with Blake et al. [4]. It is important to note that we made sure to also factor in the 10nm Ti adhesion layer along with the Si initial substrate into our equation (1) to accurately reproduce near actual optical constructive interference patterns to increase contrast for various photon wavelengths and Ni

thicknesses. This precise substrate thickness determination was fundamental in giving us the capability to define and calibrate our image processing algorithms to specified illumination intensity pixel value ranges for a given illumination intensity on Image B.

Once calibrated with Raman spectroscopy, our process of graphene layer detection largely followed the procedure of our prior publication in Nolen et al. [48] including; non-uniform illumination correction, graphene layer detection and classification from binary output masks for individual graphene layers with Raman spectroscopy verification shown in Figure 3.14, and median filtering to improve detection accuracy by removing CCD noise from detected graphene layer binary output masks. The result of following these procedures is shown in Figure 3.15 where pseudo-color classification for the range of each detected graphene layers overwritten on top of the original optical microscopy image for clear visual identification. At this point there is enough information to proceed with additional post-processing of images to provide a variety of statistical interpretation inspection of individual layering throughout the CVD graphene growth process.

Statistical Analysis of Graphene Layering & Motivations for Implementation into CVD Graphene Growth Process:

Statistical information was gathered by applying additional image processing functions using the areas identified as graphene layer or layers which enabled us to analyze a number of important statistics useful for potential improvement of the overall CVD graphene growth process. The statistical information that we have provided could

potentially allow for more control of graphene layer growth process if our statistical inspection technique was incorporated within each individual growth step for controlling individual rates of each growth process parameter; temperature, pressure, gas chemical concentration, purity of growth medium, etc. Typically SPC inspections are usually incorporated within each step of a material growth process to automatically tweak each growth parameter to achieve the highest non-fluctuating yield of material purity, continuous uniform growth, etc. Moreover, the graphene layer growth process parameters have yet to be refined with SPC to provide exceptional yields for growing graphene layers that contain high-quality, large-area layer uniformity, and to grow or transfer these graphene layers on any medium [35] preserving material quality.

We decided to produce statistical additional image processing results for the three most important and simplistic areas that show major potential to be incorporated into SPC standards for future industrial growth processes of graphene for producing high-quality and uniformly layered graphene across large wafer-sized areas. First of these statistics includes the percentage area coverage over the area of Image B for each graphene layer shown as the inset of Figure 3.15. By knowing the percentage area of growth for each graphene layer over an area of interest, one can assist graphene growth processes to improve individual graphene layer growth as a SPC parameter for achieving larger-area uniform layer growth. Second of the statistics includes the estimation of the perimeter for all graphene layers in left panel of Figure 3.17 and classified perimeters with unique pseudo-colors for different layers of graphene in right panel of Figure 3.17. The perimeter information could very well help edge specific graphene layer growth

processes for growing specifically only zigzag or armchair graphene terminated edges. These GNR edges are important due to the chirality of edge termination in graphene nanoribbons (GNR) characteristically being determined on the crystallographic direction of the ribbon axis [64]. The importance of these edges lies within the electronic band-gap where a vast difference in properties could be influenced between zigzag GNR edges encasing an electronic band gap resembling an overlapping metallic nature versus armchair GNR edges with an electronic bandgap resembling semi-metallic properties more [65]. Third of the statistics includes the estimation of individual graphene growth of same layered area 'clusters' in Figure 3.16 for each graphene layer and then quantified in a bar chart shown as an inset in the bottom-right panel of Figure 3.16. By determining the number of CVD growth areas for each graphene layer, automatic industrial-scale SPC could possibly be able tune growth parameters to create more uniform and better connected graphene layers creating more reliable and more reproducible high-quality graphene layering for incorporation into current materials systems which require wafer-scale materials to be sustainable for high-yield mass manufacturing practical applications. Moreover, we only presented a few of many additional important statistics that can be compiled by processing further using image processing or other information data analysis techniques to extract critical parameter rates for SPC graphene layer growth process diagnostics.

Our technique shows true versatility and can be applied to large-area automation systems, other "graphene-like" exfoliated atomically-thin layered material systems i.e.; Bi_2Se_3 and Bi_2Te_3 [66-69], various graphene growth mechanisms i.e.; MBE and CVD,

and graphene transferred to various substrates as long as there is a way to contrast each graphene layer from one another different from the substrate that it lies on top of. Furthermore, a proof of concept demonstration of our work was completed in Kyle et al. [51], where our prior technique from Nolen et al. [48] was applied for a millimeter-sized area by stitching together a montage of images containing identified and classified graphene layers using our method of filtering, graphene layer classification using MATLAB: Image Processing Toolbox, and verification from Raman spectroscopy analysis. More specifically Kyle et al. applied our technique to CVD graphene grown on Cu transferred to glass making each graphene layer visible by using a UV light source with an optical microscope after depositing PMMA on top of the transferred graphene. Prior work applying image processing to semiconductor wafer inspection [70] has previously shown an immense impact on chip manufacturing to provide wafer screening of material processing reducing costs and improving SPC parameters. This work proposes a technique to improve quality control parameters of CVD graphene growth via graphene layer identification directly on the growth medium and for implementation of automated SPC inspection systems using screening processes encapsulated from our technique. Practical graphene applications in heat spreader interconnects, analog electronics, and optoelectronic devices [71-75] that are sensitive to graphene material quality and graphene layer fluctuation over large-areas might find our inspection technique particularly useful in developing a graphene layer growth technique that achieves their needs especially since quality and reliability of graphene devices are the present focus of graphene research [76].

3.5.4 Summary

This work describes a high-throughput and automatable method for ascertaining the number of graphene layers for CVD grown graphene on Ni substrates. We characterize these CVD grown graphene layers by detecting discrete absorbed contrast differences between individual graphene layers verified by Raman spectroscopy and further analyzing statistically to provide the following detection capabilities; edges, perimeters, percentage of layers, and cluster quantification. Our inspection methodology uses image processing algorithms to expand our previous work using illumination equalization correction [48], color to grayscale image processing [48], median filtering [48], and various statistical analysis (mentioned in the previous sentence) of detected graphene layers all through a pixel-by-pixel process facilitated by computational calculation. Although graphene layer detection provided in this work included only CVD grown graphene on Ni, this technique was intended to be universal for all atomically-thin layered materials whereby constructive optical interference of the said layered material can be achieved in contrast to the substrate that it is grown or deposited on top of [4]. Furthermore, our scalable graphene layer inspection process is capable of being implemented as a tool for both of the following: 1) as a research application to understand graphene growth processes by providing information in turn to tune the graphene growth process parameter rates [10-18] e.g.; pressure, temperature, derivative chemical composition percentages and 2) as a tool for industrial application through integrated as a fast and high-throughput automated inspection process for post-graphene growth while on its original growth medium.

3.6 BISMUTH TELLURIDE FAMILY OF MATERIALS IDENTIFICATION: QUINTUPLE LAYERING

Recently, our Nano-Device Laboratory group reported the first "graphene-like" mechanical exfoliation of quasi two-dimensional (2D) films of compound semiconductors [9, 10]. The fabrication of quasi-2D crystals via mechanical exfoliation was demonstrated with bismuth telluride (Bi_2Te_3), which has layered crystal structure with the five atomic planes – quintuples – bound by Van der Waals forces. By cleaving crystals along the quintuple layers we were able to obtained single quintuples of Bi-Te and few-quintuple films [9, 10]. These mechanically exfoliated films can find applications in thermoelectric devices and topological insulators [9, 10].

More recently we have mechanically exfoliated, characterized, and created electrical devices for tri-layers of $TiTe_2$ [77] which are interesting for exhibiting phase-change properties. Moreover, this section focuses on studies for Sb_2Te_3 which exhibits phase-change properties (with addition of other elements), topological insulating properties, and thermoelectric properties. Initial characterization of properties for this material system is important to understand before we continue into our large-area identification method. First mechanical exfoliation of antimony telluride (Sb_2Te_3) films and analysis of the Raman spectrum was taken and thickness studies for this material were taken of the resulting quasi-2D crystals. Sb_2Te_3 belongs to the group of the transition-metal dichalcogenides, which are utilized as the phase-change materials for information storage devices [78]. This material exhibits rhombohedral symmetry with a layered crystal structure of five hexagonal atomic planes - quintuples - stacked along the

c-axis in the arrangement Te-Sb-Te-Sb-Te bound by weak Te-Te van der Waal bonds featuring large inter-atomic distances of 3.736 Å [79]. Easy separation along this Te-Te c-axis bond made high quality exfoliation possible due to preservation of bonds within the quintuple structure, all of which exhibit strong bonds owing to their short inter-atomic distances. Due to the ability to create extremely small thickness of such atomic quasi-2D crystals, one can achieve strong quantum confinement of charges and very strong spatial confinement of phonons. By tuning the electron and phonon properties of this material, one can increase the thermoelectric figure of merit, ZT, at low temperature. The electrical and magnetic properties can also be modified by changing the thickness of the quasi-2D crystals of Sb_2Te_3.

For the purpose of identification, quality verification, and to complete further characterization we compiled an investigation of this material through micro-Raman spectroscopy. Initially we identified these exfoliated quintuples using optical contrast technique and atomic force microscopy (AFM). Results of these measurements are shown in Figure 3.18 where in (a) Raman spectroscopy allowed us to examine the vibration properties of Sb_2Te_3 to ensure that they abide by the 3 resonant signature peaks shown in a power dependence study taken. We observed a power % Raman spectrum at 25mW, λ=488nm observing the material classification in-plane peaks $A_{1g}^{'}$ at 68 cm^{-1}, $A_{1g}^{''}$ at 163 cm^{-1}, out-of-plane peak $Eg^{''}$ at 121.5 cm^{-1} which showed blue shifting when melting, and an additional out-of-plane peak $A_{2u}^{'''}$ at 139 cm^{-1} which is not usually a Raman active peak appearing as the crystal lattice becomes melted. The purpose was to show the extremely low thermal conductivity of these materials melting at low power. Also in

Figure 3.18 in (b) optical microscopy images were captured showing a purplish colored material appearing much like few layer graphene interestingly enough. This material was then measured in (c) with AFM and (d) was measured on the order of ~8.6nm in thickness which is stacked about 8 quintuples in vertical height.

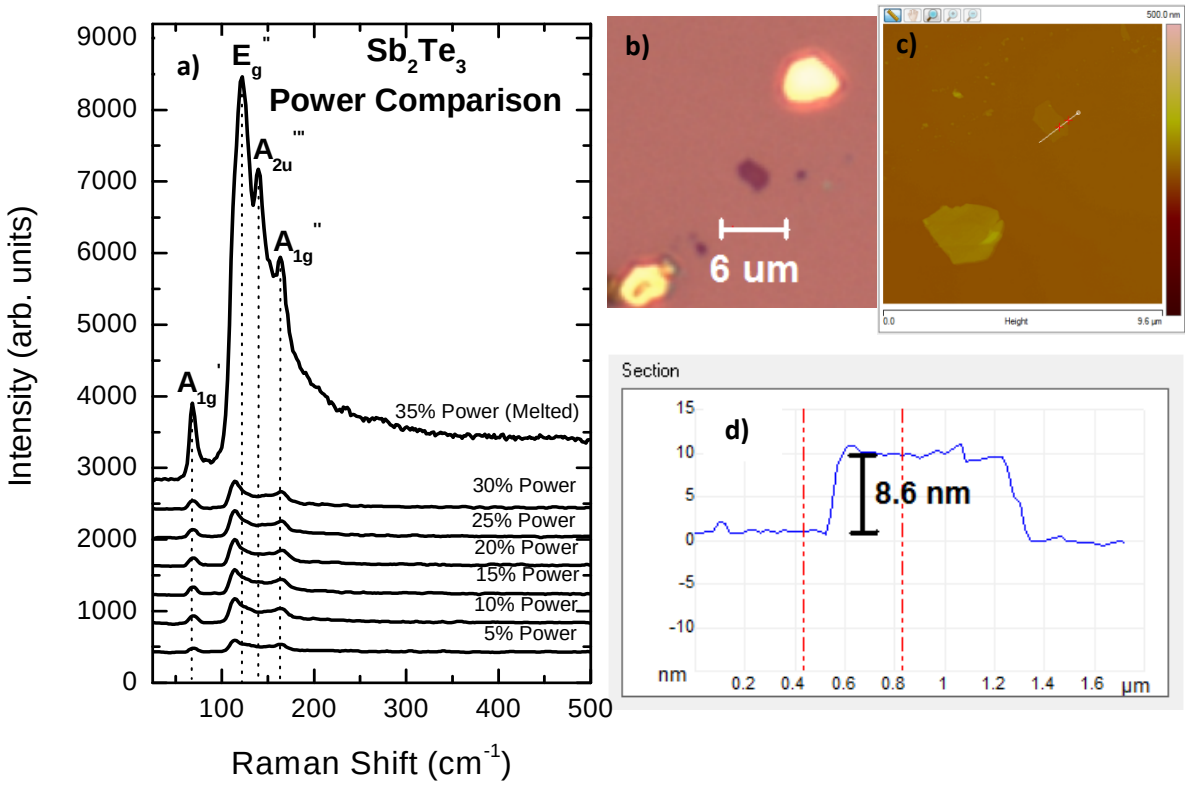

Figure 3.18: Characterization results showing Raman spectrum with power dependence in (a), optical microscopy in (b), and AFM measurement in (c) with thickness measured in (d).

For similar motivations as previously discussed for automated large-area identification of graphene layers and graphene multi-layers, bismuth telluride family of materials including Sb_2Te_3, Bi_2Te_3, and Bi_2Se_3 can benefit from our metrology technique

too. Some of these motivations include; growth process improvement, locating atomically-thin quintuple sheets for research, statistical quality layering control management, and analysis of quintuple layering for wafer-sized areas in industry, etc. We used the same identification process methodology that we used for graphene layer identification for identification of atomically-thin quintuple layers. Since the atomic structure of all bismuth telluride family of materials exhibit similar crystal symmetry (quintuple layering) with similar optical properties, identification for these materials is entirely possible and can be completed similarly. A preliminary result of our identification method working on these quintuple layered systems is shown through analysis of previously published results by Kong et al. [13] of Bi_2Se_3 vapor-solid grown samples down to ~3nm or ~3 quintuples of controlled geometry and ~1nm controlled quintuple growth on top of 300nm SiO_2/Si where the original figure in Kong et al. shows an optical image and AFM image with corresponding height measurement from a line graph. We use image processing analysis on top of the optical image since there is a direct calibration measurement through AFM to compliment the same optical image. Figure 3.19 illustrates the process and results of identification for quintuple layering: in the top left panel the original optical image is displayed, in the top right panel is the final identification of 4 quintuples and 5 quintuples respectively with yellow and blue pseudo colors are mapped back to the original image. For completeness, the 4 quintuple layer mask is shown in the bottom left panel and the 5 quintuple layer mask is shown in the bottom right panel. These masks were found through the same 6 step process

methodology as done previously with graphene layer identification via image processing where the top left panel shows a white box. It is interesting to note that our identification

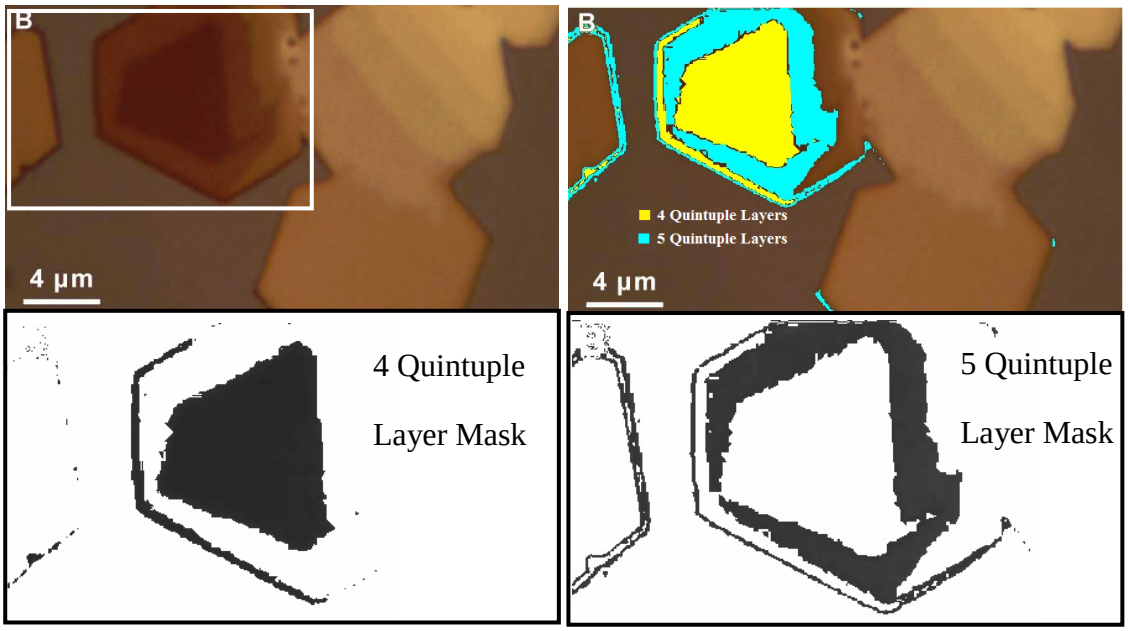

Figure 3.19: Quintuple identification method where the top left panel shows an optical microscopy image from Kong et al. In the top right panel shows the identification of 4 quintuple layers in yellow and 5 quintuple layers in light blue. The bottom left panel and bottom right panel display the masks for 4 and 5 quintuple layering respectively.

method was more accurate in detecting edges than AFM was, although there is much work to be done to increase the accuracy of our technique by refining our process methodology.

3.7 POTENTIAL APPARATUS EXPANSION

Since our apparatus works for graphene layer identification and other atomically-thin layered materials, we plan to utilize our metrology tool to its full extend by expanding this technique for use in many other material science applications. Some of these include,

but are not limited to the following number of expansion possibilities. Identification of graphene on top of near-transparent substrate materials by coating the top of the graphene using a photo resist coating [6] in order to create an constructive optical interference environment which would maximize any contrast difference between each graphene layer and the substrate that it resides on. Furthermore, if the substrate is completely transparent this PMMA coating combined with UV fluorescent spectroscopy has recently been developed using our technique to produce a large contrast difference between graphene layers compared to a transparent substrate such as glass [51]. Expansion of our technique is to calibrate our system with other robust verification techniques such as transmission electron microscopy (TEM), electron dispersion spectroscopy (EDS), low-energy electron microscopy (LEEM), and other analogous material characterization techniques. Another extension of our technique could be to use our technique to develop other metrology systems for other near-transparent thin-film materials already used in the silicon industry for large-scale inspection to tune important material characterization parameters. Specifically, the important materials used in the semiconductor industry that could be most affected might be polysilicon, silicon dioxide, silicon nitride, hafnium oxide, etc. along with the methodology of their deposition steps e.g.; CVD, atomic-layer deposition (ALD), MBE, metal-organic chemical vapor deposition (MOCVD), etc.

3.8 SUMMARY

Demonstration and methodology for layer identification of atomically-thin layered materials using Matlab image processing toolbox calibrated using Raman spectroscopy or

AFM. Layer detection was completed for mechanically exfoliated graphene transferred to SiO_2 substrate, CVD grown graphene on Ni substrate, and vapor-solid grown Bi_2Se_3 on SiO_2 substrates. To ensure our processes and methods were robust in terms of reliability and repeatability, we put our layer detection technique through intensive material characterization tests for graphene layered materials. Our detection technique is compatible for implementation into current automated material inspection systems.

REFERENCES

1. Z. H. Ni, H. M. Wang, J. Kasim, H. M. Fan, T. Yu, Y. H. Wu, Y. P. Feng, and Z. X. Shen, *Nano Lett.* **7**, 9, 2758 (2007).
2. I. Jung, M. Pelton, R. Piner, D. A. Dikin, S. Stankovich, S. Watcharotone, M. Hausner, and R. S. Ruoff, *Nano Lett.* **7**, 3569 (2007).
3. P. Blake, E. W. Hill, A. H. Castro Neto, K. S. Novoselov, D. Jiang, R. Yang, T. J. Booth, and A. K. Geim *Appl. Phys. Lett.* **91**, 063124 (2007).
4. R. R. Nair, P. Blake, A. N. Grigorenko, K. S. Novoselov, T. J. Booth, T. Stauber, N. M. R. Peres, and A. K. Geim, *Science* **320**, 1308 (2008).
5. C. Casiraghi, A. Hartschuh, E. Lidorikis, H. Qian, H. Harutyunyan, T. Gokus, K. S. Novoselov, and A. C. Ferrari *Nano Lett.* **7**, 2711 (2007).
6. G. Teo, H. Wang, Y. Wu, Z. Guo, J. Zhang, Z. Ni, and Z. Shen, *J. Appl. Phys.* **103**, 124302 (2008).
7. I. Calizo, S. Ghosh, W. Bao, F. Miao, C. N. Lau, and A. A. Balandin *Solid State Commun.* **149**, 1132 (2009).

8. I. Calizo, W. Bao, F. Miao, C. N. Lau, and A. A. Balandin *App. Phys. Lett.* **91**, 201904 (2007).
9. D. Teweldebrhan, V. Goyal, and A. A. Balandin, *Nano Lett.* **10**, 1209 (2009).
10. D. Teweldebrhan, V. Goyal, M. Rahman, and A. A. Balandin, *App. Phys. Lett.* **96**, 053107 (2010).
11. K. M. F. Shahil, M. Z. Hossain, D. Teweldebrhan, and A. A. Balandin, *App. Phys. Lett.* **96**, 153103 (2010).
12. M. Z. Hossain, S. L. Rumyantsev, K. M. F. Shahil, M. Shur, and A. A. Balandin, *physica status solidi* (a) **208**, 144 (2010).
13. D. Kong, W. Dang, J. J. Cha, H. Li, S. Meister, H. Peng, Z. Liu, and Y. Cui, *Nano Lett.* **10**, 2245 (2010).
14. W. Dang, H. Peng, H. Li, P. Wang, and Z. Liu, *Nano Lett.* **10**, 2870 (2002).
15. C. Huang, C. F. Wu, and C. C. Wang, *IEEE Trans. Des. Test. Comput.* **19**, 2 (2002).
16. F. Parvizi, *Micro & Nano Lett.* **3**, 29 (2008).
17. S. Amini, J. Garay, G. Liu, A. A. Balandin, and R. Abbaschian, *J. of App. Phys.* **108**, 094321 (2010).
18. S. Subrina, D. Kotchetkov, and A. A. Balandin, *IEEE Electron Device Letters* **30**, 1281 (2009).
19. Q. Shao, G. Liu, D. Teweldebhran, and A. A. Balandin, *App. Phys. Lett.* **92**, 202108 (2008).
20. X. Yang, G. Liu, A. A. Balandin, and K. Mohanram, *ACS Nano* **4**, 5532 (2010).

21. S. Rumyantsev, G. Liu, W. Stillman, M. Shur, and A. A. Balandin, *J. Physics: Condens. Matt.* **22**, 395302 (2010).

22. E. Levy, D. Peles, M. Opher-Lipson, and S. G. Lipson, *Applied Optics* **38**, 679 (1999).

23. R. C. Gonzalez and R. C. Woods, Digital Image Processing 3rd Ed.; Prentice-Hall Inc., Upper Saddle River, NJ, (2006).

24. S. Bae, H. Kim, Y. Lee, X. Xu, J. S. Park, Y. Zheng, J. Balakrishnan, T. Lei, H. R. Kim, Y. Song, Y. J. Kim, K. S. Kim, B. Ozyilmaz, J. H. Ahn, B. H. Hong, and S. Iijima, *Nature Nanotechnology* **5**, 574 (2010).

25. K. S. Kim, Y. Zhao, H. Jang, S. Y. Lee, J. M. Kim, K. S. Kim, J. H. Ahn, P. Kim, J. Y. Choi, and B. H. Hong, Nature **457**, 706 (2009).

26. X. Li, W. Cai, J. An, S. Kim, J. Nah, D. Yang, R. Piner, A. Velamakanni, I. Jung, E. Tutuc, S. K. Banerjee, L. Colombo, and R. S. Ruoff, Science **324**, 1312 (2009).

27. K. V. Emtsev, A. Bostwick, K. Horn, J. Jobst, G. L. Kellogg, L. Ley, J. L. McChesney, T. Ohta, S. A. Reshanov, J. Rohrl, E. Rotenberg, A. K. Schmid, D. Waldmann, H. B. Weber, and T. Seyller, Nature Mater. **8**, 203(2009).

28. K. Lee, S. Kim, M. S. Points, T. E. Beechem, T. Ohta, and E. Tutuc, Nano Lett. **11**, 3624 (2011).

29. P. W. Sutter, J. I. Flege, and E. A. Sutter, Nature Mater. **7**, 406 (2008).

30. P. Sutter, J. T. Sadowski, and E. Sutter, Phys. Rev. B **80**, 245411 (2009).

31. A. T. N'Diaye, S. Bleikamp, P. J. Feibelman, and T. Michely, Phys. Rev. Lett. **101**, 219904(E) (2008).

32. Z. Sun, S. K. Hamalainen, J. Sainio, J. Lahtinen, D. Vanmaekelbergh, and P. Liljeroth, Phys. Rev. B **83**, 081415(R) (2011).
33. W. Regan, N. Alem, B. Aleman, B. Geng, C. Girit, L. Maserati, F. Wang, M. Crommie, and A. A. Zettl, Appl. Phys. Lett. **96**, 113102 (2010).
34. X. Liang, B. A. Sperling, I. Calizo, G. Cheng, C. A. Hacker, Q. Zhang, Y. Obeng, K. Yan, H. Peng, Q. Li, X. Zhu, H. Yuan, A. R. H. Walker, Z. Liu, L. M. Peng, C. A. Richter, ACS Nano **5**, 9144 (2011).
35. A. Ismach, C. Druzgalski, S. Penwell, A. Schwartzberg, M. Zheng, A. Javey, J. Bokor, and Y. Zhang, Nano Lett. **10**, 1542 (2010).
36. Q. Yu, L. A. Jauregui, W. Wu, R. Colby, J. Tian, Z. Su, H. Cao, Z. Liu, D. Pandey, D. Wei, T. F. Chung, P. Peng, N. P. Guisinger, E. A. Stach, J. Bao, S. Pei, and Y. P. Chen, Nature Mater. **10**, 443 (2011).
37. F. Torrisi, T. Hasan, W. Wu, Z. Sun, A. Lombardo, T. Kulmala, G. W. Hshieh, S. J. Jung, F. Bonaccorso, P. J. Paul, D. P. Chu, A. C. Ferrari. arXiv:1111.4970v1 [cond-mat.mtrl-sci] (2011).
38. D. L. Nika, E. P. Pokatilov, A. S. Askerov, and A. A. Balandin, Phys. Rev. B **79**, 155413 (2009).
39. A. A. Balandin, S. Ghosh, W. Bao, I. Calizo, D. Teweldebrhan, F. Miao, C. N. Lau. Nano Lett. **8**, 902 (2008).
40. A. A. Balandin, Nature Mater. **10**, 569 (2011).
41. S. Ghosh, W. Bao, D. L. Nika, S. Subrina, E. P. Pokatilov, C. N. Lau, and A. A. Balandin, Nature Mater. **9**, 555 (2010).

42. Y. M. Lin, C. Dimitrakopoulos, K. A. Jenkins, D. B. Farmer, H. Y. Chiu, A. Grill, and Ph. Avouris, Science **327**,662 (2010).

43. V. Ryzhii, M. Ryzhii, V. Mitin, and T. Otsuji, J. Appl. Phys. **107**, 054512 (2010).

44. S. V. Morozov, K. S. Novoselov, M. I. Katsnelson, F. Schedin, D. C. Elias, J. A. Jaszczak, and A. K. Geim, Phys. Rev. Lett. **100**, 016602 (2008).

45. K. S. Novoselov, A. K. Geim, S. V. Morozov, D. Jiang, Y. Zhang, S. V. Dubonos, I. V. Grigorieva, and A. A. Firsov, Science **306**, 666(2004).

46. G. Liu, W. Stillman, S. L. Rumyantsev, M. Shur, and A. A. Balandin, Intl. J. HS. Elec. Systms. **20**, 161 (2011).

47. S. Rumyantsev, G. Liu, W. Stillman, M. Shur, and A. A. Balandin, J. Phys.: Condens. Matter. **22**, 395302 (2010).

48. C. M. Nolen, G. Denina, D. Teweldebrhan, B, Bhanu, and A. A. Balandin, ACS Nano **5**, 914 (2011).

49. H. Q. Zhou, F. Yu, H. C. Yang, M. J. Chen, G. Wang, and L. F. Sun, Chem. Phys. Lett. **518**, 76 (2011).

50. M. Z. Hossain, and D. Teweldebrhan, J. Nanoelect. and Optoelect. **6**, 116 (2011).

51. J. R. Kyle, A. Guvenc, W. Wang, M. Ghazinejad, J. Lin, S. Guo, C. S. Ozkan, and M. Ozkan, Small **7**, 2599 (2011).

52. X. Wang, L. Zhi, and K. Mullen, Nano Lett. **8**, 323 (2008).

53. G. Jo, M. Choe, C. Y. Cho, J. H. Kim, W. Park, S. Lee, W. K. Hong, T. W. Kim, S. J. Park, B. H. Hong, Y. H. Kahng, and T. Lee, Nanotechnology **21**, 175201 (2010).

54. J. Wu, M. Agrawal, H. A. Becerril, Z. Liu, Y. Chen, and P. Peumans, ACS Nano **4**, 43 (2010).

55. C. Thomsen, and S. Reich, Phys. Rev. Lett. **85**, 5214 (2000).

56. A. C. Ferrari, Solid State Comm. **143**, 47 (2007).

57. D. M. Basko, Phys. Rev. B **76**, 081405(R) (2007).

58. A. C. Ferrari, J. C. Meyer, V. Scardaci, C. Casiraghi, M. Lazzeri, F. Mauri, S. Piscanec, D. Jiang, K. S. Novoselov, S. Roth, A. K. Geim. Phys. Rev. Lett. **97**, 187401 (2006).

59. C. C. Lu, C. Jin, Y. C. Lin, C. H. Huang, K. Suenaga, and P. W. Chiu, Langmuir **27**, 13748 (2011).

60. E. D. Palik, Handbook of Optical Constants, (Academic, Orlando) (1985).

61. E. Levy, D. Peles, O. M. Lipson, and S. G. Lipson, Appl. Opt. **38**, 679 (1999).

62. R. C. Gonzales, and R. Woods, Digital Image Processing 3rd Ed., Saddle River, NJ: Prentice-Hall Inc. (2006).

63. W. Burger, and M. J. Burge, Digital Image Processing: An Algorithmic Introduction Using Java 1st Ed. Springer Street, New York, NY: Springer Science + Business Media, LCC (2008).

64. V. Barone, O. Hod, and G. E. Scuseria, Nano Lett. **6**, 2748 (2006).

65. A. H. Castro Neto, F. Guinea, N. M. R. Peres, K. S. Novoselov, and A. K. Geim, Rev. Mod. Phys. **81**, 109 (2009).

66. D. Teweldebrhan, V. Goyal, and A. A. Balandin, Nano Lett. **10**, 1209 (2010).

67. D. Teweldebrhan, V. Goyal, M. Rahman, and A. A. Balandin, Appl. Phys. Lett. **96**, 053107 (2007).

68. K. Shahil, K. M. F. Hossain, D. Teweldebrhan, and A. A. Balandin, Appl. Phys. Lett. **96**, 153103 (2010).

69. M. Z. Hossain, S. L. Rumyantsev, D. Teweldebrhan, K. M. F. Shahil, M. Shur, and A. A. Balandin, Phys. Status Solidi A **208**, 144 (2010).

70. C. J. Huang, C. F. Wu, and C. C. Wang, IEEE Design & Test of Computers **19**, 44 (2002).

71. S. Subrina, D. Kotchetkov, and A. A. Balandin, IEEE Electron Device Letters **30**, 1281 (2009).

72. Q. Shao, G. Liu, D. Teweldebrhan, and A. A. Balandin, Appl. Phys. Lett. **92**, 202108 (2008).

73. X. Yang, G. Liu, A. A. Balandin, and K. Mohanram, ACS Nano **4**, 5532 (2010).

74. S. Rumyantsev, G. Liu, W. Stillman, M. Shur, and A. A. Balandin. J. Phys.: Condens. Mater. **22**, 395302 (2010).

75. F. Bonaccorso, Z. Sun, T. Hasan, and A. C. Ferrari, Nature Photonics **4**, 622 (2010).

76. X. Liang, B. A. Sperling, I. Calizo, G. Cheng, C. A. Hacker, Q. Zhang, Y. Obeng, K. Yan, H. Peng, Q. Li, X. Zhu, H. Yuan, A. R. H. Walker, Z. Liu, L. M. Peng, C. A. Richter, ACS Nano **5**, 9144(2011).

77. J. Khan, C. M. Nolen, D. Teweldebhrhan, D. Wickramaratne, R. K. Lake, and A. A. Balandin, Appl. Phys. Lett. **100**, 043109 (2012).

78. M. Wuttig and N. Yamada, *Nature Materials* **6**, 824 (2007).

79. T. L. Anderson and H. B. Krause, *Acta Cryst.* **B30**, 1307 (1974).

Chapter 4

Scalable Graphene Transfer Process

4.1 INTRODUCTION

Recent advancements in controlled high-quality uniform layer growth of graphene through chemical vapor deposition (CVD) on Cu [1] or growth by thermal decomposition on SiC [2] over wafer-sized areas has been the current focus of graphene research. Through these developments, the motivation for transferring graphene from its growth medium (usually a metal [3]) to arbitrary dielectrics of choice has rapidly grown in importance. This is in part due to corporate and governmental motivations to seek out the commercial and industrial viability for securing graphene as a material with parallel fabrication capability. Severe limitations exist for transferring large-areas of graphene including processes which chemically degrade graphene or leave residues [4], are not suitable for parallel fabrication [5], are only good for few specific applications [6], can only be used for highly ordered pyrolytic graphite (HOPG) bulk transfer [7], etc. A model of the graphene transfer apparatus is shown in Figure 4.1 with various modification possibilities. This section largely follows details in SAND2011-6961 [8].

Sandia National Laboratories is a multi-program laboratory managed and operated by Sandia Corporation, a wholly owned subsidiary of Lockheed Martin Corporation, for the U.S. Department of Energy's National Nuclear Security Administration under contract DE-AC04-94AL85000.

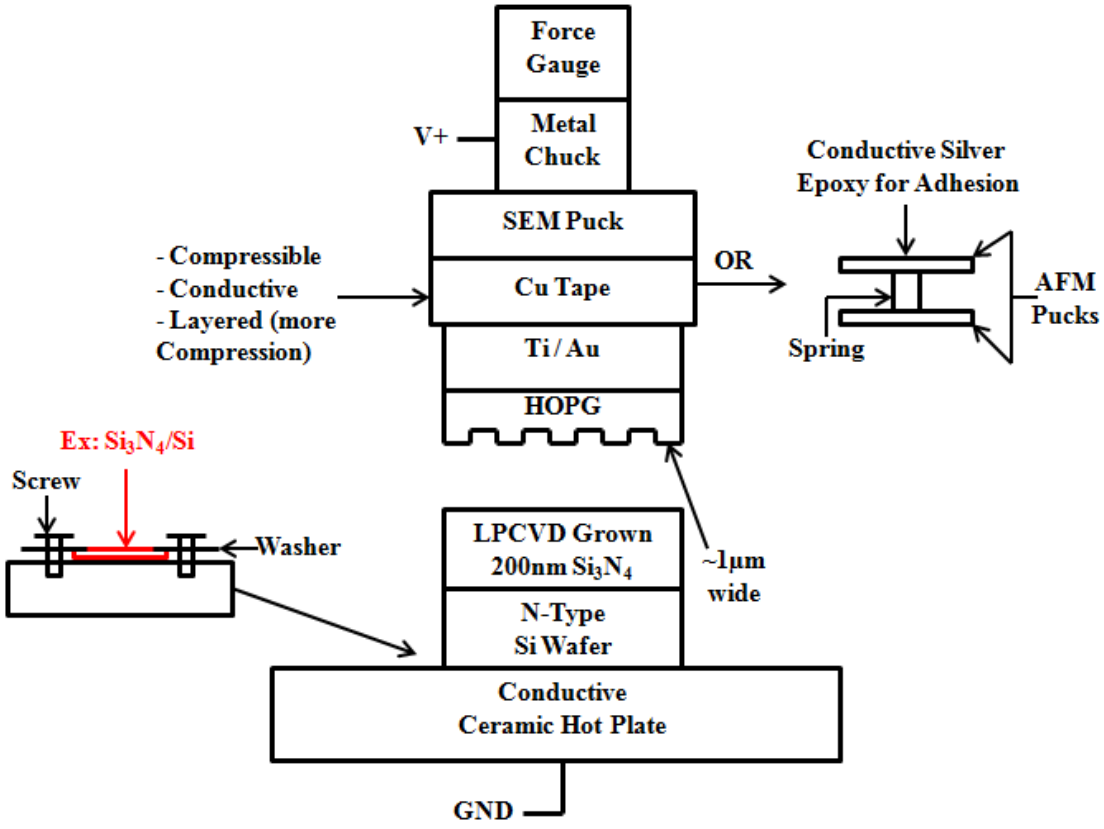

Figure 4.1: Model diagram of the generalized test bed electrostatic transfer apparatus used for transferring graphene to arbitrary substrates with a variety of modification options depending on various donor and acceptor substrates.

4.2 ELECTROSTATIC TRANSFER OF HOPG GRAPHITE PILLARS

Initial work completed at Sandia National Laboratories (SNL) has been to research and develop an electrostatic graphene transfer process. Our goal is to produce a reliable high-quality wafer-scale transfer apparatus that is compatible with future parallel graphene fabrication processes. Our results prove that we have now matched the results of current electrostatic transferring processes [7, 9-10] of transferring HOPG pillars, defined using photolithographic patterning, to common dielectric substrates shown in

Figure 4.2. The target dielectric is 200 nm Si_3N_4, deposited via low pressure chemical vapor deposition (LPCVD), on doped Si. We transferred the HOPG pillars by applying a large compression force >50 N by sandwiching the HOPG pillars with Si_3N_4 using a precision flattened vice. 30 V forward bias was applied to the HOPG, creating a 0.75 MPa electrostatic pressure force on 200 nm Si_3N_4, thus overcoming the 0.4 MPa needed for exfoliation from HOPG [11].

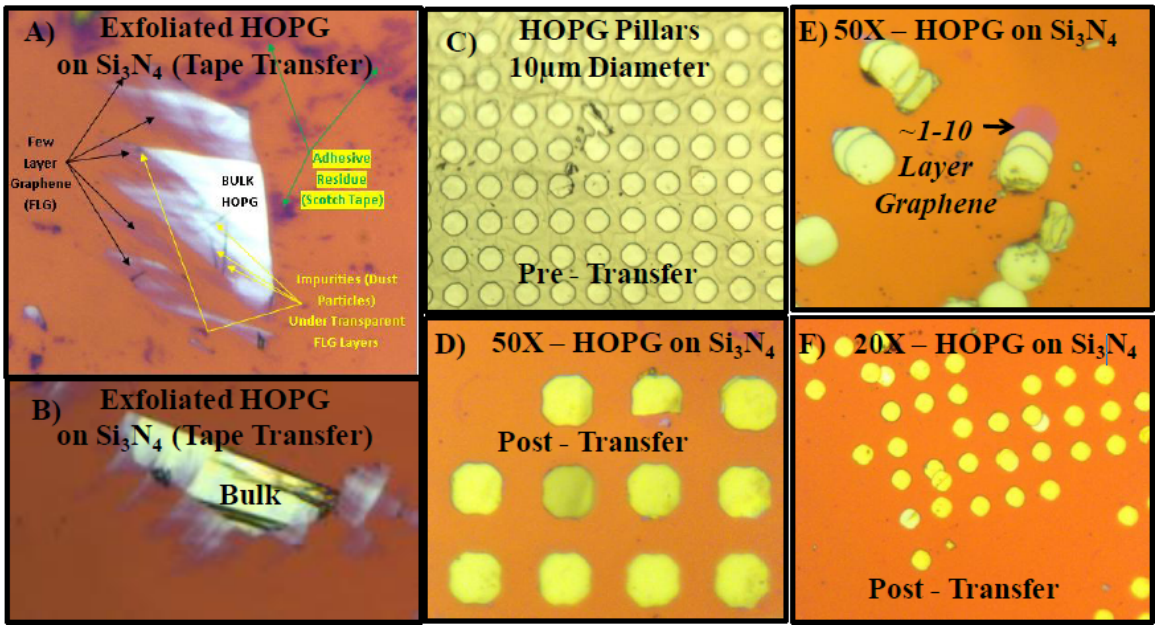

Figure 4.2: Various aspects of graphene transfer are outlined via optical microscopy; A) and B) are thin and bulk exfoliated graphite from HOPG bulk transferred to Si_3N_4, C) shows 10µm HOPG pillars, and D), E), F) are patterned HOPG pillars transferred to Si_3N_4 substrate.

Si_3N_4 was chosen as the choice target substrate since this dielectric material can sustain high voltages before tunneling and can maintain strength under high pressures as compared with other substrates. Reliability test of current-voltage characterization for 200 nm of Si_3N_4 was carried out until a tunneling regime of Poole-Frenkle emission [12,

13] was clearly seen when compared with theoretical calculations shown in Figure 4.3 A) The equation for this plot is labeled by Habermehl et al. in Ref [12]. Next, the electrostatic pressure force vs. voltage was plotted for Si_3N_4 in Figure 4.3 B) showing that a 0.4 MPa electrostatic pressure is great enough to exfoliate HOPG which can be accomplished by applying a bias of >22V. This plot shows that HOPG can be exfoliated between 22V to 80V without venturing into the Poole-Frenkle emission tunneling arena that traps carrier charges. The electrostatic pressure calculation consists of $P=\varepsilon_o\varepsilon_r V^2/2d^2$, where ε_o is dielectric permittivity of free space $8.85x10^{-12}$ F/m, ε_r is dielectric constant 7.5 for Si_3N_4, d is thickness 200nm, and P is pressure in N/m.

Once fully characterized, the experimental apparatus was designed and built. Initially, we experienced problems with little to no exfoliation force. To seek out this problem we utilized a capacitance measurement technique to gauge how much of the HOPG was in contact with the Si_3N_4 (contact area). This measurement revealed that the contact area between the two surfaces was much less than expected (a smaller capacitance). The solution to our problem was to use a precision flat vice to clamp these plates together in excess of >100 N/m. We were then able to achieve the correct capacitance within 5% and results of Figure 4.2 were then achieved in an ambient environment. Our results conclude that our apparatus relatively matches the electrostatic transfer quality of other setups found in literature and is ready to explore new research possibilities. We have yet to control the environmental conditions; therefore improvement to achieve high quality transfer is well in within the scope of this work.

To further control the environmental conditions, we implemented a number of reliability control measures. One being a capacitance to surface area measurement incorporated

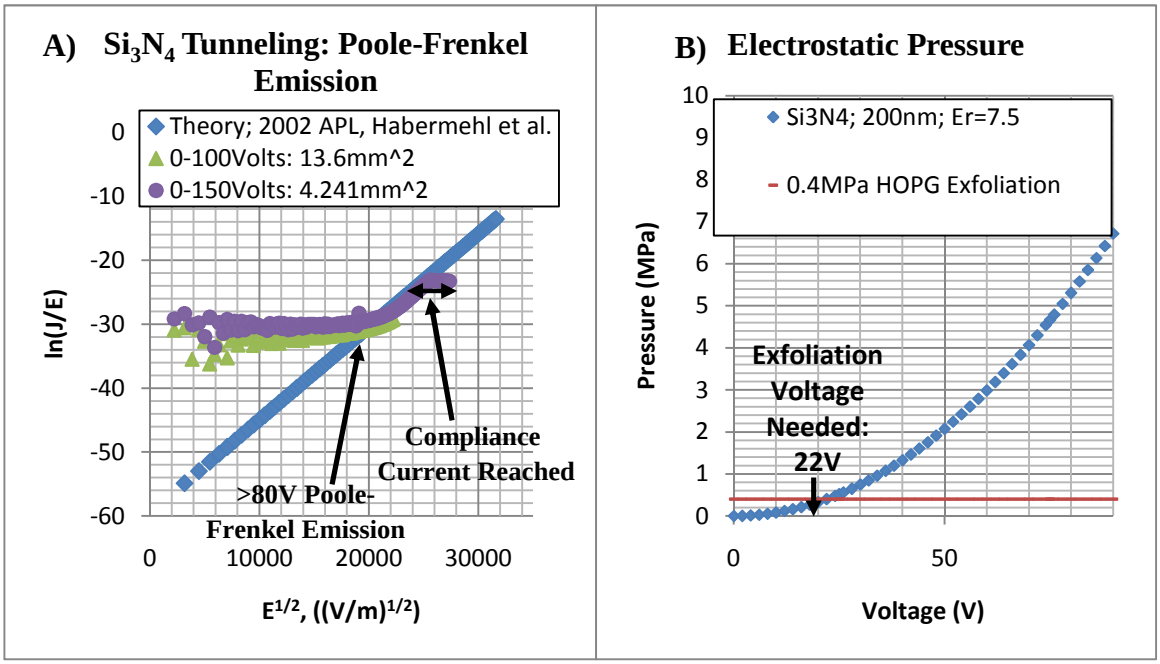

Figure 4.3: Reliability of 200 nm Si_3N_4 as an electrostatic target substrate was carried out in A) where little carrier emission is seen up to 80 V and in B) 22 V was calculated to be the minimum voltage needed to achieve the 0.4 MPa HOPG exfoliation pressure.

into our graphene transfer process as an inspection quality improvement step to increase the yield of transferred graphene by ensuring that we did indeed have complete contact between the surface area of the donor graphene substrate and acceptor target substrate Si_3N_4. For an accurate measurement of capacitance to surface area, our experiments were matched to calculated values displayed graphically in Figure 4.4 using the following formula $C = (\varepsilon_o \varepsilon_r A)/d$. Where C is the capacitance variable under investigation as the y-axis in Figure 4.4 having units in Farads, ε_r is the dielectric constant where we use 7.5 for Si_3N_4, ε_o is constant of relative permittivity in free space being 8.85×10^{-12} F/m, A is the

contacted surface area varied in the x-axis in Figure 4.4, and d is the insulating thickness between conducting surfaces where we use the 200 nm.

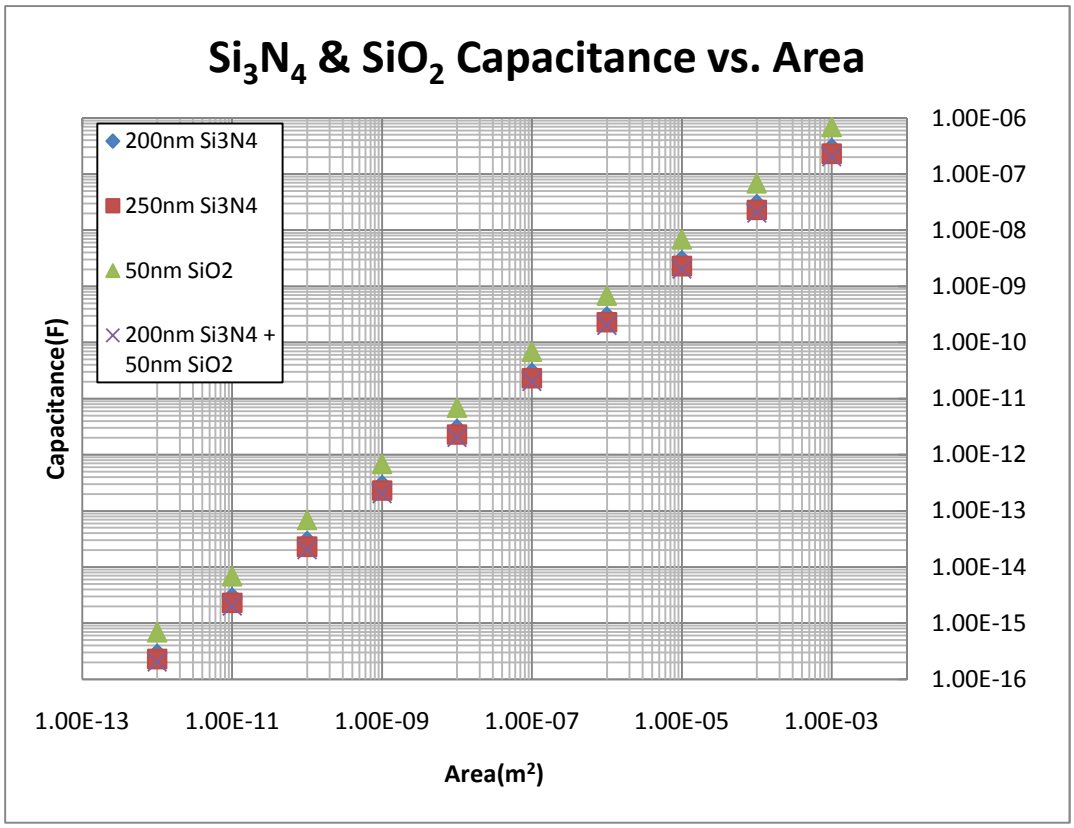

Figure 4.4: Capacitance to area is calculated for various deposited material scenarios for the purpose of including a process inspection to ensure complete contact between surfaces.

Force to area measurement was included as another reliability control measurement incorporated into our graphene transfer process to ensure that the correct electrostatic pressure was physically being applied. To properly execute this measurement, specific gold square geometries were evaporated through electron-beam evaporation onto the top of the acceptor substrate containing a specific area and deposited over the entire area of the Si p-doped backside as a back area contact. This enabled us the

possibility to directly correlate our experimental results with our calculated results which are graphically displayed in Figure 4.5 using the following formula $F = (A\varepsilon_o\varepsilon_r V^2)/(2d^2)$. Where F is force variable under investigation as y-axis in Figure 4.5 in N, A is area varied in the x-axis in Figure 4.5 in units of m^2, ε_o is free space relative permittivity as $8.85x10^{-12}$ F/m, ε_r is the dielectric constant where we use 7.5 for Si_3N_4, V are the various constant voltages with units in V, and d is the insulating thickness between conducting surfaces where we use 200 nm.

Unfortunately when we attempted to match our experimental results with the calculated forces seen, we found that very little electrostatic force was physically measured using our force measurement setup. Although this was not a direct determination that there was not much force being applied between the donor and acceptor, it was definitely a question of concern as to if the electrostatic force was being applied or not. After much discussion and literature search, our investigation yielded inconclusive results and only opened up more questions as to whether Si_3N_4 was an improper substrate to use for electrostatic forces since very little is known in literature about Si_3N_4 electrical characteristics. What is known is that electrostatic force was seen in very small amounts with our test bed using Si_3N_4 as the dielectric, yet still could potentially assist graphene transfer rather than just stamping the pattern for transfer.

Lastly, we achieved success after reevaluating previously published content on successful electrostatic graphene transfer and found a link that they all lacked in providing vital information regarding the amount of pressure that they used in their methodology. As it turns out, an immense amount of pressure is needed in an excess of

>20N needed to transfer graphitic pillars from donor to acceptor substrates using a precision-flat vice with very small roughness in order to provide uniform even high pressure to sandwich these mediums together without cracking, breaking, or damaging

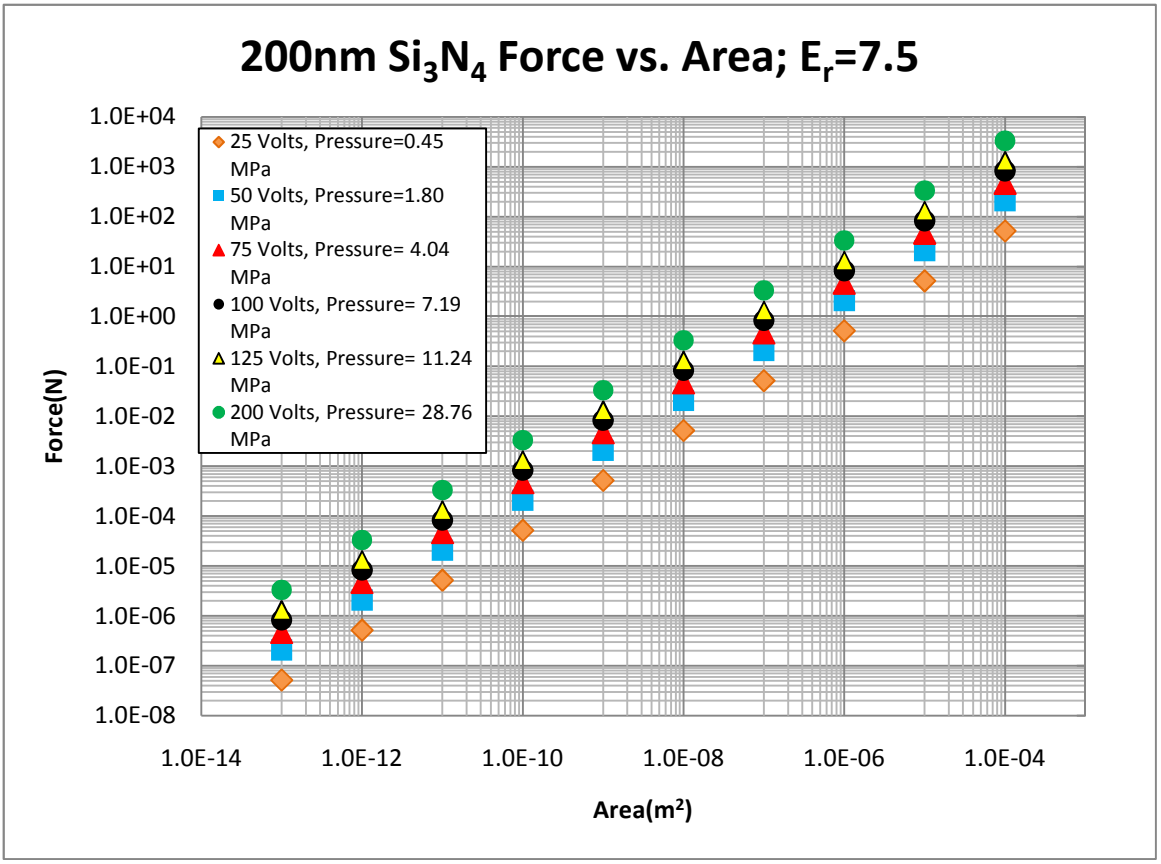

Figure 4.5: Force to area contact area for various voltages used to ensure proper electrostatic pressure force is achieved between donor and acceptor substrate structures.

either side during this clamping process. Numerous results are shown in Figure 4.2 providing conclusive results of graphitic bulk HOPG transfer.

The overall methodology concerning the fabrication of pillared structures and electrostatic graphite transfer process implementation are both detailed in a step-by-step fashion in Figure 4.6 where included are the following steps. In the first step we start out

with smoothing via mechanical exfoliation using scotch tape peeling until a shiny mirror finish is achieved from an initial HOPG SPI-Grade 1, 2, or 3 (depending on grain size and quality of orientation needed) bulk piece with dimensions 5mm x 5mm x 1mm (length x width x thickness) from SPI Supplies. The second step includes numerous other fabrication steps outlined in the next paragraph concerning the fabrication via lithographic patterning of pillars detailed step-by-step in Figure 4.7. In step three, preparation of the acceptor substrate is briefly labeled out where 200 nm of Si_3N_4 is deposited on top of the p-doped Si substrate using low-pressure chemical vapor deposition fabrication (LPCVD). Then the Ti/Au contact is deposited onto the backside surface of the acceptor substrate by first etching any native oxide using Ar^+ ion milling and then thereafter in the same chamber, 10 nm of Ti is deposited followed by ~100 nm Au using electron-beam (E-beam) evaporation as a backside contact. Lastly, in step four the electrostatic graphite transfer process takes place where the HOPG graphite patterned pillars from the donor substrate is pressed together with >20 N of force with a precision flat vice to the acceptor substrate followed by applying >22 V of bias where the backside contact is grounded allowing for potentially > 0.4 MPa of electrostatic force explained in the first few paragraphs of this section. Resulting raw visual results are seen in the last part of Figure 4.6 in the bottom right corner as the HOPG graphite pillars and post transferred graphite on the acceptor substrate are captured with optical microscopy images.

Lithographic patterning fabrication procedure of the following HOPG graphite pillars are outlined within this paragraph for Figure 4.7. First, the HOPG bulk graphite

obtained from SPI Supplies was exfoliated with adhesive tape to obtain a relatively smooth surface backed by using a visual examination to ensure a 'mirror finish'. In step two, SiO_2 is deposited using chemical vapor deposition (CVD) for the purpose of using a

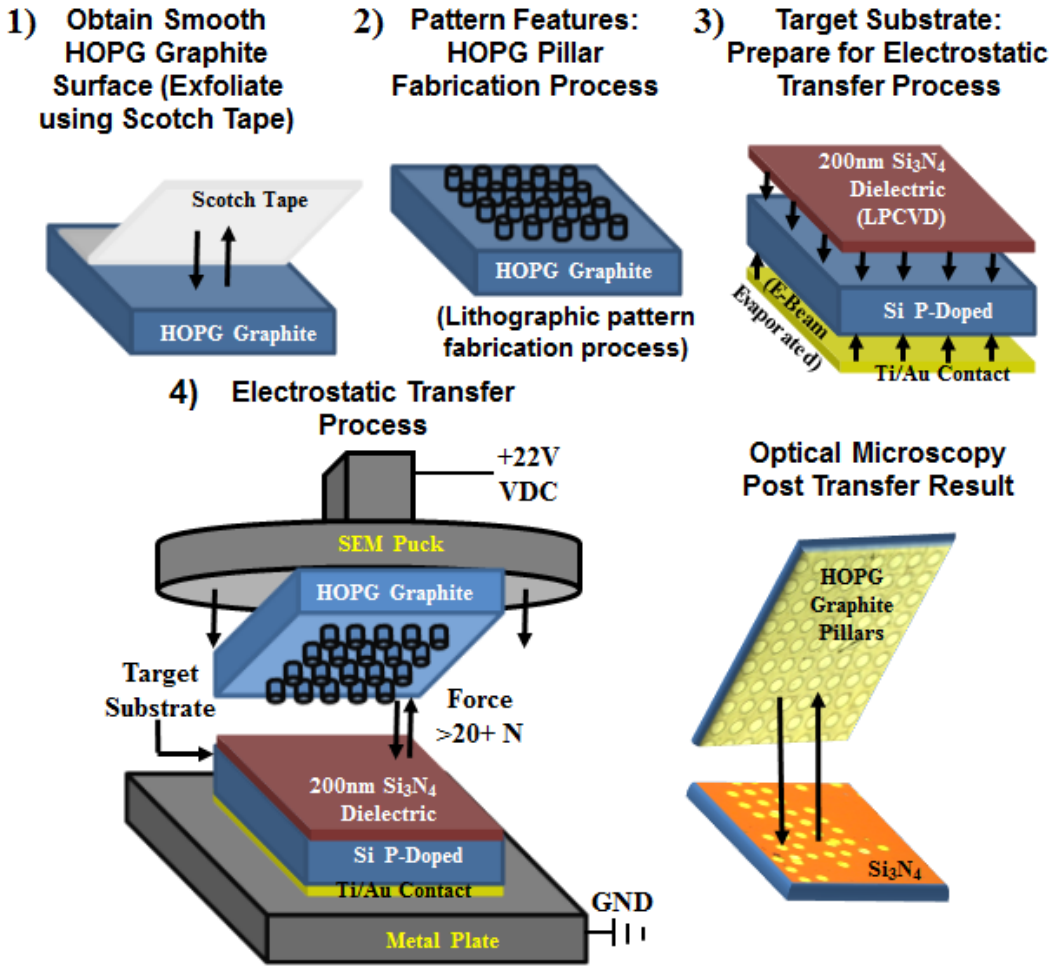

Figure 4.6: Detailed step-by-step model of the overall graphene transfer apparatus implementation including donor and acceptor preparation. Process shows a range from the beginning steps with the overall fabrication process and ending with the complete electrostatic transfer apparatus outlining details of system where each fabricated piece is shown for use in the complete setup. Raw visual optical microscopy results using this setup for post fabrication and post transferred carbon material is shown.

'hard mask' for later etching the HOPG preventing photo-resist (PR) contamination. In step three, a thin layer of hexamethyldisilazane (HDMS) is evaporated to promote adhesion of the PR. In step four, a thin layer of negative PR is spin coated and baked onto the substrate for patterning features in latter steps. In step five, features are patterned using a mask and UV light exposes unmasked parts of the negative PR causing the PR to stay after soaking in the developer solution and washing away any non-exposed features in the photolithography process. In step six, reactive-ion etching (RIE) takes place only inside features where PR does not cover them. RIE Ar^+ ion bombardment and plasma reactions O_2 take place to etch all the way through the deposited SiO_2 to the graphite which is etched by the O_2 plasma a few µm. In step seven, acetone is used to wash way the PR and HDMS organic polymers. In step eight, HF wet etch is used to etch away the SiO_2. Lastly in step nine, the resulting HOPG pillars are remaining where an optical microscopy image and model of the pillared structure express the success of our result.

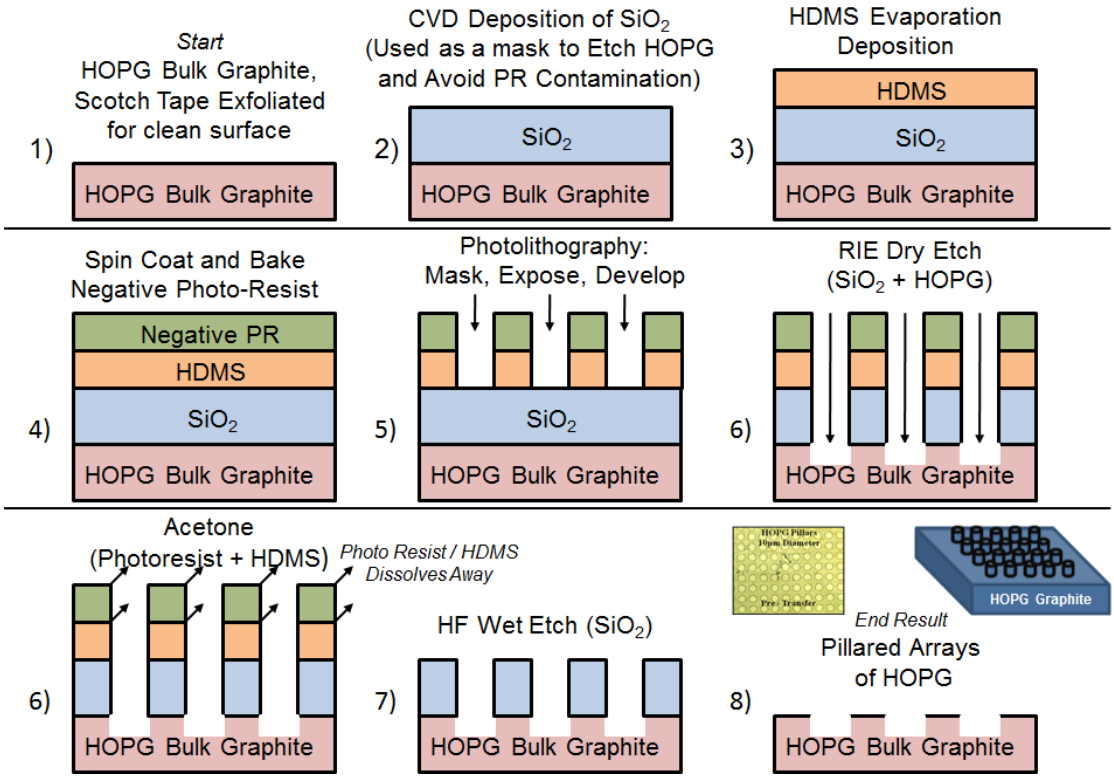

Figure 4.7: Detailed step-by-step model of the lithographic pillar fabrication process methodology used to create the corresponding donor HOPG pillared structure.

4.3 SONICATION THINNING AND CLEANING PROCESS OF HOPG PILLARS

Historically high frequency (1-100 KHz) sonication bathes have been used to dissociate / reduce particles from one another through ultrasonic vibrations which have been largely utilized for ensuring that vacuum parts are particle free when used in an acetone bath. Generally, a higher the frequency produces faster dissociation of particles and more advanced sonication bath instruments auto-tune into the resonant frequency of particles to produce a more efficient / effective dissociation. More specifically sonication has been used in an N-methyl-2-pyrrolidone (NMP) bath as a liquid exfoliation process to turn

graphite into small particles of graphene suspended in solution [14]. NMP is commonly used in cleanroom environments as a universal solvent to dissociate a wide range of chemicals and works especially well at cleaning surfaces of hard to remove adhesive organic polymers or at bare minimum reducing the adhesion 'sticking force' properties of various adhesives e.g; scotch tape. Most recently, NMP has been used as the notable solvent to reduce graphite into small fluid particles enabling the development of an inkjet graphene transfer printing process for application as a few-layer graphene particle spray which can be applied to most all arbitrary substrates and can be used as a flexible transparent conductive electrode for solar-cell and optoelectronic applications for use in cheap thin-film-transistor (TFT) electronics [15].

The origin of graphite and graphene exfoliation rely upon surface energy binding forces between itself, the substrate it lies on, and 'between the sheets' of individual graphene layers where the van der Waals binding force remains the dominant adhesion force pinning graphene and all its layers. Through numerous reports [16-19], this van der Waals binding force for graphite and graphene consists of a surface energy of ~70-80 mJ m^{-2}. In literature, liquid exfoliation is best when the enthalpy of mixing graphite dispersed in good solvents nears zero and the solvent-graphite interaction is predominately interacted with the van der Waals binding force interaction and predicted that the best solvent has a surface tension in the range of 40-50 mJ m^{-2} such as NMP [14]. Furthermore NMP can allow for the delamination of HOPG graphene flakes from the surface of SiO_2 if there is strong adhesion force (being monolayer (1ML) or bilayer graphene (2ML)), yet other liquids in sonication may prove to provide better sonication

to separate graphene layers from one another when stacked in bulk graphite form since it takes less surface energy to dissociate them due to the fact that the topmost stacked graphene layers are not interacting with the substrate surface (if at all) in the same way that only 1ML or 2ML graphene layers are adhered to the surface.

In order to determine a proper sonication solution, we tested isopropanol (IPA), NMP, water, and oil to determine what liquid would best fit to provide exfoliation only to the post-transferred HOPG pillars sitting on the Si_3N_4 substrate. After initially using water as the sonication bath, it was quickly realized that after very short time intervals (<1 minute) complete cleaning of the Si_3N_4 surface would take place and all post-transferred graphite pillars would vanish completely from inspection. After much analysis it was determined that because the surface of Si_3N_4 is very hydrophilic, the interaction between water sonication and the transferred HOPG pillar edges were very high causing these pillars to completely wipe away at +1 minute of sonication or at the very least move to another location on the Si_3N_4 surface after just a few seconds of sonication in water. Since graphene is hydrophobic and does not interact with water [20], these HOPG pillars will interact predominantly with hydrophobic surface tension interaction. Next NMP was selected due to being used in liquid exfoliation explained in the previous paragraphs above. As it turns out for bulk HOPG transferred stacks, NMP caused a very similar result as with the water by sliding or sweeping away these transferred HOPG pillars even at low time / low power sonication. Next IPA was selected from its known reduction in surface stiction role for surface micromachining because it has a much higher surface tension interaction on Si_3N_4 when weighing hydrophobic

surface tension to hydrophilic surface tension ratio than water and other solvents when contacting with Si_3N_4 surface [21]. IPA sonication resulted in a much better outcome which provided a noticeably higher exfoliation (thinning) to shifting / wiping transferred HOPG pillars from the Si_3N_4 surface, yet still did not meet goal for providing only exfoliation of pillars. Lastly, we used very clean oil used for vacuum systems as the bath for sonication due to purely hydrophobic surface tension interaction with little to no hydrophilic surface tension interaction. Results displayed in Figure 4.8 demonstrate a sonication time evolution from 10 to 50 minutes detailing the following observations with colored arrows; low pillar shifting occurs in all colored arrows, black arrow shows that very thinned out HOPG pillars are relatively undisturbed from shifting or degradation, yellow arrow shows cleaning or peeling of non-complete pillared regions, blue arrow shows highly stacked pillars falling and being removed from the surface via exfoliation without any shifting of the bottom-most pillar. Furthermore, from Figure 4.8 one can also see that the sonication began to rid the entire graphene surface of anything on top of it. Through Raman spectroscopic analysis, we found that there was no change to the defect disorder D-peak (1350 cm^{-1}) after sonication of these pillars showing that the entity of graphene throughout its basal plane is extremely strong and holds together through low power sonication when stacked together as an HOPG stack. This allows for the clean stripping exfoliation that we see when examine the yellow arrow in Figure 4.8 with further analysis.

Furthermore in Figure 4.9, demonstration through optical microscopy images show patterned exfoliation and thinning in A) and D). In B) excessive sonication over 4+

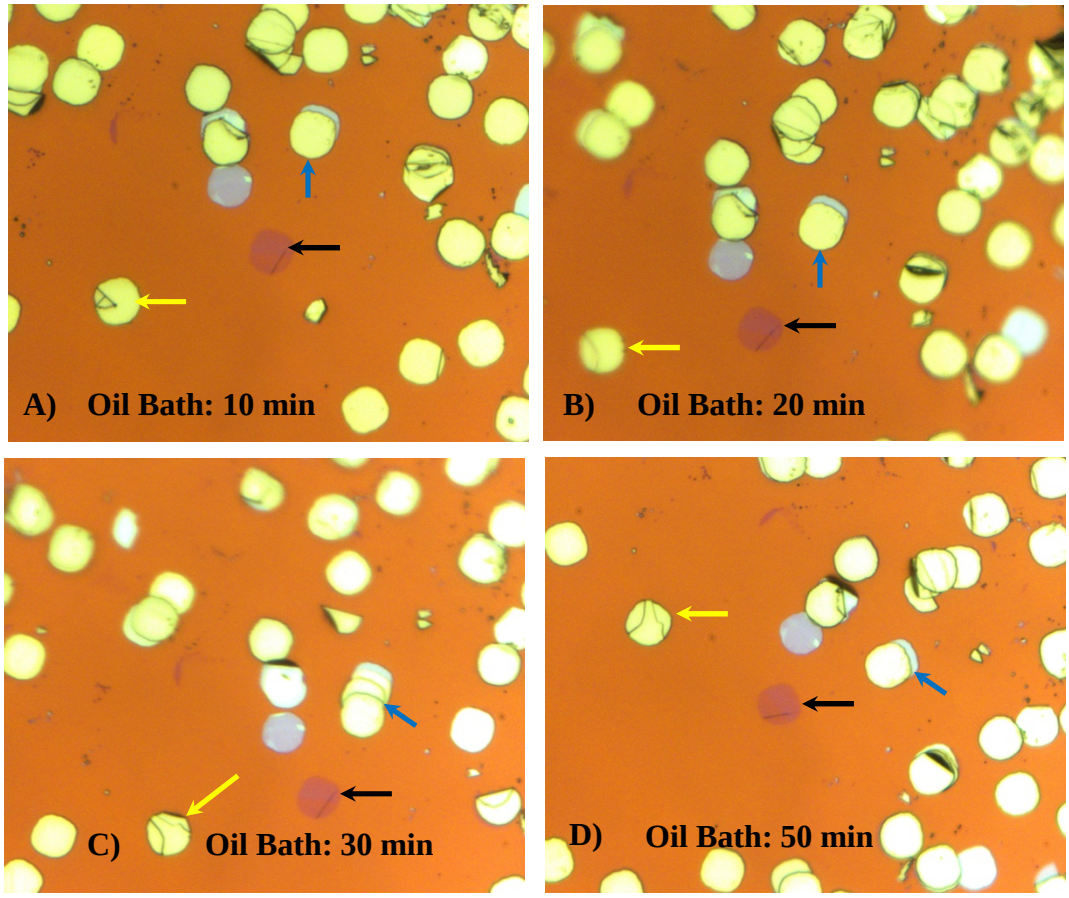

Figure 4.8: Time evolution of transferred HOPG pillar being exfoliated using low power sonication when suspended in oil. Optical microscopy images of oil bath sonication where A), B), C) and D) are sonication times of 10, 20, 30, and 50 minutes respectively where different colored arrows represent different kinds of exfoliation. These colors indicate the following; yellow color showing thinning and cleaning of non-whole pillars, blue representing high pillared graphite stacks separating out, and black consisting of a very thinned out graphene pillar stack that is undisturbed while cleaning and exfoliation of the surface are taking place.

hours causes degradation to start occurring before complete cleaning of the Si_3N_4 surface takes place. For reliability and repeatability, a clear depiction of the exfoliation and thinning process is demonstrated again in C).

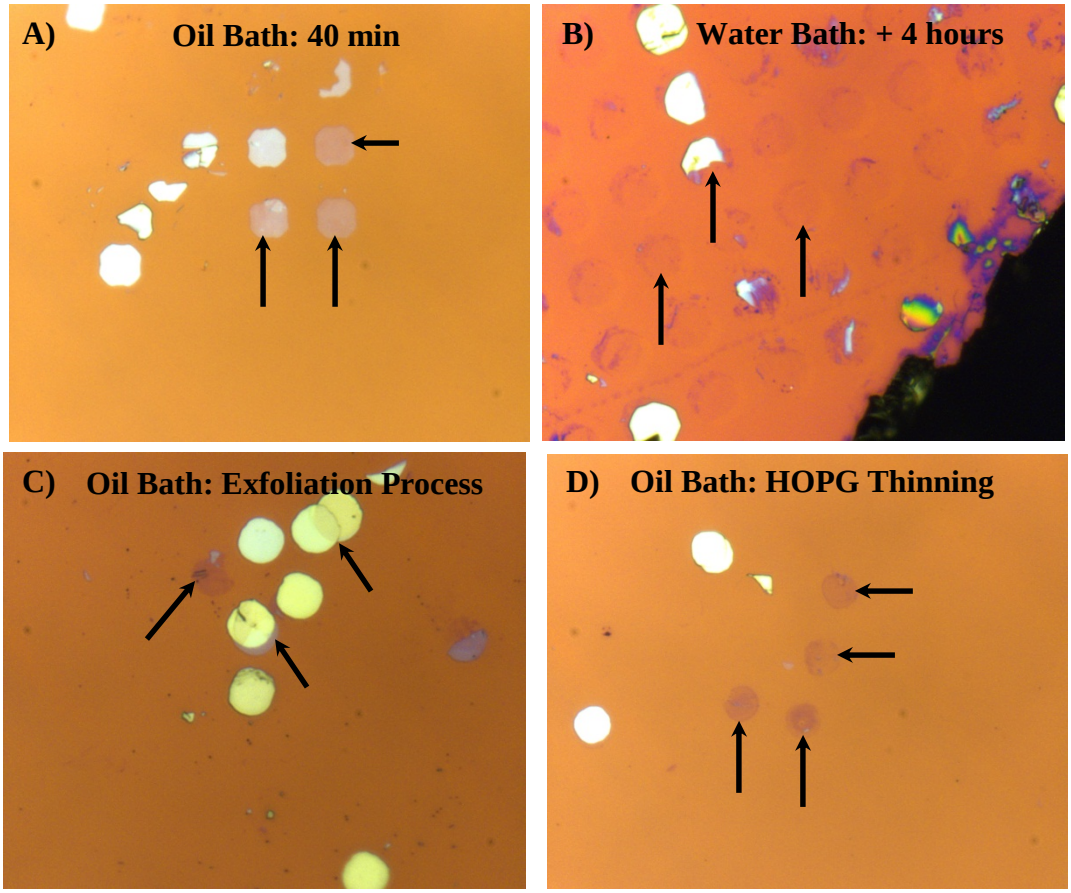

Figure 4.9: Optical microscopy images of transferred graphite pillars in a sonication bath where the following demonstrations are shown; A), D) after a 40 min oil bath well patterned HOPG pillar stacks are thinned out to the point where these 5um pillars become increasingly optically transparent in regards to the background getting closer to few-layered graphene, B) after 4+ hours complete stripping and degradation of these HOPG pillar stacks takes place, and C) clear exfoliation and thinning are demonstrated for repeatability.

Unfortunately, thinning these samples out until they are within 3 layers or less seems virtually impossible before degradation much less shifting or sliding on the Si_3N_4 becomes inevitable as well. Although this may seem largely unsuccessful when considering the initial goals that we set out to accomplish, it turns out that we learned a lot about how graphite can be reduced, yet still retain shape and size originally defined from pillar structuring which could lead to a number of potential applications.

4.4 SUMMARY

Demonstration of HOPG pillars transferred to Si_3N_4 using high force >20 N pressure with the key tool being a precision flat vice. Stamping was the primary method of transfer and could possibly be improved upon by applying voltage bias to enable additional electrostatic force pressure. Although, since we were largely unsuccessful at transferring these HOPG pillars to Si_3N_4 using predominantly electrostatic pressure forces, it is unknown as to why this force was largely unseen when using Si_3N_4 as the insulating barrier and in much contrast worked so well for SiO_2 in literature [7, 9-10]. Yet, our results were not surprising after a more detailed examination revealed that although there was a plethora of information regarding electrical characterization for SiO_2 and very little information about Si_3N_4 aside from Poole-Frenkle emission. Sonication proved to exfoliate / thin the transferred HOPG pillars when used in relatively clean oil (high enough grade to clean vacuum parts). In turn sonication provides a new way to exfoliate set determined size of HOPG pillars which could potentially provide the need for creating precise size particles for device applications. Numerous advantages exist by using sonication to process these graphene / graphite pillars which are atomically-thin, exhibit an extremely high surface area, are highly conductive which could further be exfoliated into 1-3 layers using further sonication in liquid and ultra-centrifuging [15], and can obtain an extremely high yield of identically sized monoatomic layer thick graphene or electrode particles where ‘size matters’. Other atomically-thin layered materials could be processed similarly too. Some potential applications include; a need for conductive

particles using percolation as a conductive paste, improve conduction for conductive layer on solar cell, and conductive part of a solid-state ultra-capacitor that hold charge.

REFERENCES

1. X. Li, W. Cai, J. An, S. Kim, J. Nah, D. Yang, R. Piner, A. Velamakanni, I. Jung, E. Tutuc, S. K. Banerjee, L. Colombo, and R. S. Ruoff, *Science* **324**, 1312 (2009).
2. T. Ohta, N. C. Bartelt, S. Nie, K. Thurmer, and G. L. Kellogg, *Phys. Rev. B* **81**, 121411 (2010).
3. A. Reina, X. Jia, J. Ho, D. Nezich, H. Son, V. Bulovic, M. S. Dresselhaus, and J. Kong, *Nano Lett.* **9**, 30 (2009).
4. X. Li, Y. Zhu, W. Cai, M. Borysiak, B. Han, D. Chen, R. D. Piner, L. Colombo, and R. S. Ruoff, *Nano Lett.* **9**, 4359 (2009).
5. A. Reina, H. Son, L. Jiao, B. Fan, M. S. Dresselhaus, Z. Liu, and J. Kong, *J. Phys. Chem. C* **112**, 17741 (2008).
6. W. Regan, N. Alem, B. Aleman, B. Geng, C. Girit, L. Maserati, F. Wang, M. Crommie, and A. Zettl, *Appl. Phys. Lett.* **96**, 113102 (2010).
7. A. N. Sidorov, M. M. Yazdanpanah, R. Jalilian, P. J. Ouseph, R. W. Cohn, and G. U. Sumanasekera, *Nanotechnology* **18**, 135301 (2007).
8. S. W. Howell, T. Ohta, K. F. McCarty, T. E. Beechem III, W. Pan, L. B. Biederman, A. J. Ross III, C. M. Nolen, and C. Gutierrez, SAND2011-6961 **U.S. DOE NNSA**, Contract DE-AC04-94AL85000 (2011).

9. L. B. Biedermann, T. E. Beechem, A. J. Ross, T. Ohta, and S. W. Howell, *New J. of Phys.* **12**, 125016 (2010).
10. X. Liang, Z. Fu, and S. Y. Chou, *Nano Lett.* **7**, 3840 (2007).
11. X. Liang, A. S. P. Chang, Y. Zhang, B. D. Harteneck, H. Choo, D. L. Olynick, and S. Cabrini, *Nano Lett.* **9**, 467 (2009).
12. S. Habermehl and C. Carmignani, *Appl. Phys. Lett.* **80**, 261 (2002).
13. S. Habermehl, R. T. Apodaca, and R. J. Kaplar, *Appl. Phys. Lett.* **94**, 012905 (2009).
14. Y. Hernandez, V. Nicolosi, M. Lotya, F. M. Blighe, Z. Sun, S. De, I. T. McGovern, B. Holland, M. Byrne, Y. K. Gun'Ko, J. J. Boland, P. Niraj, G. Duesberg, S. Krishnamurthy, R. Goodhue, J. Hutchison, V. Scardaci, A. C. Ferrari, and J. N. Coleman, *Nature Nano.* **3**, 563 (2008).
15. F. Torrisi, T. Hasan, W. Wu, Z. Sun, A. Lombardo, T. Kulmala, G. W. Hshieh, S. J. Jung, F. Bonaccorso, P. J. Paul, D. P. Chu, and A. C. Ferrari, *arXiv:1111.4970v1* [cond-mat.mtrl-sci] (2011).
16. J. X. Benedict, N. G. Chopra, M. L. Cohen, A. Zettl, S. G. Louie, and V. H. Crespi, *Chem. Phys. Lett.* **286**, 490 (1998).
17. L. A. Girifalco and R. J. Good, *J. Phys. Chem.* **61**, 904 (1957).
18. M. Hodak and L. A. Girifalco, *Chem. Phys. Lett.* **350**, 405 (2001).
19. R. Zacharia, H. Ulbricht, and T. Hertel, *Phys. Rev. B* **69**, 155406 (2004).
20. S. Niyogi, E. Bekyarova, M. E. Itkis, J. L. McWilliams, M. A. Hamon, and R. C. Haddon, *J. Am. Chem. Soc.* **128**, 7720 (2006).

21. N. Tas, T. Sonnenberg, H. Jansen, R. Legtenberg, and M. Elwenspoek, *J. Micromech. Microeng.***6**, 385 (1996).

Chapter 5

Conclusions

5.1 SUMMARY OF DISSERTATION THESIS

Development of new electronic material devices for numerous real-world applications are important for succeeding the current semiconductor industry into the future by innovating devices to provide solutions for enhancing these devices beyond their present limitations. Electronic devices which incorporate nanostructured atomically-thin layered materials have demonstrated use for a wide variety of practical applications with ground-breaking functionality proven to perform well beyond their predecessors. Limited industrial-wide use of nanostructured materials inside electronic devices has largely been constrained by scalability of material processes. The limiting scalability factor lies within wafer-scale quality control and reliability of material processing rendering nanostructured materials unable to provide necessary top-grade material for high-yield industrial applications.

In this dissertation, I investigated and demonstrated innovative techniques for a scalable inspection and electrostatic transfer process technique for atomically-thin layered materials. For the layer inspection process, I determined the number of atomic planes for atomically-thin layered materials over wafer-sized areas using initial Raman spectroscopy calibration and image processing for determination and classification. This inspection apparatus demonstrated the capability of acquiring important statistical analysis of each determined graphene layered region for a region area of interest

including; layer area coverage percentage, perimeter outline for post edge detection, and quantification of graphene growth area regions. With these results, if incorporated into an industrial SPC material inspection system, atomically-thin layered material growth parameters can be automatically tuned for achieving the necessary levels for reliable high-quality material growth for industrial standards.

For the scalable electrostatic transfer process, I moved few-layered graphene and graphite in patterns from its growth medium to Si_3N_4 dielectric substrate. Resulting demonstrations of this scalable technique has proven to be a reliable transfer process for depositing graphene layers to a precisely controlled location. Incorporation of this electrostatic graphene layer transfer process provides the semiconductor industry with a valuable transfer process step that is compatible with current fabrication processes in terms of scalability, reliability and retaining material quality. I have used electrostatic transfer and mechanical exfoliation of graphene, CVD grown graphene on Ni, and mechanical "graphene-like" exfoliation of Bi_2Te_3 and Sb_2Te_3 on SiO_2 or Si_3N_4 to demonstrate the scalable layer inspection and transfer process techniques. The results of this dissertation are important to succeed these nanostructured materials for practical new device implementation in the semiconductor industry with current material processes.

5.2 COMPETITIVE AWARDS WON DURING DISSERTATION RESEARCH

1. Recipient of MRS *Silver Symposium Award for Functional Two-Dimensional Layered Material Research*, Symposium Y, MRS Spring Meeting, San Francisco, CA April 26-29, 2011. Chairs: Andre Geim, Alexander Balandin, and Jiaxing Huang.
2. Recipient of *2nd Place Poster Award*, 1st IEEE-EDS Student Research Symposium, UC Riverside, April 2009. Chairs: 2009 IEEE EDS Presidents Cor Claeys and Renuka Jindal.
3. Recipient of *MRS Silver Poster Award* (co-author), MRS Spring Meeting, San Francisco, CA, April 2011. *Poster title: ""Graphene-like" Exfoliation of Quasi-2D Crystals of Titanium Ditelluride: A New Route to Charge Density Wave Materials."*
4. Recipient of *ECS 2nd Place Poster Award* (co-author), Electrochemical Society 219th Meeting, Montreal, Canada, May 2011. *Poster title: ""Graphene-Like" Exfoliation and Characterization of Material Properties of $TiTe_2$ Quasi-2D Crystals."*
5. Recipient of *Young Scientist Award* (co-author), 38th conference on the Physics & Chemistry of Surfaces and Interfaces (PCSI-38), San Diego, CA, January 16-20 2011.
6. Recipient of the *Verizon Corporation Scholarship Award for Navy Undergraduate Research*, October 2007.
7. Induction into two prestigious honor societies; *Tau Beta Pi Engineering (TBΠ) Honors Society* AB Chapter and *Omicron Delta Kappa (OΔK) Leadership Honors Society*
8. Recipient of *Full Graduate Division Doctoral Fellowship Award* UC Riverside (08'-12')

5.3 PATENT & PEER-REVIEWED PAPERS PUBLISHED FROM DISSERTATION RESEARCH

Patent

1. C. M. Nolen, G. Denina, D. Teweldebrhan, B. Bhanu, and A. A. Balandin. **"***Systems and Methods for Material Layer Identification through Image Processing***"** U.S. Patent App No: 13/052009. Filed: March 18, 2010. (Full Patent Funded: UCR)

Peer-Reviewed Published Papers

1. C. M. Nolen, G. Denina, D. Teweldebrhan, B. Bhanu, and A. A. Balandin, "*High-Throughput Large-Area Automated Identification and Quality Control of Graphene and Few-Layer Graphene Films*," ACS Nano, 5 (2), pp 914-922 (2011). *(Highlight: Nanowerk; "Graphene quality control goes industrial" Feb 2011)*
2. C. M. Nolen, A. Sumant, J. Yu, G. Denina, B. Bhanu, and A. A. Balandin, "*Large-Area Graphene Layer Identification and Statistical Analysis of Graphene Growth via Chemical Vapor Deposition on Nickel over Wafer-sized Areas*," (*Submitted to Carbon Journal)*
3. J. Khan, C. M. Nolen, D. Teweldebrhan, D. Wickramratne, R. K. Lake, and A. A. Balandin, "*Anomalous electron transport in back-gated field-effect transistors with $TiTe_2$ semimetal thin-film channels,"* Appl. Phys. Lett., 100(4), 043109 (2012). *(Highlight: AIP Virt. J. Nanoscale Science & Technology, Feb 6th, 2012)*
4. C. M. Nolen, D. Teweldebrhan, G. Denina, B. Bhanu, and A. A. Balandin, "*Large-Scale Automated Identification and Quality Control of Exfoliated and CVD Graphene via Image Processing Technique,"* ECS Trans. Vol. 33, pgs. 201-209, SOTAPOCS

52, Las Vegas, NV, Oct. 2010, M. E. Overberg, J. Brown, P. Hesketh, W. Johnson, H. Ma, P. Vanysek (eds.).

5. C. M. Nolen, D. Teweldebrhan, G. Denina, B. Bhanu, and A. A. Balandin, *"Large-Area Industrial-Scale Identification and Quality Control of Graphene,"* MRS Proceed., Vol. 1344, y03-26, Symposium Y, San Francisco, CA Apr 2011, A. A. Balandin, A. Geim, J. Huang, D. Li (eds.).
6. J. Khan, D. Teweldebrhan, C. M. Nolen, and A. A. Balandin, *""Graphene-Like" Exfoliation of Quasi-2D Crystals of Titanium Ditelluride: A New Route to Charge Density Wave Materials,"* MRS Proceed., Vol. 1344, y10-13, Symposium Y, San Francisco, CA Apr. 2011, A. Balandin, A. Geim, J. Huang, D. Li (eds.).
7. J. Khan, D. Teweldebrhan, C. M. Nolen, and A. A. Balandin,*""Graphene-Like" Exfoliation and Characterization of the Atomically-Thin Films of Titanium Ditelluride,"* ECS Trans. Vol. 35, pgs. 205-210, "Dielectrics in Nanosystems –and-Graphene, Ge/III-V, Nanowires and Emerging Materials for Post-CMOS Applications 3," Montreal QC Canada, May 2011, Z. Karim, D. Misra, P. Srinivasan, Y. Obeng, S. De Gendt (eds.).
8. J. Khan, C. M. Nolen, D. Teweldebrhan, and A. A. Balandin, *"Properties of Mechanically Exfoliated Quasi-Two-Dimensional Crystals of Titanium Ditelluride,"* ECS Trans. Vol. 33, pgs. 211-217, "(SOTAPOCS 52)", Las Vegas, NV, Oct. 2010, M. E. Overberg (eds.)

9. C. M. Nolen, G. Denina, A. Sumant, B.Bhanu, and A. A. Balandin, *"Scalable Large-Area Graphene Layer Detection and Statistical Analysis for CVD Grown Graphene on Ni,"* (In Preparation for Carbon Journal).
10. C. M. Nolen, T. Baldacchini, J. Yu, and A. A. Balandin, *"Large-Area High Throughput Graphene Layer Identification and Defect Detection using CARS femto-second laser pulses,"* (In Preparation for Nano Letters or ACS Nano).
11. C. M. Nolen, J. Latchinian, and A. A. Balandin, *"Fast Scalable Large-Area Graphene Height Determination Technique using an Optical Profiler via White Light Interferometry,"* (In Preparation for Applied Physics Letters).

5.4 CONFERENCE PRESENTATIONS FROM DISSERTATION RESEARCH

1. C. M. Nolen, D. Teweldebrhan, G. Denina, B. Bhanu, and A. A. Balandin, *"Large-Area High-Throughput Graphene Layer Identification: To Advance the Development of Wafer-Scale Quality Control Measurement Tools,"* Rad-Hard CMOS Technical Device Seminar 2011, Sandia National Laboratories, Albuquerque, NM, Jul. 2011. (Invited Talk)
2. C. M. Nolen, D. Teweldebrhan, G. Denina, B. Bhanu, and A. A. Balandin, *"Large-Area Industrial-scale Identification and Quality Control of Graphene,"* Materials Research Society 2011, Symposium Y, San Francisco, CA, Apr. 2011, A. Geim, A. A. Balandin, J. Huang, D. Li (eds.). (Best Presentation Award, Symposium Y, Silver ($200))

3. C. M. Nolen, D. Teweldebrhan, G. Denina, B. Bhanu, and A. A. Balandin, *"Large-Area Automatic Graphene Identification and Quality Control: Prospects of Industrial Applications,"* International Nano Conference 7, Albany, NY, May 11'. (Invited Poster)
4. C. M. Nolen, D. Teweldebrhan, G. Denina, B. Bhanu, and A. A. Balandin, *"An Optical Technique for the Large-Scale Graphene Recognition and Quality Control,"* OSA's 94th Meeting Frontiers in Optics: Laser Science XXVI, PDPA7, Rochester, NY, Oct. 2010.
5. C. M. Nolen, D. Teweldebrhan, G. Denina, B. Bhanu, and A. A. Balandin, *"Graphene-Silicon Heterogeneous Integration: Graphene Identification and Quality Control on Large-Scale Wafers,"* Inland Empire Tech Week 2010, CSU San Bernardino, CA, Oct. 2010.
6. C. M. Nolen, D. Teweldebrhan, G. Denina, B. Bhanu, and A. A. Balandin, *"Large-Scale Automated Identification and Quality Control of Exfoliated and CVD Graphene via Image Processing Technique,"* Electrochemical Society 218th Meeting, Las Vegas, NV, Oct. 2010.
7. C. M. Nolen, J. Khan, and S. Arab, *"Power Improvement in Wireless Sensor Networks Using a Graphene-Based Rechargeable Power Source in Sensor Nodes,"* IEEE-EDS Student Research Symposium1st Meeting, UC Riverside, Ca, April 2009, IEEE EDS Presidents Cor Claeys and Renuka Jindal (eds.). (2nd Place Poster Award)
8. J. Khan, C. M. Nolen, D. Teweldebrhan, A. Balandin, *"Properties of Mechanically Exfoliated Quasi-Two-Dimensional Crystals of Titanium Ditelluride,"*

Electrochemical Society 218th Meeting, Las Vegas, NV, Oct. 2010, John Lewis (eds.).

9. J. Khan, D. Teweldebrhan, C. M. Nolen, A. Balandin, "*Graphene-Like" Exfoliation and Characterization of Material Properties of $TiTe_2$ Quasi-2D Crystals*," Electrochemical Society 219th Meeting, Montreal, Canada, May 2011, Z. Karim, D. Misra (eds.).
10. Z. Yan, G. Liu, D. Teweldebrhan, V. Goyal, S. Sabrina, C. M. Nolen, and A. A. Balandin, "*Few-Layer Graphene Top-Surface Heat Spreaders for High-Power Electronics*," Physics & Chemistry of Surfaces & Interfaces, San Diego, Ca, Jan. 2011. (Best Poster Award)
11. M. Rahman, I. Bejenari, D. Kotchetkov, V. Goyal, M. Z. Hossain, C. M. Nolen, K. K. F. Shahil, P. Goli, "*Mobility in Silicon and Poly-Silicon Channels Embedded within Acoustically Hard Poly Crystalline Diamond Barriers,"* SRC FENA (UCLA) 5th Annual Review, Los Angeles, CA., March 2009.

APPENDIX A: MATLAB Code for Graphene Layer Identification

```
clear all
close all
clc
%%
=========================================================================

img0 = imread('4.18.bmp'); %Background Image
img1 = imread('4.17.bmp'); %Few-layer Graphene Image
layers = ['1st'; '2nd'; '3rd'; '4th'];
%%
=========================================================================
%           PHASE 1 : Uneven lighting correction
%=========================================================================

img1_orig = img1;

%Minimum intensity values added by the light
minr = min(min(img0(:,:,1)));
ming = min(min(img0(:,:,2)));
minb = min(min(img0(:,:,3)));

%Intensity values added by the light
diff_light(:,:,1) = img0(:,:,1) - minr;
diff_light(:,:,2) = img0(:,:,2) - ming;
diff_light(:,:,3) = img0(:,:,3) - minb;

%Subtracting the effect of light on the image
img1(:,:,1) = img1(:,:,1)-diff_light(:,:,1);
img1(:,:,2) = img1(:,:,2)-diff_light(:,:,2);
img1(:,:,3) = img1(:,:,3)-diff_light(:,:,3);

%Comparing the Original and Even Lighting
figure
subplot(1,2,1)
imshow(img1_orig)
title('Original Image')
subplot(1,2,2)
imshow(img1)
title('Image with "even" Lighting')

%Displaying the light intensity
figure
imshow(rgb2gray(diff_light), []);
title('Added Light Intensity')

[x, y] = size(img0(:,:,1));

% 3D View
```

```
figure
u = double(rgb2gray(diff_light));
[a, b] = meshgrid(1:y, 1:x);
surfc(a,b, u, 'EdgeColor','none')
title('Added Light Intensity 3D View')

%%
=========================================================================
%           PHASE 2 : Possible Graphene Layers Isolation
%=========================================================================
%Comparing Blank and Image
figure
subplot(1,2,1)
imshow(img0)
title('Blank Substrate')
subplot(1,2,2)
imshow(img1)
title('Image with "even" Lighting')

%Removing the substrate
diff_substrate = imabsdiff(rgb2gray(img0),rgb2gray(img1)+
rgb2gray(diff_light))>2;
diff_substrate = medfilt2(diff_substrate, [7 7]);
[x, y] = size(img0(:,:,1));
final = img1;
for i = 1:x
    for j = 1:y
        if(diff_substrate(i,j) == 0)
            final(i,j,:) = 0;
        end
    end
end

%Displaying the result of removing substrate
figure
imshow(final, [])
title('Image without the substrate')


[counts,range]=imhist(rgb2gray(img0));
upperlimit = 0;
for i = length(counts)-1:-1:0
    if(counts(i) > 0)
        upperlimit = i;
        break
    end
end
```

```
%%
=========================================================================
%           PHASE 3 : Separating Graphene layers using the known range
%=========================================================================

layer_mask = ones(x,y,5);
gray_img = rgb2gray(final);


% Range of possible graphene locations
r = 45;
offset = 26;
l1 = 4;
gap12 = 0;
l2 = 4;
gap23 = 0;
l3 = 4;
gap34 = 0;
l4 = 4;

% Segmenting the images based on the ranges
for i = 1:x
    for j = 1:y
        if((gray_img(i,j) < upperlimit-r) || (gray_img(i,j) >
upperlimit))
            gray_img(i,j) = 255;
        end
        if((gray_img(i,j) < upperlimit-offset-l1) || (gray_img(i,j) >
upperlimit-offset))
            layer_mask(i,j,1) = 0;
        end
        if((gray_img(i,j) < upperlimit-offset-l1-gap12-l2) ||
(gray_img(i,j) > upperlimit-offset-l1-gap12))
            layer_mask(i,j,2) = 0;
        end
        if((gray_img(i,j) < upperlimit-offset-l1-gap12-l2-gap23-l3) ||
(gray_img(i,j) > upperlimit-offset-l1-gap12-l2-gap23))
            layer_mask(i,j,3) = 0;
        end
        if((gray_img(i,j) < upperlimit-offset-l1-gap12-l2-gap23-l3-
gap34-l4) || (gray_img(i,j) > upperlimit-offset-l1-gap12-l2-gap23-l3-
gap34))
            layer_mask(i,j,4) = 0;
        end
    end
end

layer_mask_befor_filter = layer_mask;

%Applying filter to remove small regions
masksize = 9; %(9 is the best, 4, 14, 24, 32)
for i = 1:4
```

```
    layer_mask(:,:,i) = medfilt2(layer_mask(:,:,i), [masksize
masksize]);
end

% Before Median Filter
figure
for i = 1:4
    subplot(2,2,i)
    imshow(layer_mask_befor_filter(:,:,i), [])
    title([layers(i,:), 'Layer'])
end

% Before Median Filter : 1st Layer
figure
imshow(layer_mask_befor_filter(:,:,3), [])
title('1st Layer')

% After Median Filter
figure
for i = 1:4
    subplot(2,2,i)
    imshow(layer_mask(:,:,i), [])
    title([layers(i,:), ' Layer'])
end


% Applying Pseudo Color to the original image using information from
% segmentation
layered = img1_orig;
mask_from_image = zeros(x,y);
for i = 1:x
    for j = 1:y
        % Changing all 1st layer to Red
        if(layer_mask(i,j,1) == 1)
            layered(i,j,:) = [255 0 0];
            mask_from_image(i,j) = 1;
        end
        % Changing all 2nd layer to Green
        if(layer_mask(i,j,2) == 1)
            layered(i,j,:) = [0 255 0];
            mask_from_image(i,j) = 2;
        end
        % Changing all 3rd layer to Blue
        if(layer_mask(i,j,3) == 1)
            layered(i,j,:) = [0 0 255];
            mask_from_image(i,j) = 3;
        end
        % Changing all 4th layer to Yellow
        if(layer_mask(i,j,4) == 1)
            layered(i,j,:) = [255 255 0];
            mask_from_image(i,j) = 4;
        end
    end
```

```
end

layer_mask_orig = layer_mask;
% clear 'layer_mask'
for i = 1:4
    layer_mask(:,:,i) = double(mask_from_image == i);
end

figure
imshow(layered)
title('Final Result')

%==========================================================================
%           PHASE 4 : Statistical information
%==========================================================================

% Statistical Information

%Clustering detected pixels on each of the layer
neighbor = 8;
for i = 1:4
    [Label(:,:,i), numCluster(i)] = bwlabel(layer_mask(:,:,i) ,
neighbor);
end

% Plot of the labeled clusters
figure
for i = 1:4
    subplot(2,2,i)
    imshow(label2rgb(Label(:,:,i)))
    title([layers(i,:), ' Layer Clusters'])
end


for j = 1:4
    % Finding Area of all layers
    stat_AreaofLayers(j) = sum(sum(layer_mask(:,:,j)));

    % Finding the percentage of area of layers versus size of image
    stat_PercentofArea(j) = (stat_AreaofLayers(j) / (x*y) ) * 100;

    for i = 1:numCluster(j)
        % Finding the Areas of each detected clusters in each layers
        stat_areas(j,i) = length(find(Label(:,:,j) == i));
        % Finding the Perimeter of each of the detected clusters in
        each layers
        stat_perimeter(j,i) = sum(sum(bwperim(Label(:,:,j) == i, 8)));
    end

    disp_perim(:,:,j) = bwperim(Label(:,:,j));
```

```
end

% Plot of the Perimeter
figure
for i = 1:4
    subplot(2,2,i)
    imshow(disp_perim(:,:,i))
    title([layers(i,:), ' Layer Perimeters of each clusters'])
end

% Comparison of total area of each layer versus the entire image
areaPercent = zeros(x,y,3);
for i = 1:4
    A(i) = round(sqrt(stat_AreaofLayers(i)));
end
areaPercent(1:A(1), 1:A(1), 1) = 255;
areaPercent(1:A(2), sum(A(1)+1):sum(A(1:2)+2), 2) = 255;
areaPercent(1:A(3), sum(A(1:2)+2):sum(A(1:3)+3), 3) = 255;
areaPercent(1:A(4), sum(A(1:3)+3):sum(A(1:4)+4), 1) = 255;
areaPercent(1:A(4), sum(A(1:3)+3):sum(A(1:4)+4), 2) = 255;

figure
imshow(areaPercent )
title('Total Area Occupied by Each Layer')


%%
%=========================================================================
%               Additional Processing (Overlay Perimeter)
%=========================================================================

% Plot of the Perimeter
img1_perim = img1;
color = [255 0 0; 0 255 0; 0 0 255; 255 255 0;];


for i = 1:4
    for j = 1:x
        for k = 1:y
            if(disp_perim(j,k,i))
                img1_perim(j,k,:)=color(i,:);
            end
            if (sum(disp_perim(j,k,:)) > 1)
                img1_perim(j,k,:)= [255 255 255];
            end
        end
    end
end
figure
title('Perimeter overlaid on Image (White - shared perimeter)')
imshow(img1_perim)
```

```
%%
=========================================================================
%       Additional Processing (Area - sorted and visualized by size)
%=========================================================================


sorted_Label = zeros(x,y,4);
figure('Name', 'Area - sorted and visualized by size')
for h = 1:4
    [sorted, indSorted] = sort(stat_areas(h,:));
    for k = 1:length(indSorted)

        sorted_Label(:,:,h) = bsxfun(@plus, sorted_Label(:,:,h), ...
            (Label(:,:,h) == indSorted(k))*k);
    end
    subplot(2,2,h)
    imshow(label2rgb(sorted_Label(:,:,h)))
    title([layers(h,:), ' Layer Clusters'])
end
 %%
=========================================================================
```